UNIVERSITY OF SOUTHAMPTON
Faculty of Engineering and Physical Sciences
School of Electronics and Computer Science

Thesis for the degree of Doctor of Philosophy

Supervisors: Professor C.H. (Kees) de Groot
Professor Andrew L. Hector
Examiners: Dr Iris Nandhakumar
Dr Paz Vaqueiro

Thermoelectric Properties of Bismuth Telluride and Antimony Telluride Thin Films Electrodeposited from a Non-aqueous Solution.

by Katarina Cicvarić

November 26, 2020

UNIVERSITY OF SOUTHAMPTON

ABSTRACT

FACULTY OF ENGINEERING AND PHYSICAL SCIENCES
SCHOOL OF ELECTRONICS AND COMPUTER SCIENCE

Doctor of Philosophy

by Katarina Cicvarić

Thermoelectric materials have a potential for use in power generation technologies due to their ability to convert heat directly into electricity. The field of thermoelectrics has drawn a significant attention over the last 20-25 years because it is a pollution-free form of energy conversion. Of all the types of thermoelectric materials investigated so far, nanostructured materials have shown the most promise in enhancing performance of thermoelectric devices.

This work reports the thermoelectric properties of Bi_2Te_3 and Sb_2Te_3 thin films electrodeposited from the weakly coordinating solvent dichloromethane (CH_2Cl_2). It was found that the oxidation of porous Bi_2Te_3 films is significant, causing the degradation of its thermoelectric properties. It is shown that the morphology of the film can be improved drastically by applying a short initial nucleation pulse, which generates a large number of nuclei, and then growing the nuclei by pulsed electrodeposition at much lower overpotential. More importantly, this significantly reduces the oxidation of the films as smooth films have smaller surface-to-volume ratio and are less prone to oxidation. X-ray Photo-electron spectroscopy (XPS) shows that those films with Te(O) termination show complete absence of oxygen below the surface layer. A thin film transfer process was developed using polystyrene as a carrier polymer to transfer the films from the conductive TiN to an insulating layer for thermo-electrical characterisation. Temperature dependent Seebeck measurement reveal a room temperature coefficient of -50 μV/K growing to nearly -100 μV/K at 520. The corresponding power factor reaches value of about 90 $\mu W/mK^2$ at that temperature. It is shown that Sb_2Te_3 films' morphology is improved by employing pulsed electrodeposition compared to potentiostatic. As-deposited film exhibits poor crystallinity, crystallising after annealing at 100°C. The Seebeck coefficient increases with temperature increase reaching a value of 107.5 μV/K at 485 K. The corresponding power factor reaches nearly 100 $\mu W/mK^2$ at 464 K. Hence, this work demonstrates electrodeposition of Bi_2Te_3 and Sb_2Te_3 thin films from dichloromethane, which could be implemented for the fabrication of thin film device for thermo-electric energy conversion.

List of Publications

Journal Publications

Katarina Cicvarić, Lingcong Meng, Daniel W. Newbrook, Ruomeng Huang, Sheng Ye, Wenjian Zhang, Andrew L. Hector, Gillian Reid, Philip N. Bartlett and C.H. de Groot, Thermoelectric properties of bismuth telluride thin films electrodeposited from a non-aqueous solution, *ACS Omega* 2020, 5, 14679–14688.

Lingcong Meng, Katarina Cicvarić, Andrew L. Hector, C.H. de Groot, Philip N. Bartlett, Electrodeposition of bismuth telluride from a weakly coordinating, non- aqueous solution, *Journal of Electroanalytical Chemistry*, 839 (2019), 134–140.

Ruomeng Huang, Gabriela P. Kissling, Reza Kashtiban, Yasir J. Noori, Katarina Cicvarić, Wenjian Zhang, Andrew L. Hector, Richard Beanland, David C. Smith, Gillian Reid, Philip N. Bartlett and C. H. (Kees) de Groot, Towards a 3D GeSbTe phase change memory with integrated selector by non-aqueous electrodeposition, *Faraday Discussions*, 2019, 213, 339.

Conference Publications

Katarina Cicvarić, Lingcong Meng, Ruomeng Huang, Wenjian Zhang, Gabriela P. Kissling, CH Kees de Groot and Philip N. Bartlett, Pulsed electrodeposition and transfer of bismuth telluride thin films, European Materials Research Society (E-MRS) Nice, France (2019).

Katarina Cicvarić, Lingcong Meng, Ruomeng Huang, Wenjian Zhang, Gabriela P. Kissling, CH Kees de Groot and Philip N. Bartlett, Pulsed electrodeposition and transfer of bismuth telluride thin films, International Conference on Thermoelectrics (ICT) Gyeongju, South Korea (2019).

Katarina Cicvarić, Lingcong Meng, Ruomeng Huang, Wenjian Zhang, Gabriela P. Kissling, CH Kees de Groot and Philip N. Bartlett, Pulsed electrodeposition and transfer of bismuth telluride thin films, International Conference on Materials Chemistry (MC) Birmingham, United Kingdom (2019).

Acknowledgements

I spent three years working at University of Southampton towards my PhD degree. Along this way I had guidance and support from my supervisors, colleagues, family and friends, and I wish to thank them on this occasion.

First of all, I wish to thank my main supervisor Prof. Kees de Groot for giving me an opportunity to pursue a PhD, and for his professional guidance, help and feedback throughout this time. Most of all thanks for being flexible allowing me to explore the fields of my interest, for the encouragements and patience. I also thank to my other supervisor Prof. Andrew L. Hector for all the advice and help in his field of expertise.

I wish to thank all the members of the ADEPT project; investigators, postdocs, PhD students and the project manager Dr. Josephine Corsi. It has been a privilege working with everyone on such an ambitious and exciting project, and an enjoyable experience. Special thanks to Prof. Philip N. Bartlett for all his expert advice and feedback on my work. Many thanks to Dr. Ruomeng Huang and Dr. Lingcong Meng for their help and guidance on the experimental part of fabrication and electrodeposition.

Thanks to all my colleagues in SET research group for being helpful and supportive throughout the years. Thanks to Dr. Jamie D. Reynolds for useful advice on the thin film transfer. Also, many thanks to the staff members in the Cleanroom for all the help on my experimental work.

I wish to thank to my family, relatives and close friends for their love throughout my life. Thanks to my parents and my brothers for your endless support throughout this time when I was doing my PhD abroad and when I needed it the most. To all my friends for being there for me during this time I am very grateful.

Finally, I wish to thank The Engineering and Physical Sciences Research Council (EPSRC) funding body for enabling this work and offering me an opportunity to give my contribution to the scientific community.

Contents

Chapter 1

Introduction

The world is currently facing numerous challenges related to energy supply and consumption. The global demand for energy continues to rise, with a projection of increase of 48% from 2012 to 2040 as a result of world's population and economic growth. Consequently, there is a growing awareness and concern over the negative effect of the greenhouse gasses on the environment as fossil fuel combustion still accounts for majority of energy conversion [1]. Therefore, the need for energy sources other than fossil fuels has induced a significant amount of research of alternative energy sources and sustainable energy conversion technologies. Moreover, more than 60% of energy worldwide is lost mostly in the form of waste heat [2]. Thermoelectrics could be used in energy conversion devices, as these materials have the ability to convert heat directly into electricity. Moreover, the thermoelectric system is an environment-friendly solid-state energy conversion technology with advantages of being highly reliable, small-sized, pollutant-free and feasible in a wide temperature range. The proposed applications for thermoelectric materials are in thermoelectric-solar hybrid system to make use of the IR part of the solar spectrum, capturing waste heat from exhaust and transforming it into electricity in automobiles, localised cooling in computers, infrared detectors and many others. However, the practical realisation of thermoelectric energy conversion technologies is still limited as commercially available systems possess low figure of merit ZT which makes them uncompetitive with current widely used technologies, such as fossil fuel combustion. Thermoelectric generators have recently been installed into automobiles, and thermoelectric refrigeration system has been included in seats and electronic components for cooling. Apart from this practical realisations, NASA's Voyager and Cassini space probes are using thermoelectric generators powered by radioactive decay [3].

Thermoelectric device consists of couples made of alternating n- and p-type semiconducting materials, connected electrically in series and thermally in parallel. When a temperature difference is imposed on thermoelectric materials, electrons in n-type and holes in p-type semiconductor move from the hot side to cold side. This accumulation

of charge on the cold side induces voltage. If the module is connected to a circuit, the generated voltage will drive the electric current [4].

Bismuth telluride and antimony telluride are the most efficient and most widely used thermoelectric materials for low temperature applications (up to 200 °C). These materials are composed of heavy atoms which scatter phonons enabling the temperature gradient needed for electron flow. Furthermore, these materials are self-doped due to the anti-site defects providing charge carriers in the order of 10^{18}-10^{20} [5]. However, they possess a figure of merit (ZT) of around 1 which is not high enough for large scale implementation. Moreover, tellurium is one of the rarest elements in Earth's crust, with abundance comparable to that of platinum. Therefore, manufacturing bulk thermoelectric generators is not practical. Thin film thermoelectric generators on the other hand could be integrated on large scale using flexible substrates. Currently, there is a range of fabrication techniques being used for thin film fabrication, such as sputtering, chemical vapour deposition (CVD), pulse laser deposition (PLD), molecular beam epitaxy (MBE), evaporation and electrodeposition. In comparison to other methods for thin film fabrication, electrodeposition of thin films has advantages of being relatively cost-effective as it does not require high vacuum and elevated temperatures, easier control over thickness and composition, and deposition of films with thicknesses ranging from nanometers to hundreds of micrometers over a large area. Electrodeposition is also particularly well suited to deposition on complex geometries [6][7]. Electrodeposition of bismuth telluride thin film has been well studied and so far the material has been deposited by different electrochemical methods, such as potentiostatic electrodeposition [8][9][10][11][12][13], galvanostatic electrodeposition [14] and pulsed electrodeposition [15][16][17][18]. The most popular method is potentiostatic electrodeposition from nitric acid electrolyte containing Bi^{3+} and $HTeO_2{}^+$, which was studied extensively in [19]. Non-aqueous solvents have a wider electrochemical window than water allowing the investigation of more negative overpotentials, and bismuth telluride thin films have also been successfully electrodeposited from these without the reduction of the solvent. The electrodeposition from non-aqueous solvents including dimethylsulfoxide [20], ethylene glycol [21], chloride-free ethylene glycol [22], and 1-ethyl-1-octyl-piperidinium bis(trifluoromethylsulfonyl)imide: 1-ethyl-1-octyl-piperidinium bromide [23] has been reported. Organic solvents also provide improved solubility of Bi(III) and Te(IV) salts which are only moderately soluble in aqueous acidic media limiting the deposition rate. The use of non-aqueous solvents also widens the range of precursor salts that can be employed compared with aqueous media. In this work, electrodeposition from a non-aqueous solvent dichloromethane was investigated. The solvent's low surface tension could potentially allow us to electrodeposit bismuth telluride nanowires of much smaller diameter than those grown in an aqueous solution. This would be beneficial as previous theoretical works predict a great enhancement of ZT for nanowires of 8 nm [24] and smaller, while from aqueous solvent, nanowires below 15 nm cannot be obtained [25].

As in the case of bismuth telluride, antimony telluride thin film electrodeposition has mainly been investigated in acidic aqueous solvents [26], [27], [28], [29], [30], [31], [32], [33], [34]. However, not many reports exist in literature on Sb_2Te_3 electrodeposition possibly due to poor solubility of Sb precursor in aqueous solutions. In most cases this consequently leads to amorphous films and a need of post-annealing treatment in order to obtain good thermoelectric performance [32]. Investigations of electrodeposition of antimony telluride thin films from non-aqueous solutions was reported in molten mixture of acetamide-antimony chloride and tellurium chloride [35], and in ionic liquid consisting in mixture of choline chloride with oxalic acid [36].

In this work, electrodeposition of bismuth telluride and antimony telluride thin films from electrolyte containing $[N^nBu_4][BiCl_4]$, $[N^nBu_4][SbCl_4]$ and $[N^nBu_4]_2[TeCl_6]$ as Bi, Sb and Te precursors, respectively, with addition of $[N^nBu_4]Cl$ as supporting electrolyte in dichloromethane (CH_2Cl_2) has been investigated. In addition, the electrodeposited Bi_2Te_3 and Sb_2Te_3 thin film thermo-electric properties have been measured.

Chapter 2

Theory of Thermoelectric Materials

2.1 Thermoelectric energy conversion

Thermoelectric energy conversion is based on the Seebeck effect, named after Thomas Johann Seebeck who discovered it in 1821 [2]. Seebeck found that a compass needle deflects if a temperature gradient is imposed on two different metals connected in a closed loop. It was later realised that the deflection of the compass needle is caused by the generation of magnetic field due to electrical current passing through the loop. Today, we have a scientific explanation of the thermoelectric phenomenon. In the case of semiconductors, mobile charge carriers (electrons in n-type and holes in p-type) have more thermal energy at the hot side of the material than the carriers at the cold side. Therefore, the mobile charge carriers will diffuse to the cold side and since there are more mobile carriers at the cold side of the material than at the hot side, an electric field forms in response to inhomogenous charge distribution opposing further diffusion. If the material is in an open circuit, an equilibrium will form when the rate at which carriers diffuse from the hot to the cold side is balanced by the rate at which carriers move in the opposite direction due to the accumulated electric field. Consequently, an electrochemical potential forms in response to a temperature gradient, known as Seebeck voltage. The amount of voltage generated per unit temperature gradient is called Seebeck coefficient. If the material is connected to a circuit, the electrochemical potential will drive the electrical current which can be used to perform useful work. This is the basis of thermoelectric power generation. In Seebeck's case, the potential difference between the junctions induced by the temperature gradient drives an electrical current which generates a magnetic field around the wires, causing the deflection of the compass needle [37].

The Seebeck effect is defined by Eq. 2.1

$$E_{\text{emf}} = -S\Delta T \tag{2.1}$$

where E_{emf} is the electromotive force, S is the Seebeck coefficient (also known as the thermopower), an intrinsic property of the material being used, and ΔT is the temperature gradient.

The reversal of this phenomenon is known as Peltier effect: if an electrical current is passed through the junction of two different metals, heat is either absorbed or rejected at the junction, depending on the current's direction. The Peltier effect allows thermoelectricity to be used for cooling or heating, with the heat flow given as by Eq. 2.2

$$Q = \Pi I \tag{2.2}$$

where Q is the heat absorbed or emitted, Π is the Peltier coefficient, and I is the applied current. Peltier coefficient (Π) is a material dependent parameter related to Seebeck coefficient describing how much thermal energy is carried per charge carrier. It is defined as by Eq. 2.3

$$\Pi = ST \tag{2.3}$$

2.2 Figure of merit, *ZT*

The efficiency of thermoelectric materials is related to a dimensionless figure of merit, ZT, which ties conversion efficiency to the materials properties, and is defined by Eq. 2.4

$$ZT = \frac{S^2 \sigma T}{\kappa_{lattice} + \kappa_{electronic}} \tag{2.4}$$

where S (V/K) is the Seebeck coefficient, σ (S/m) is the electrical conductivity, T (K) is the temperature, and $\kappa_{lattice}$ and $\kappa_{electronic}$ $(W/m\ K)$ are the lattice and electronic contribution to the thermal conductivity, respectively. In order to maximise ZT, a material needs to have a large Seebeck coefficient, high electrical conductivity, and low thermal conductivity. However, the interdependence of these material properties makes the manipulation difficult. As can be seen in Fig. 2.1, an increase in carrier concentration increases the electrical conductivity (σ), however the thermal conductivity (κ) increases as well. Furthermore, an increase in carrier concentration decreases the Seebeck coefficient (S).

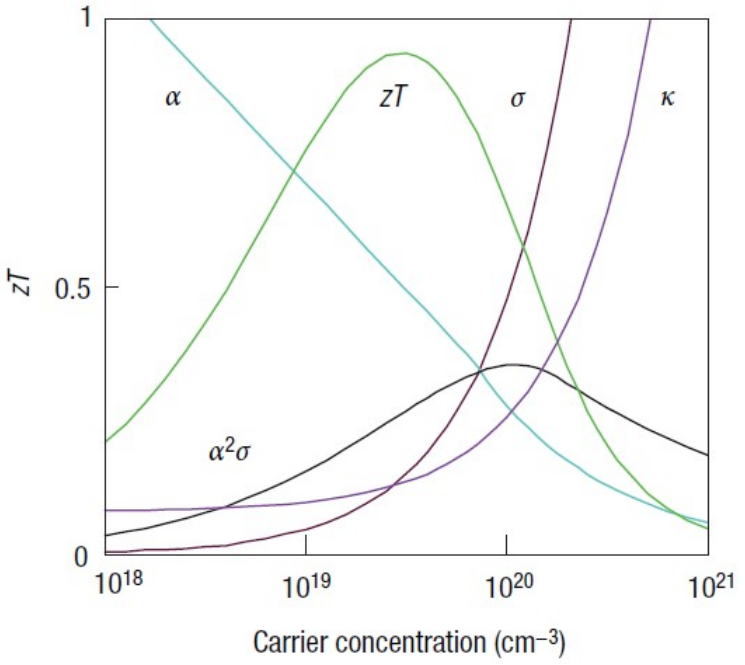

FIGURE 2.1: Interdependence of Seebeck coefficient (S), electrical conductivity (σ) and thermal conductivity (κ). The maximum figure of merit ZT is proportional to the power factor $S^2\sigma$. Reprinted by permission from [4], Springer Nature.

The relationship between the electrical conductivity and the carrier concentration is defined by Eq. 2.5

$$\sigma = ne\mu \tag{2.5}$$

where e is the carrier charge, n is the carrier density, and μ is the carrier mobility. The relationship between the Seebeck coefficient and the carrier concentration can be expressed with Eq. 2.6

$$S = \frac{8\pi^2 {k_\mathrm{B}}^2}{3eh^2} m^* T (\frac{\pi}{3n})^{2/3} \tag{2.6}$$

where k_B is the Boltzmann constant, h is the Planck's constant, m^* is the effective mass of the charge carrier, and n is the carrier concentration. Low carrier concentration insulators and semiconductors posses large Seebeck coefficient (S), and a high electrical conductivity is found in high carrier concentration metals. Thus, the thermoelectric power factor ($S^2\sigma$) maximises somewhere between the carrier concentrations of semiconductors and metals. Generally, the best thermoelectric materials are heavily doped semiconductors with carrier concentration of 10^{19} - 10^{21} cm^{-3}. In order to ensure a large Seebeck coefficient, a single type of carriers (n-type or p-type) must be achieved, as mixed n-type/p-type charge carriers will lead to the opposite Seebeck effect which will cancel out. Therefore, the suitable materials are those with energy bandgaps and appropriate doping, where n-type and p-type can be separated.

The thermal conductivity of thermoelectric materials consists of two parts: $\kappa_{lattice}$, resulting from the heat transporting phonons travelling through the crystal lattice, and $\kappa_{electronic}$, resulting from the heat carrying charge carriers (electrons or holes) travelling through the crystal lattice. Electronic contribution to the thermal conductivity for metallic systems and degenerate semiconductors can be can be estimated using Wiedemann-Franz law, defined by Eq. 2.7

$$\kappa_{electronic} = \sigma L T \tag{2.7}$$

where L is the Lorenz number (L=2.4 $\times$ 10^{-8} J^2 K^{-2} C^{-2}). According to the Wiedemann-Franz law, it can be seen that the electronic thermal conductivity is proportional the electrical conductivity. Lattice thermal conductivity can be expressed by Eq. 2.8

$$\kappa_\mathrm{L} = \frac{1}{3}(C_\mathrm{v} v_\mathrm{s} \lambda_\mathrm{ph}) \tag{2.8}$$

where C_v is the heat capacity, v_s is the sound velocity, and λ_{ph} is the phonon mean free path (mfp) [38],[39]. The relationship between the figure of merit (ZT) and the efficiency for power generation in a thermoelectric device is defined by the Eq. 2.9

$$\eta(\%) = 100 \times (\frac{T_{\mathrm{H}} - T_{\mathrm{C}}}{T_{\mathrm{H}}}) \frac{\sqrt{1 + Z\overline{T}} - 1}{\sqrt{1 + Z\overline{T}} + (\frac{T_{\mathrm{H}}}{T_{\mathrm{C}}})} \tag{2.9}$$

where η is the efficiency of a device, T_H and T_C are the temperatures at hot and cold side of the device, respectively, and $Z\overline{T}$ is the figure of merit at mean temperature [40].

2.3 Conventional thermoelectric materials

Majority of the work on thermoelectrics focuses on semiconductors. The conditions providing the highest ZT are satisfied in highly covalent intermetallic compounds and alloys of heavy elements, such as: Pb, Bi, Tl, Sb, S, Se and Te. According to the optimal working temperature, conventional thermoelectric materials can be divided into:

- low-temperature range (<500 K) materials, based on alloys of Bi_2Te_3 with Sb_2Te_3 and Bi_2Se_3
- middle-temperature range (600-900 K) materials, based on PbTe, GeTe and SnTe
- high-temperature range (>900 K), based on SiGe alloys

So far, the most widely used thermoelectric materials have been alloys of Bi_2Te_3 with Sb_2Te_3 and Bi_2Se_3. These semiconducting materials possess the highest ZT of around 1 at room temperature of any known material, and are commercially used in low-power cooling and low-power thermoelectric generation [4].

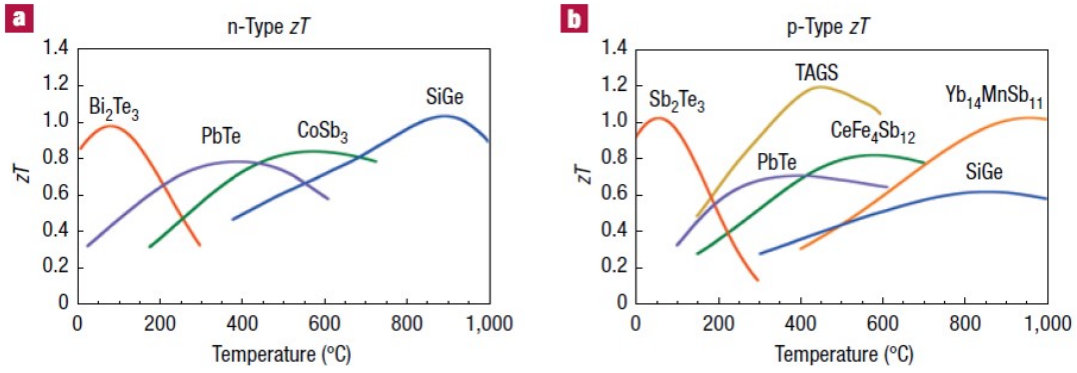

FIGURE 2.2: Figure of merit ZT of state-of-the-art commercial materials and those used or being developed by NASA for thermoelectric power generation. a) n-type, and b) p-type. Reprinted by permission from [4], Springer Nature.

In order to make thermoelectric devices competitive to existing energy-conversion technologies, materials with ZT value of above 1.5 for effective power generation and above 2 for cooling are needed [41]. Although the ZT of traditional bulk materials remained near 1 for decades, recent discoveries have revealed new bulk materials with better thermoelectric performances and the development of nanoscale and nanostructured materials which have pushed the ZT value to above 1 (see Fig. 2.5), and further increment is expected [38].

2.3.1 Structural characteristics of bismuth and antimony telluride thermoelectric material

As mentioned above, alloys of Bi_2Te_3 with Sb_2Te_3 and Bi_2Se_3 are the most widely used thermoelectric materials for a near-room-temperature power generation. Bi_2Te_3 and Sb_2Te_3 are narrow-band-gap semiconductor composed of heavy elements bonded covalently. Heavy elements scatter phonons as large atoms with relatively weak bonds are highly polarizable, while covalent bonding allows high electron mobility, making these materials good candidates for thermoelectric applications. An undped Bi_2Te_3 possesses intrinsic charge carrier concentration in the order of 10^{18}-10^{19} cm^{-3} due to antisite defects. Bi-rich Bi_2Te_3 is p-type due to Bi_{Te} acceptor effects, while the Te rich compound is n-type due to the Te_{Bi} donor defects. Sb_2Te_3 is always p-type, even the Te-rich compound which is due to the low formation energy of Sb_{Te} antisite defects. Both Bi_2Te_3 and Sb_2Te_3 have a rhombohedral unit cell belonging to the space group D_{3d}^5-$R\bar{3}m$, also described as hexagonal unit cell. Experimentally determined lattice parameters are $a_{Bi_2Te_3}$=4.395 Å,$c_{Bi_2Te_3}$=30.014 Å, and $a_{Sb_2Te_3}$=4.273 Å, $c_{Sb_2Te_3}$=30.467 Å for Bi_2Te_3 and Sb_2Te_3, respectively [42]. Fig. 2.3 shows model of Bi_2Te_3 hexagonal crystal structure, where the same structure can be applied to Sb_2Te_3. In the compound Bi(Sb) is somewhat less electronegative than Te, hence the valences can be associated as Bi^{3+}(Sb^{3+}) and Te^{2-}. The crystal exhibits a layered structure with the sequence -(Te^1-Bi(Sb)-Te^2-Bi(Sb)-Te^1)- (quintuple layer). Te^1 and Te^2 refer to Te atoms with different surroundings, bonded with nearest Bi(Sb) atom with polar-covalent type of bond. The Te^1–Te^1 bond is weak van der Waals bond between large Te atoms that are highly polarizable, responsible for the easy cleavage along the basal plane and anisotropy in electric and thermal conductivity. The crystal's electrical conductivity (σ) is higher within the basal plane than perpendicular to the basal plane. Seebeck coefficient (S), on the other hand, is nearly isotropic. However, the lattice thermal conductivity (κ_L) along the basal plane is higher than perpendicular to the basal plane. The ZT value is hence higher within basal plane than out-of-plane [5],[16].

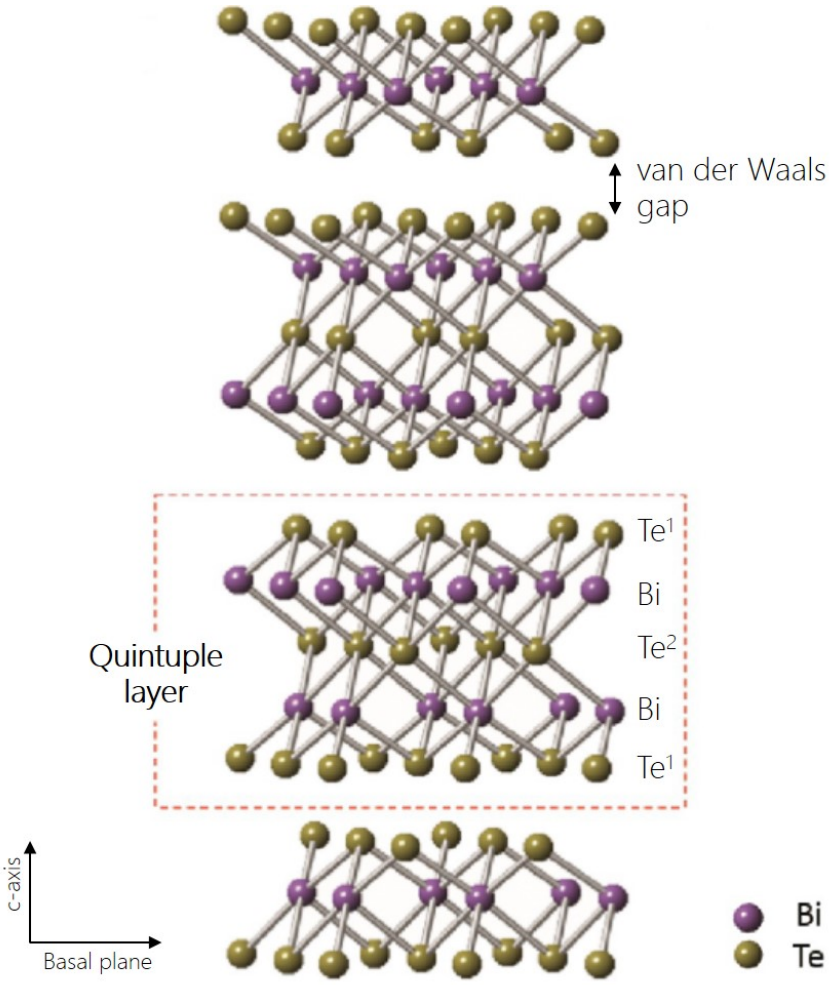

FIGURE 2.3: Schematic representation of Bi_2Te_3 hexagonal crystal structure. Reprinted from [43].

2.4 Enhancing thermoelectric performance

A key strategy in enhancing ZT, and therefore improving thermoelectric performance is decoupling the materials properties that determine ZT. The interdependency of the thermoelectric parameters makes the efforts to enhance ZT value very challenging. An attempt to increase electrical conductivity σ can result in an increase in electronic thermal conductivity $\kappa_{electronic}$, which contributes to total thermal conductivity κ. Decreasing κ with phonon scattering could, on the other hand, result in a decrease in electrical conductivity.

Approaches in achieving higher values of ZT rely on strategies aiming to either increase the power factor ($S^2\sigma$) by optimising the carrier concentration n, or decrease the thermal conductivity by introducing the scattering centres. These strategies include: use of materials composed of elements with heavy atomic masses, designing alloys to create point defects that scatter phonons, use of complex crystal materials containing elements which do not have well defined positions within the lattice, use of dopants with energy levels nearly resonant with material's Fermi level, and reduced dimensionality approach to improve bulk materials' properties [38, 44, 45, 3].

2.4.1 Alloying and doping approach

The major success in enhancing the thermoelectric properties in bulk materials is achieved by tuning or doping techniques in order to increase charge carrier concentration and reduce lattice thermal conductivity. Therefore, good thermoelectric materials are heavily doped semiconductors with high carrier concentration and low thermal conductivity. Alloys of Bi_2Te_3 with Sb_2Te_3 and Bi_2Se_3 have traditionally been used in thermoelectric devices for low-temperature power generation (up to 500 K) as p- and n-type semiconducting materials, respectively. Alloying creates point defects due to mass fluctuation in the crystal lattice reducing the phonon mean free path and hence the thermal conductivity, as well as tuning of the carrier concentration. The optimised composition for the p-type alloy is $(Sb_{0.8}Bi_{0.2})_2Te_3$ with a peak ZT of 1.1, whilst n-type is optimised to $Bi_2(Te_{0.8}Se_{0.2})_3$ with the highest ZT reaching 0.8 [4],[46]. Doping Bi_2Te_3 or its alloy with I as an electron donor can tune the carrier concentration producing n-type material [5].

Thermoelectric materials used at medium temperatures (500-900 K) are group IV tellurides (PbTe, GeTe, SiTe) based materials. In an optimised n-type alloy ZT peaks at about 0.8, while p-type alloy known as TAGS ($(GeTe)_{0.85}(AgSbTe_2)_{0.15}$) ZT reaches 1.2 [4]. Here as well, doping can be employed to tune the carrier concentration. Both n and p-type PbTe can be produced by adding some impurities such as halogenides as donors ($PbCl_2$, $PbBr_2$, PbI_2) and alkali metals as acceptors (Na_2Te, K_2Te). The ZT of PbTe at higher temperature is found to surpass ZT value of Bi_2Te_3 due to the s^2 lone pair

and distortion of structure at higher temperatures [47]. Since Te is scarce in the Earth's crust (0.001 ppm) with low concentration even compared to Pt (0.005 ppm) and Au (0.004 ppm), PbSe and PbS are suggested as alternatives [48].

The traditional high temperature thermoelectric material is $Si_{1-x}Ge_x$ alloy used as both p- and n-type material. Because silicon and germanium have the same crystal structure, lattice order is kept during alloying. However, the ZT of this material is rather low due its relatively high lattice thermal conductivity [4].

The required intrinsic properties of high thermopower and low thermal conductivity were found in $NaCo_2O_4$ making the compound an attractive candidate for thermoelectric applications. By partially replacing Na with Ca, carrier concentration is reduced and the thermopower increased [49]. Cobalt based oxide semiconductors have potential advantages over conventional high temperature thermoelectric materials in terms of chemical and thermal resistance as p-type materials, but the n-type materials have shown a rather low ZT. The compound Zn_4Sb_3 has shown as one of the efficient thermoelectric materials due to its extraordinary low thermal conductivity and electronic structure of a heavily doped semiconductor [50].

This approach has been used to produce materials used in commercial devices for decades. Although point defects created by doping in solid solutions serve to decrease the lattice thermal conductivity by increasing phonon scattering, there is also reduction in charge carrier mobility. Consequently, the overall ZT enhancement is limited [51].

2.4.2 Complex crystal structures

This approach focuses on investigating materials which have high electronic conductivity due to their highly periodic crystal structure but low thermal conductivity resulting from their complex crystal lattices. The partially filled clathrates and skutterudites are the most studied groups of complex materials which are believed to be "phonon-glass electron-crystals" (PGEC), meaning that the materials have a low lattice thermal conductivity as in the glass, and a high electrical conductivity as in a crystal. Skutterudite containing elements with low electronegativity differences, such as $CoSb_3$ and $IrSb_3$, have a high degree of covalent bonding which enables them high carrier mobilities. However, the strong bonding and simple lattice order leads to high lattice thermal conductivity (κ_L). Generally, structures of these materials have voids which can be filled with loosely-bounded atoms that vibrate at low frequencies and consume thermal energy [4]. Skutterudite compounds $Ba_{0.15}In_{0.16}Co_4Sb_{11.83}$ and $Ba_{0.14}In_{0.23}Co_4Sb_{11.84}$ [52] and clathrate $Ba_8Ga_{16}Ge_{13}$ [53] have found to have ZTs near 1.35.

Zintil compounds, such as $Yb_{14}MnSb_{11}$ [54], are materials with complex crystal structures and large unit cells which are being investigated as thermoelectric materials. These materials have a combination of covalent and ionic bonding, leading to higher charge

mobilities than purely ionic compounds and unit cells with intrinsically low thermal conductivity. Furthermore, this combination of the bonding types leads to complex structures with the possibility of multiple structural units in the same structure.

Another class of complex materials promising in thermoelectric applications is Nowotny chimney ladder (NCL) compounds [55]. This materials have a variable length, columnar sublattice of non-metal atoms (ladders) in the channels (chimneys) of a metal atom sublattice. Such materials have complex structures at the borderline between crystalline solids and amorphous materials.

2.4.3 Resonant energy level doping

As mentioned above, in order to maximise ZT, optimisation of carrier concentration is required. In most semiconductors by adding dopants energy states within the band gap are introduced. However, if a dopant has energy levels near the Fermi level, the density of states near the Fermi level is increased which is believed to cause the enhancement of ZT. When the donor or acceptor level lies near the Fermi level, the density of states is locally increased leading to an increase in carrier effective mass. If the Fermi level is close to distortion, it is theoretically expected that the Seebeck coefficient would increase. This is illustrated in Fig. 2.4. An increase in Seebeck coefficient using this approach was experimentally demonstrated in bulk Tl-doped PbTe, reaching ZT value of 1.5 at 500 °C [56].

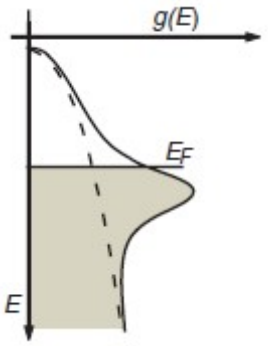

FIGURE 2.4: Schematic of the effect of the resonant level on the electronic density of states. Reprinted by permission from [56], Science.

2.4.4 Nanoscale approach

The use of nanostructures enables ZT enhancement through quantum confinement and increased influence of interfaces and surfaces specific for this dimensions. While ZT of conventional bulk thermoelectrics (Bi_2Te_3, PbTe and SiGe alloys) has remained ≈1 for a long time, theoretical and experimental results in superlattices, nanowires, nanotubes

and quantum dots have shown a great promise of a higher ZT [24]. Hicks and Dresselhaus were the first reporting a great enhancement in thermoelectric properties can be greatly enhanced in nanostructures based on their calculations [57],[58]. Since then, many publications have been stating that by decreasing the dimensions an enhancement in ZT over the bulk materials can be achieved [59, 37, 45, 38, 48, 39, 60, 61, 40, 62, 63]. Venkatasubramanian *et al.* [64] reported a ZT of 2.4 at room temperature for alternating nanostructure made of Bi_2Te_3/Sb_2Te_3 superlattice, which decreased thermal conductivity and increased Seebeck coefficient. Harman *et al.* [65] reported achieving ZT of 3.2 at 300 K in PbSeTe-based quantum dot superlattice structures due to the decrease in thermal conductivity.

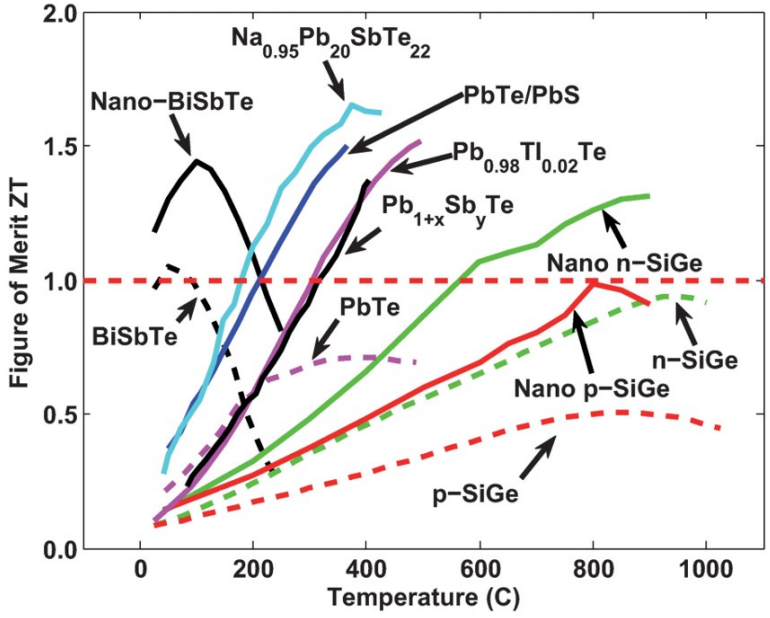

FIGURE 2.5: Comparison of ZT in state-of-the-art conventional bulk materials and nanostructured materials. Reprinted by permission from [37], Royal Society of Chemistry.

The band structure is usually represented as a simple parabolic dispersion function defining relationship between the energy and the momentum (E-k) of available quantum mechanical states for electrons in the band. This relationship for a three-dimensional semiconducting material is shown in Fig. 2.6. In an intrinsic semiconductor all the states in the valence bands are filled with electrons, and the conduction band states are empty. In an extrinsic semiconductor impurities are being introduced which can either donate additional electrons below the bottom of conduction band (n-type), or can accept valence electrons from the top of the valence band (p-type). By introducing these impurities, materials' electrical, optical and structural properties can be adjusted. The band gap (E_g) is defined as the difference in energies between the valence and conduction band, and has no available electronic states. E_g represents energy needed to elevate electron from valence to conduction band, where it can move freely and conduct electric current.

For the conduction band minimum and valence band maximum the ground state energy is set to zero, and the Fermi level (E_F) is measured with respect to ground state.

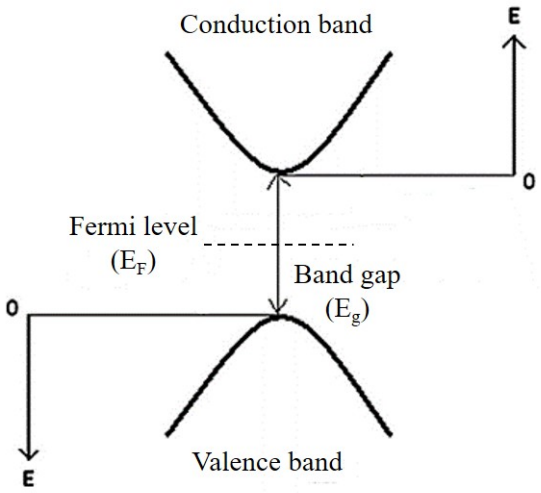

FIGURE 2.6: The energy dispersion for electrons (E) as a function of momentum (k) in conduction band and holes in valence bands. The Fermi level is positioned in the band gap (E_g) between the conduction band minimum and the valence band maximum. Reprinted by permission from [24], Elsevier.

Figure 2.7 shows density of states (DoS) for electrons in bulk (3D) material, quantum well (2D), quantum wire or nanowire (1D) and quantum dot (0D). The density of states (DoS) is defined as the number of states which can be occupied by electrons at each energy level. In the case of a bulk semiconductor, the dependence of DoS with energy is parabolic. By reducing the dimensions a change in energy dependence of DoS occurs, particularly an increase in DoS. The second effect of reducing materials dimensionality is an increase in band gap (E_g) as conduction band shifts upward and valence band downward from the ground state. This is illustrated in Fig. 2.8. Given the same carrier density, this increase in E_g will in turn increase the Seebeck coefficient (S). From the kinetic point of view, S is difference between average energy of electrons and the Fermi level. By reducing the dimensionality the average electron energy reduces but Fermi level reduces largely, resulting in increased S. These changes at reduced dimensionality could be utilised for power factor increment of nanostructured materials over their bulk counterparts [24].

Most of the understood ZT enhancement in nanostructures is attributed to the decrease in lattice thermal conductivity (κ_L). In a solid, quasi particles responsable for the heat transport are lattice modes/phonons. Because the mean free path (mfp) of electrons is much shorter than that of phonons, nanostructuring introduces a high density of interfaces to scatter phonons over a large mfp, scattering phonons more preferentially than electrons and thus leading to the reduction of κ_L while preserving carrier mobility (μ) and electronic conduction (σ). This is illustrated in Fig. 2.9. The key for this

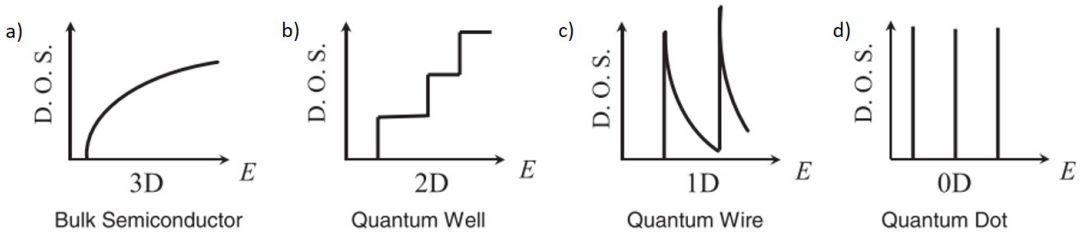

FIGURE 2.7: Electronic density of states for: a) 3D bulk semiconductor, b) 2D quantum well, c) 1D nanowire, and d) 0D quantum dot. Reprinted by permission from [59], John Wiley and Sons.

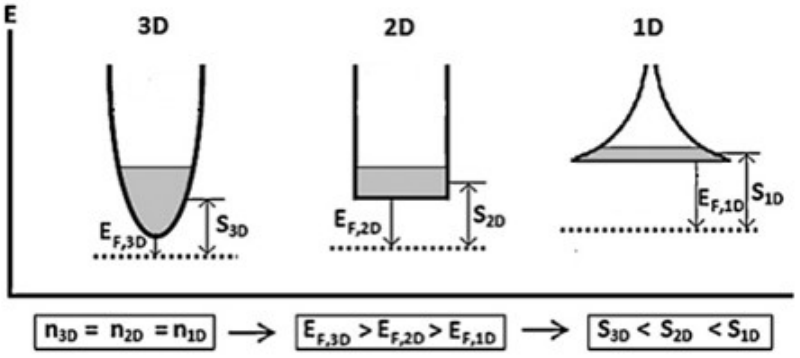

FIGURE 2.8: The shape of electronic DoS of 3D, 2D and 1D material. The conduction band shifts upwards from the ground state increasing E_g. Reprinted by permission from [24], Elsevier.

strategy is to prepare nanostructures with one or more dimensions smaller than mfp of phonons but larger than the mfp of charge carriers [24].

Thermal conductivity κ_L below the bulk alloy was reported for Si_m-Ge_n superlattices (where m and n refer to the number of monolayers) [67]. A decrease in layer thickness in 2D materials is related to increased number of interfaces per unit length, which leads to lower κ_L. Furthermore, the influence of the mean interface roughness on decreasing κ_L due to additional phonon scattering has been postulated through simulations for smaller thicknesses. Thermal measurements on Bi_2Te_3/Sb_2Te_3 superlattices have also shown a reduction in κ_L value over the bulk Bi_2Te_3, with the pronounced decrease with superlattice period < 6 nm [68].

It has been proposed that systems with a greater degree of confinement, such as nanowires or nanotubes [60], would lead to even greater phonon scattering and consequently lower κ_L than 2D systems. As in the case of superlattices, the reduction in phonon mfp through phonon-surface, phonon-boundary, phonon-phonon, and phonon-carrier scattering contribute to lower κ_L. Reduction in thermal conductivity of two orders of magnitude has been shown by simulations in Si nanowires compared to bulk Si [69]. Controlled roughness seems to contribute to the reduction in κ_L of Si nanowires, approaching the value of κ_L of amorphous SiO_2. As it would be expected, the κ_L decreases with reduction of

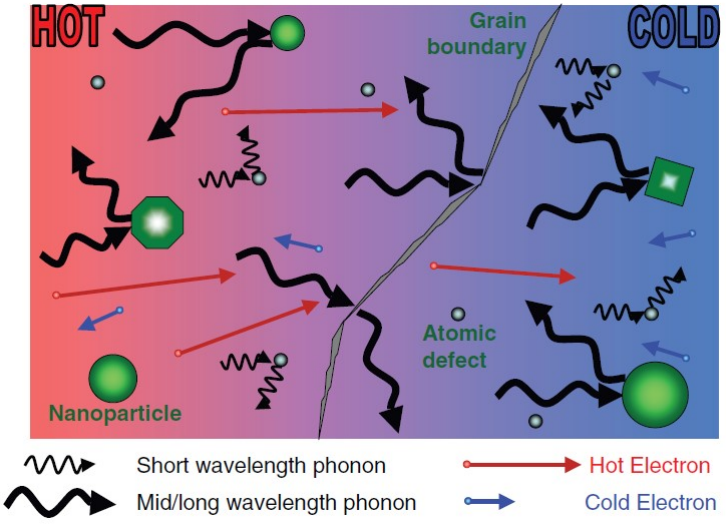

FIGURE 2.9: Schematic diagram illustrating mechanisms of phonon scattering and electronic transport of hot and cold electrons in a thermoelectric material. Reprinted by permission from [66], John Wiley and Sons.

nanowire diameter probably due to the reduction of phonon mfp and enhanced boundary scattering. Doping introduces impurities in the crystal lattice causing scattering of short wavelength phonons, while rough surface causes scattering of longer wavelength phonons [70]. Results of this study are shown in Fig. 2.10. However, the enhancement of ZT value is still close to ZT of conventional thermoelectric materials ($\approx$1). Therefore, methods for reducing κ_L might no longer have effect in enhancing ZT as the minimum seems to be reached.

Second method of ZT increase is power factor ($S^2\sigma$) enhancement via quantum confinement, as explained above. The concept is illustrated in Fig. 2.11 comparing bulk Si and Si nanowires. Firstly, by increasing the dopant concentration the carrier concentration increases (Fig. 2.11b). Consequently, the average electron energy $< E >$ and Fermi level E_F increase, but since the increase in $< E >$ is smaller than the increase E_F, there is a four-fold reduction in S (from -0.4 to -0.1 mV/K). Nevertheless, $S^2\sigma$ is enhanced by a factor of three as a result of increased carrier concentration. Secondly, by reducing the dimensionality the DoS is increased compared to the bulk material and the E_F is decreased (Fig. 2.11c). Given the same carrier concentration, the electron distribution of the nanowire is shifted towards lower energy states due to the shape of the DoS, but the E_F is decreased largely resulting in two-fold enhancement in S (from -0.1 to -0.2 mV/K). Hence, there is a four-fold increase in $S^2\sigma$.

Fig 2.11d shows that the DoS for 5 nm Si nanowire is similarly shaped as 2 nm Si nanowire, however, it has smaller magnitude compared to the bulk Si, except for a small energy range below 0.01 eV. Therefore, the E_F of 5 nm nanowire is higher than the E_F of the bulk material leading to much smaller S, which consequently reduces the $S^2\sigma$ in comparison to the bulk Si. In conclusion, there is an enhancement of $S^2\sigma$ when the

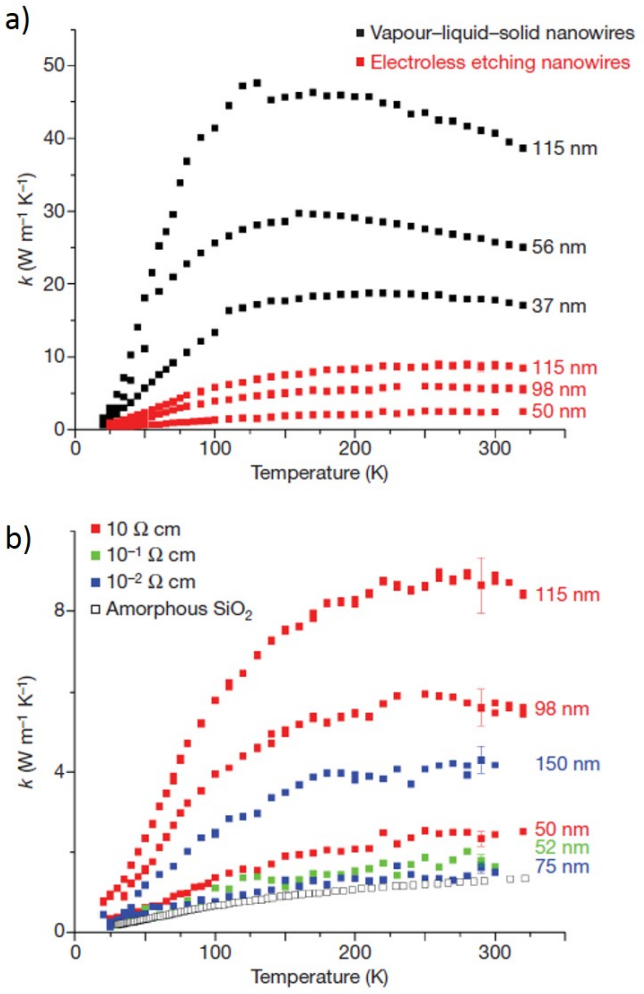

FIGURE 2.10: Decrease in κ_L with diameter of nanowires. a) The temperature dependent κ of VLS (smooth surface) nanowires and EE (rough surface) nanowires. b) The temperature dependent κ of EE nanowires etched from wafers with different resistivities. The smaller diameter highly doped EE Si nanowires have κ approaching the value of amorphous SiO_2. Reprinted by permission from [70], Springer Nature.

diameter of the nanowire is sufficiently small that the DoS becomes larger than is the bulk material.

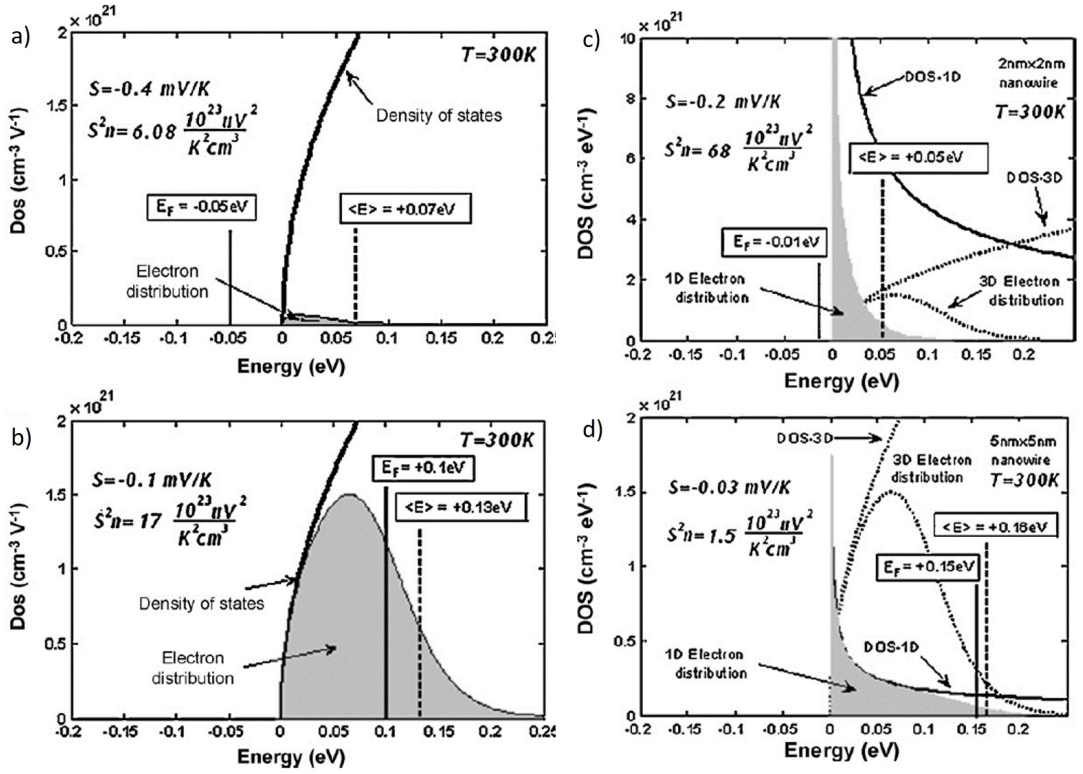

FIGURE 2.11: Electrons density distribution (grey area) of a, moderately doped (E_F=-0.05 eV, n=3.8 x 10^{18}/cm^3) and b, highly doped (E_F=0.1 eV, n=1.7 x 10^{20}/cm^3 bulk Si. S is proportinal to $< E >$-E_F. c, 2 nm and d, 5 nm Si nanowires, with dopand/carrier concentration in both cases same as in bulk Si (b). Reprinted by permission from [24], Elsevier.

2.5 Thermoelectric generator

Thermoelectric couple consists of n-type (negatively charged) and p-type (positively charged) semiconducting materials. The couple uses temperature difference along the semiconducting materials to induce the current flow based on the Seebeck effect in order to power an electric load through the external circuit (Fig. 2.12a). In a Peltier cooler a DC current flows through the couple, carrying heat from one side to the other enabling cooling of the top surface based on the Peltier effect (Fig. 2.12b) [4].

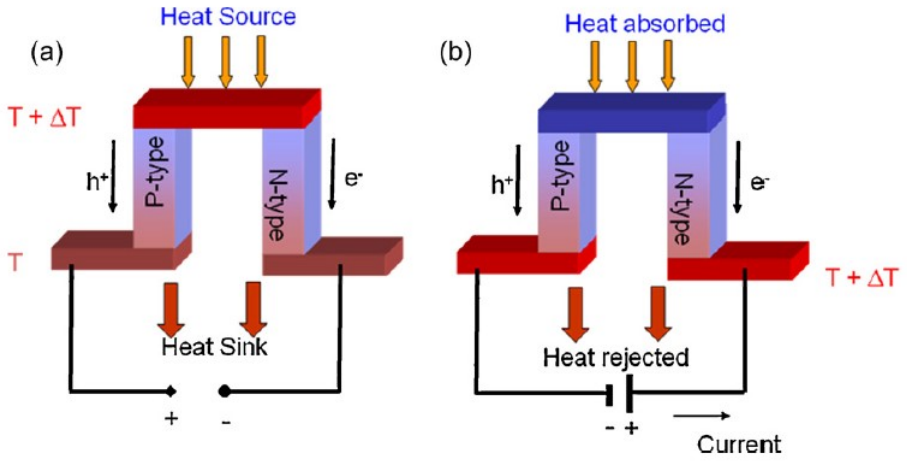

FIGURE 2.12: A thermoelectric couple based on a) Seebeck effect for conversion of heat to electricity, and b) Peltier effect for cooling. Reprinted by permission from [24], Elsevier.

Thermoelectric generator is a solid state device that converts heat directly into electricity based on the Seebeck effect. The device is made of many couples connected electrically in series and thermally in parallel, as shown in Fig. 2.13.

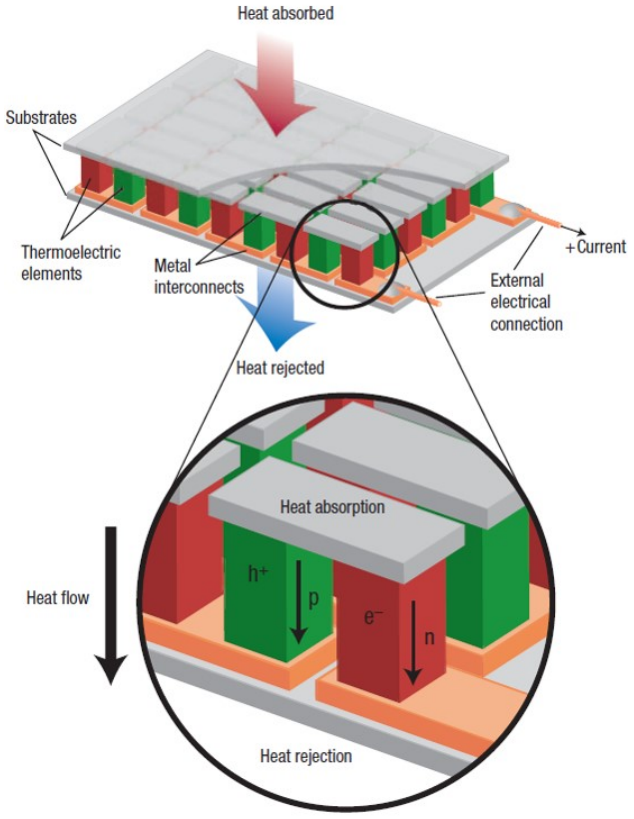

FIGURE 2.13: Thermoelectric device showing the direction of charge flow. Reprinted by permission from [4], Springer Nature.

Chapter 3

Theory of Electrodeposition

3.1 Electrode potential

If a metal electrode is immersed into electrolyte solution which contains ions of that metal, an exchange of metal ions between the solid metal and the solution will occur. From the solid metal's crystal lattice some ions will be dissolved into the solution and some ions from the solution will enter the crystal lattice. One of these reactions could occur faster than the other. In the case of more metal ions leaving the crystal lattice, an excess of electrons will build up at the metal's surface charging the metal side of the interphase negatively. As a response to the negative charging of metal electrode surface, positively charged metal ions from the solution will be attracted to the metal's surface and the negatively charged anions will be repelled. As a result of this the excess of positive metal ions, the rate of positive ions leaving the crystal lattice will slow down due to the repulsion of ions, and the rate of ions entering the crystal lattice will accelerate. Therefore, after a certain amount of time, an equilibrium between metal ions leaving and entering the crystal lattice will from. This equilibrium can be expressed by Eq. 3.1.

$$M^{z+} + ze^{-} \rightleftharpoons M \tag{3.1}$$

where M^{z+} is a positively charged metal ion, z is the number of electrons exchanged in the reaction, and M is a metal. The reaction from left to right represents consuming electrons and is called reduction. The reaction from right to left releases electrons and is called oxidation. The interphase between the metal electrode and the solution is neutral at the equilibrium, and can be expressed by Eq. 3.2.

$$q_{\mathrm{M}} = -q_{\mathrm{S}} \tag{3.2}$$

where q_M is the charge per unit area on the metal side of the interphase, and q_S is charge per unit area on the solution side of the interphase. As a result of charging at the interphase, the potential difference between the potentials of metal and the solution forms, which is defined by Eq. 3.3

$$\Delta\phi = (M, S) = \phi_{\mathrm{M}} - \phi_{\mathrm{S}} \tag{3.3}$$

where $\Delta\phi$=*(M,S)* is potential difference at the interphase, ϕ_M is potential of the metal and ϕ_S is potential of the solution. In order to measure this potential difference of the metal electrode/solution interphase, the metal electrode needs to be connected to a reference electrode which has a stable and well-known potential, forming in this way an electrochemical cell. The potential of M^{z+}/M electrode is a function of concentration of metal ions in the solution, and can be expressed by Nernst eq. 3.4

$$E = E^{\circ} - \frac{RT}{zF} lnc(M^{z+}) \tag{3.4}$$

where E is the electrode potential, E° is standard electrode potential and c is concentration of the solution. R, T, z and F are the gas constant (8.314 J mol^{-1} K^{-1}), absolute temperature, number of electrons exchanged in the reaction, and Faraday's constant (96 485 C mol^{-1}), respectively. The standard electrode potential (E°) is obtained by forming an electrochemical cell of standard hydrogen electrode and the electrode under investigation at 25 °C. The standard hydrogen's electrode potential at the conditions of p=1 atm and $c(H^+)$=1 M is zero by convention [71].

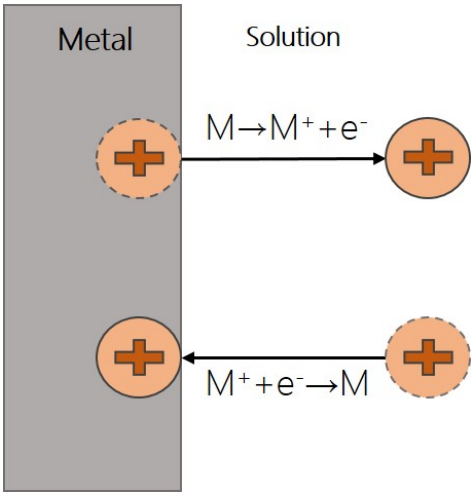

FIGURE 3.1: Formation of equilibrium state at metal/solution interphase.

3.2 Electrochemical cell

An electrochemical cell is composed of three electrodes: working, counter and reference electrode, immersed in an electrolyte solution. Working electrode is electrode of our interest, and in case of electrodeposition that is the cathode. Cathode is negatively charged by an external power supply, and it will attract positively charged ions which consume electrons and are deposited on electrode surface. This reaction is called reduction, and can generally be expressed by Eq. 3.5

$$A^{+} + e^{-} \rightarrow A \tag{3.5}$$

Counter electrode is positively charged electrode at which compensating reaction oxidation occurs, and in case of electrodeposition that is anode. Oxidation reaction can generally be expressed by Eq. 3.6

$$B^{-} \rightarrow B + e^{-} \tag{3.6}$$

Reference electrode is an electrode which has stable and well-known electrode potential, and serves to monitor the potential at working electrode. A schematic representation of an electrochemical cell is shown in Fig. 3.2.

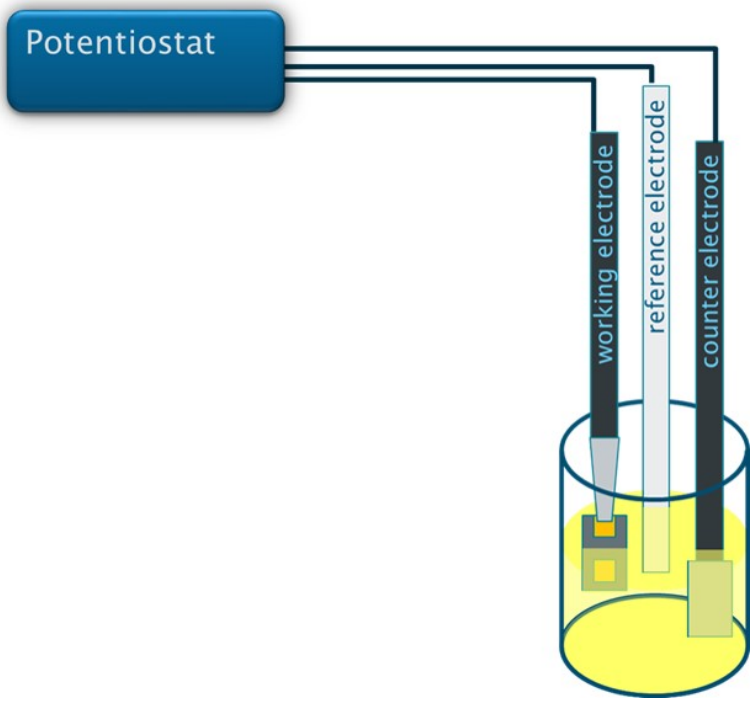

FIGURE 3.2: Schematic of an electrochemical cell containing working, counter and reference electrode immersed in an electrolyte solution and connected to the potentiostat.

3.3 Electrodeposition mechanism

Electrodeposition is an electrochemical synthesis method in which a film of solid metal or semiconductor is deposited from a solution of ions onto an electrically conducting surface (an electrode). When the electrodes are connected in electrochemical cell and the current is flowing through the cell, working electrode's potential will differ from its equilibrium potential (potential at which the same number of ions enter and leave the crystal lattice on the electrode; there is no net reaction). The difference between the equilibrium potential (E_{eq}) and a potential (E) of the electrode as a result of current flowing is called overpotential (η), as shown is Eq 3.7.

$$\eta = E - E_{\mathrm{eq}} \tag{3.7}$$

In the case of large negative overpotentials ($\eta \geq$100 mV), the current density increases exponentially with overpotential (η) according to Eq. 3.8

$$i = -i_0 e^{-\alpha z f \eta} \tag{3.8}$$

where i is the current density defined as i=I/S (s is the surface area of the electrode), i_0 is exchange current density in equilibrium potential, α is the transfer coefficient, and f is defined as:

$$f = \frac{F}{RT} \tag{3.9}$$

where F is the Faraday constant, R is the gas constant and T is the absolute temperature. The exponential relationship between the current density and the overpotential indicates that even small change in overpotential causes large change in current density. This relationship defined by Eq. 3.8 is valid if the charge transfer process (Eq. 3.1) is the rate-determining step (the slowest process). If the deposition reaction is limited by the transport of metal ions from the solution to the electrode surface, there is a limiting (maximum) current density defined by the Eq. 3.10

$$i_{\mathrm{L}} = \frac{zFD}{\delta} c_{\mathrm{b}} \tag{3.10}$$

where z is the number of electrons exchanged in reaction, F is the Faraday constant, D is the diffusion coefficient of the depositing specie, c_b is the concentration of ions in the bulk of the solution. The relationship between current density and the potential for purely activation controlled region and mixed activation and mass transport region is shown in Fig. 3.3. When the current density is at the limiting (maximum) value

the ionic species are reduced as soon as they reach electrode surface. Hence, at these conditions the concentration of ionic species at the electrode surface is zero, and the rate of deposition is controlled by the rate of ionic species transport to the electrode surface.

There are three main stages recognised for electrodeposition:

1. *Ionic migration.* The migration of solvated ions towards the working electrode under the influence of the applied potential.
2. *Electron transfer.* The solvated ions enter the diffusion layer at the working electrode surface. Due to the high electric field present, the ions lose their solvated shell. At the electrode surface, ions are neutralised by consuming electrons and adsorbed.
3. *Incorporation.* The adsorbed atoms are incorporated into the crystal lattice at the electrode surface.

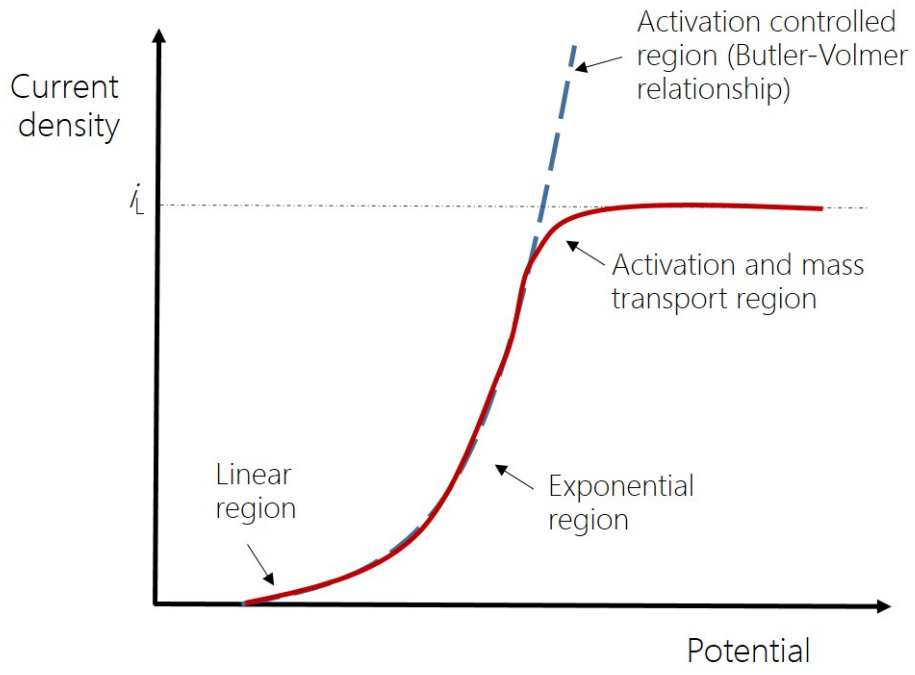

FIGURE 3.3: Regions in general current-potential relationship.

In the case of formation of Bi_2Te_3 compound by electrodeposition in dichloromethane, Bi is introduced as $[N^nBu_4][BiCl_4]$ and Te as $[N^nBu_4]_2[TeCl_6]$ precursor. Bi^{3+} from $[BiCl_4]^-$ and Te^{4+} from $[TeCl_6]^{2-}$ are both electrodeposited onto working electrode. The involved reduction reactions can be expressed by Eq. 3.11 and 3.12

$$Te^{4+} + 4e^- \longrightarrow Te/ \times 3 \tag{3.11}$$

$$Bi^{3+} + 3e^- \longrightarrow Bi/ \times 2 \tag{3.12}$$

The deposition potential is the potential at which deposition occurs. As discussed earlier, it is determined by standard electrode potential (E°) and the concentration of ionic species in the solution. The electrochemical cell potential is a sum of potentials for individual species being electrodeposited, and is then given by Eq. 3.13

$$E = E^{\circ'} - \frac{RT}{18F} ln[\frac{1}{c(Bi^{3+})c(Te^{4+})}] \tag{3.13}$$

where $E^{\circ'}$ is sum of the E° for reactions described in Eq. 3.11 and 3.12. It is important to ensure that reactions described in Eq. 3.11 and 3.12 occur simultaneously, which will occur if the potentials of the two reactions should be the same, or nearly the same. If the deposition potentials of individual ionic species greatly differ, the only way to achieve the co-deposition is by changing the concentrations of individual ionic species in the solution [71]. Often the $E^{\circ'}$ for the various species in a solvent being used is unknown, thus the solution to this problem is use of cyclic voltammetry.

3.4 Cyclic voltammetry

Cyclic voltammetry (CV) is a type of potentiodynamic electrochemical measurement. In this technique, the potential applied to working electrode is linearly increased and the current is monitored as a function of the applied potential. After the set potential at working electrode is reached, the potential is then applied in the opposite direction to return to the initial value. The potential is being measured between the working and the reference electrode, while the current is being measured between the working and the counter electrode.

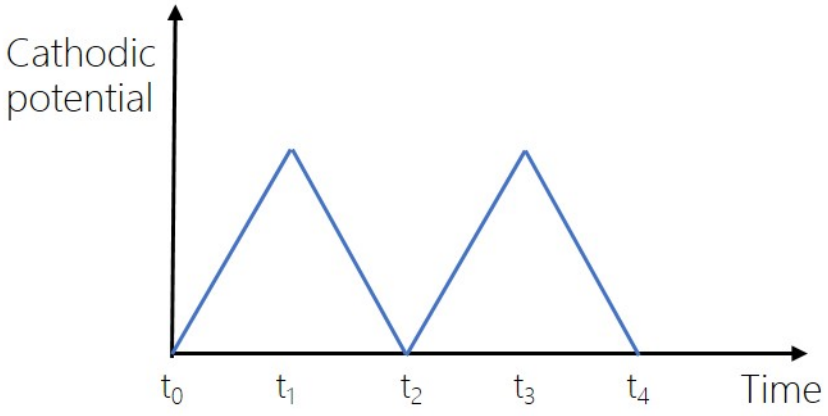

FIGURE 3.4: Cyclic voltammetry waveform. The potential is linearly increased until t_1 where is reversed until t_2. The same cycle is then repeated (from t_2 to t_4).

During the initial forward scan (from t_0 to t_1 in Fig. 3.4) when linearly increasing potential is applied, the cathodic current will increase reaching the peak cathodic current

(I_{pa} in Fig. 3.5). At the point where the peak reduction potential is reached, the cathodic current will start to decrease as the concentration of the specie being reduced is depleted. During the reverse scan (from t_1 to t_2 in Fig.3.4), the reduced specie will start to oxidise which will give rise to anodic current. The anodic current will increase until it reaches peak anodic current (I_{pa} in Fig. 3.5) where it starts to decrease as the concentration of the specie being oxidised is depleted.

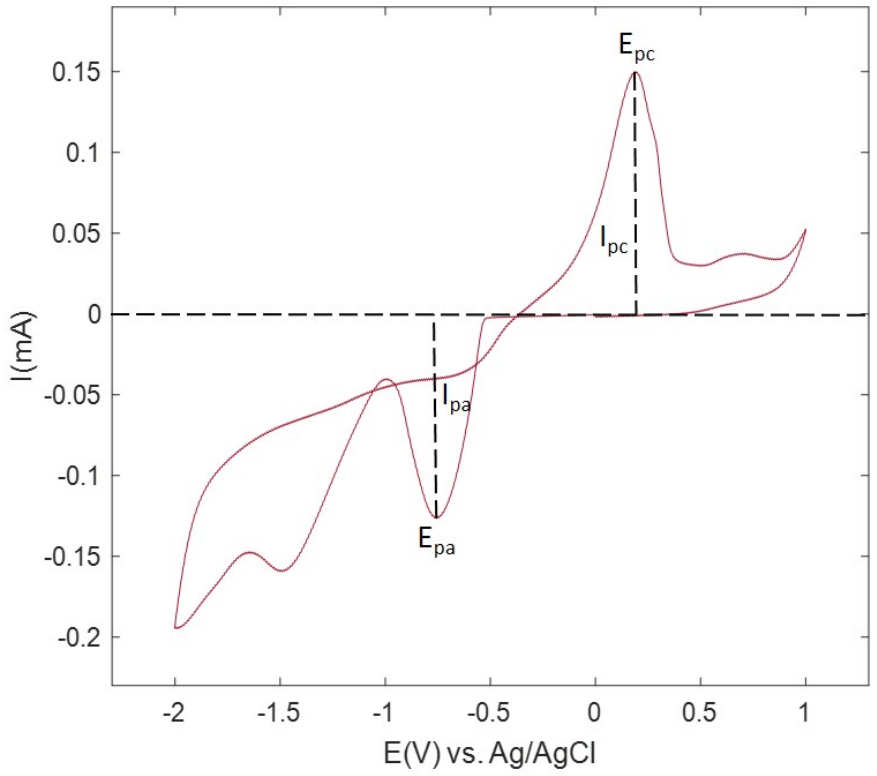

FIGURE 3.5: Cyclic voltammogram of 2.5 mM $[N^nBu_4][BiCl_4]$, 3 mM $[N^nBu_4]_2[TeCl_6]$ and 0.1 M $[N^nBu_4]Cl$ in CH_2Cl_2 solution on 3 mm diameter GC electrode. The image represents the first scan, where I_{pc} and I_{pa} represent the peak cathodic and anodic current, respectively.

The cycles can then be repeated, giving the series of I-V plots and the conditions under which elements can be deposited. Figure 3.6 shows three consecutive scans in electrochemical window from -2.0 to 1.0 V vs. Ag/AgCl. Several reduction and oxidation peaks can be observed, corresponding to different reactions in the solution at different potentials. The first scan (black curve) represents electrodeposition onto a foreign substrate. The second and the third scan (red and blue curve, respectively) represent repeated cycles and deposition onto an already deposited material, and hence differ from the first curve. The position of the reduction peaks gives information about deposition potentials for a given system [72].

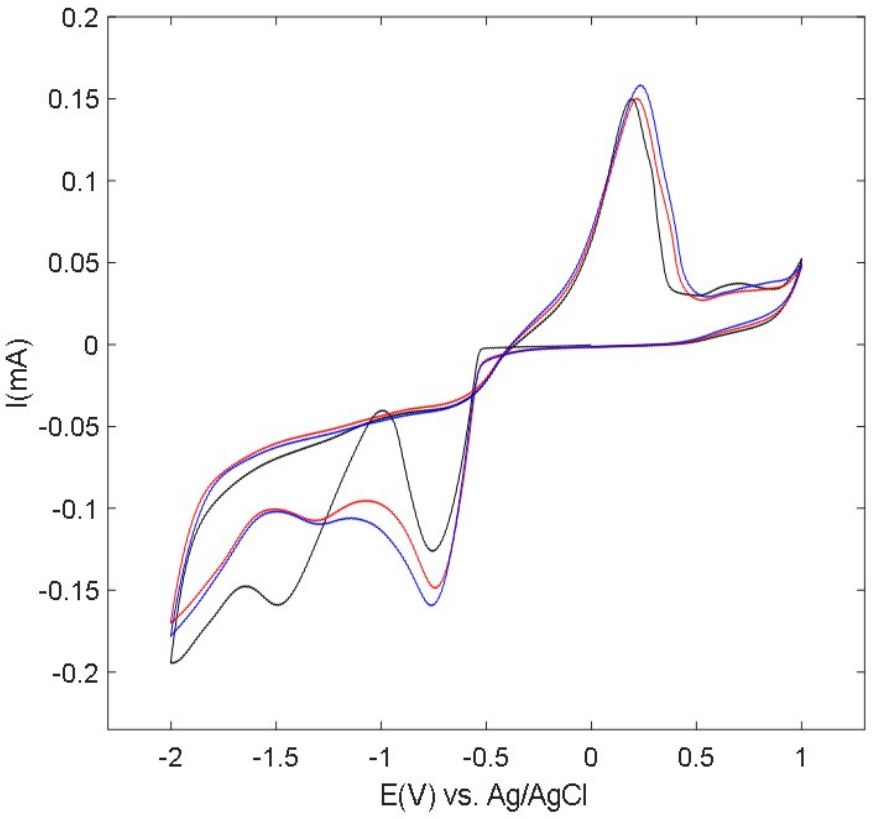

FIGURE 3.6: Cyclic voltammogram for the reduction of 2.5 mM $[N^nBu_4][BiCl_4]$, 3 mM $[N^nBu_4]_2[TeCl_6]$ and 0.1 M $[N^nBu_4]Cl$ in CH_2Cl_2 solution on 3 mm diameter GC electrode. Black curve: 1^{st} scan, red curve: 2^{nd} scan, blue curve: 3^{rd} scan.

3.5 Potentiostatic and pulse deposition techniques

During potentiostatic electrodeposition, a constant overpotential over a certain period of time is supplied to the working electrode (Fig. 3.7a). Initially, before electrodeposition, the concentration of ions is homogeneous at all distances from the working electrode (equal to the bulk concentration). When the constant potential is applied to the working electrode, the ions in close vicinity to the electrode surface are being consumed and the concentration is decreasing. As the reaction at electrode surface proceeds, the constant consumption of reactants causes a depletion of ions, and the depletion layer forms. Hence, the concentration of reactants is a function of distance from the working electrode. As explained above, the current reaches maximum (limiting) value and the deposition rate is controlled by the rate of transport of ions to the working electrode. A diffusion layer (δ) is formed as a result of ion depletion, defined by the Nernst diffusion-layer model (Fig. 3.8). According to this model, the concentration of ions has a bulk value up to the distance (δ) from working electrode surface where it starts falling linearly to zero at the electrode surface, and the ions must diffuse through the diffusion layer to reach the electrode surface. The model assumes that the liquid layer of thickness δ is

stationary. At these conditions the rate of the deposition is controlled by the rate of the reactant transport to the electrode surface.

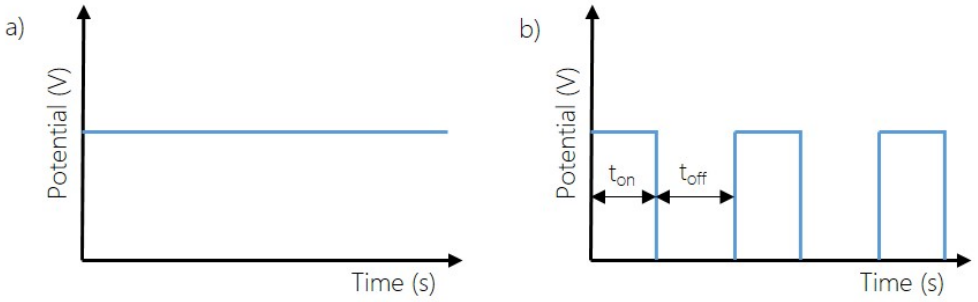

FIGURE 3.7: a) Potentiostatic and b) pulsed electrodeposition. t_{on} is the on period of pulse and t_{off} is the off period.

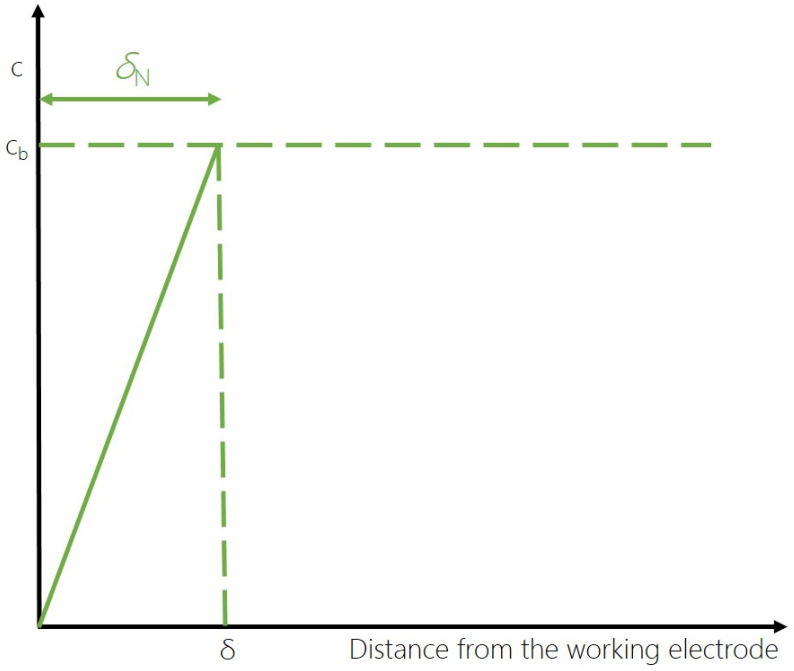

FIGURE 3.8: Schematic of the concentration profile at the working electrode for electrodeposition. δ_N is the Nernst diffusion layer thickness, c_b is the concentration of the reactanct in the bulk.

Pulsed electrodeposition is performed by alternating a constant potential (E_{on}) for a certain period of time (t_{on}), and the open circuit potential (E_{off}=OCP) for period t_{off} (Fig.3.7b). An important effect of this technique is modification of the Nernst diffusion layer, which is illustrated in Fig.3.9. At pulsing conditions the Nernst-diffusion-layer is split into pulsating diffusion-layer (δ_P), which is in the immediate vicinity of the working electrode where the ion concentration pulsates with the frequency of the pulsating current, and the stationary diffusion-layer δ_S. Hence, at these conditions there is no depletion layer as concentration of ions is being replenished during off-time. The pulsed deposition is mostly employed to obtain improved distribution of deposits grown potentiostatically. Furthermore, the deposits obtained by square pulse deposition usually

exhibit finer grains and lower porosity that those obtained by potentiostatic deposition because of high pulse current density resulting and high nucleation rate. This grain refinement comes from the blocked diffusion paths due to a high adion concentration during square wave pulsed deposition resulting in decreased surface mobility, while during the potentiostatic deposition the adion mobility is high developing crystalline structures [71].

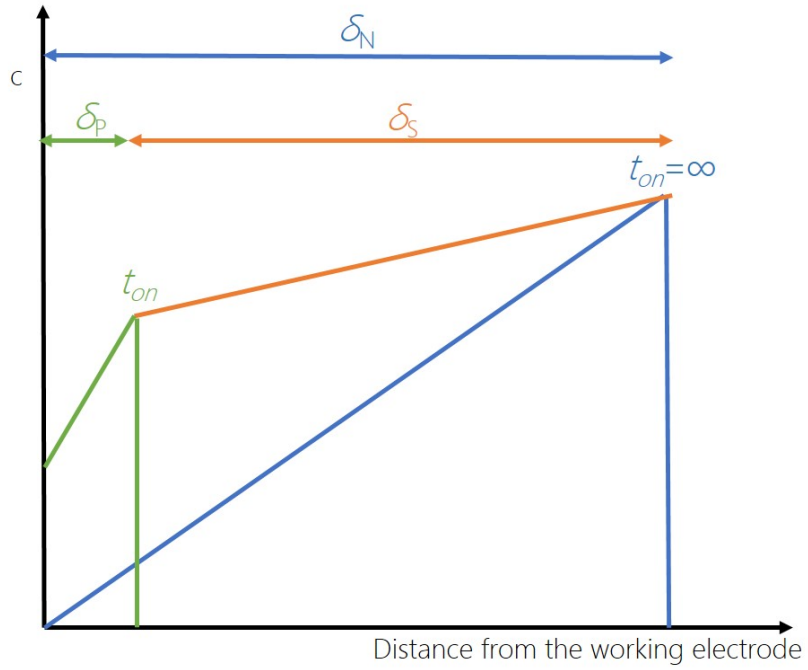

FIGURE 3.9: Schematic of the concentration profile at the working electrode for square pulsing and potentiostatic conditions. δ_P is the pulsating diffusion layer thickness, δ_S is the stationary diffusion layer thickness, δ_N is the Nernst diffusion layer thickness.

3.6 Nucleation and thin film growth

There are two fundamental processes in the formation and growth of adion clusters: 1) arrival and adsorption of ions at the electrode surface, and 2) the movement of the adsorbed ions at the electrode surface. The adion deposited to a foreign substrate is an unstable entity, but increases its stability by forming a cluster of ions. After a maximum of free energy of formation of a cluster is reached, the spontaneous growth of clusters is possible. This critical cluster is a nucleus of a new phase on a foreign substrate, characterised by equal possibility for growth and dissolution. A probability with time t of converting a site on the metal electrode into a nucleus is given by the nucleation law (Eq. 3.14).

$$N = N_0(1 - e^{-At}) \tag{3.14}$$

where N_0 is the number of maximum possible nuclei on the unit surface, A is the nucleation rate constant. Two cases are possible for the initial stage of nucleation (at low t value), instantaneous and progressive nucleation. For the instantaneous nucleation, large nucleation constant A reduces Eq. 3.14 into:

$$N \simeq N_0 \tag{3.15}$$

Instantaneous nucleation indicates that all electrode sites are converted to nuclei instantaneously, and the nuclei continue to grow during the deposition. In the case of progressive nucleation, small nucleation constant A reduces Eq. 3.14 into:

$$N \simeq AN_0t \tag{3.16}$$

For the progressive nucleation, the number of nuclei is a function of time t meaning that the new nuclei are formed while the deposition progresses. Figure 3.10 shows potentiostatic current-time transient of Bi_2Te_3 electrodeposition from dichloromethane. The potentiostatic transient curve can be divided into three regions. In the first region at the beginning the current declines. This region corresponds to double-layer charging current (i_{DL}). In the second region the current increases, which can be due to the growth of either independent nuclei (instantaneous nucleation) or simultaneous growth of independent nuclei and formation of new nuclei (progressive nucleation). This deposition current is without the overlapping effect of the nuclei (i_{free}). In the case of instantaneous nucleation the current i_{free} increases linearly with time, and in the case of progressive nucleation the current i_{free} increases at t^2. In the third region, two opposing effects occur: the growth of independent nuclei and merging (overlapping). As a result of the two opposing effects, there is an increase in current reaching the maximum value (i_{max}), after which it starts decreasing in the third region (i_{overlap}). Hence, the current increases until the nuclei begin overlapping, after which it starts to decrease. This current decay is due to the decrease in effective electrode surface area [73].

The two basic mechanisms for a deposit formation are: layer (2D) growth (Fig. 3.11a,b) and three-dimensional (3D) crystallites growth (growth by coalescence of formed nuclei, Fig 3.11c). In the layer growth mechanism, a crystal spreads in the form of layers one after the other over the electrode surface. The growing layers, or steps, can be achieved in electrodeposition of metal thin films. In the 3D nuclei-coalescence mechanism, the 3D crystallites are the structural components, and the deposits are made by coalescence (merging) of these crystallites. The 3D growth sequence by electrodeposition via nuclei-coalescence is consisted of the following stages:

- Formation growth of isolated nuclei to 3D crystallites.

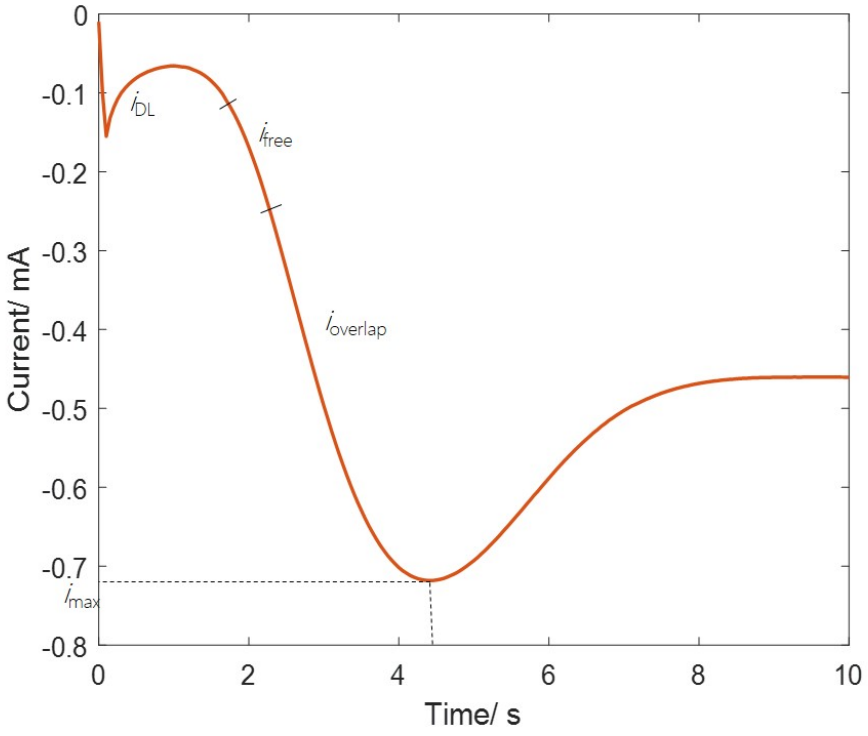

FIGURE 3.10: Potentiostatic current-time transient of electrodeposition of Bi_2Te_3 from 2.25 mM $[N^nBu_4][BiCl_4]$, 3 mM $[N^nBu_4]_2[TeCl_6]$ and 0.1 M $[N^nBu_4]Cl$ in CH_2Cl_2 solution at -1.0 V vs. Ag/AgCl on TiN electrode.

- Coalescence (merging) of 3D nuclei.
- Formation of linked network of 3D crystallites.
- Formation of continuous deposit.

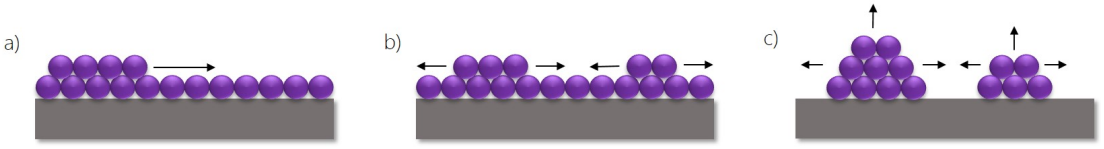

FIGURE 3.11: Schematics of 2D layer growth (a,b) and 3D nuclei-coalescence growth (c).

The deposited atoms in the solid state are in the three-dimensional regular pattern. If the periodicity of the pattern extends throughout the material, the structure is described as *single crystal*. If the periodicity of the material is interrupted by grain boundaries, the structure is called *polycrystalline*. The size of the grains throughout the structure can vary greatly. If the size of crystallites or grains is comparable to pattern unit size, the material is described as *amorphous*. The grains are referred to individual crystallites incorporated in a polycrystalline material. The repetitive three-dimensional pattern of a crystalline material (single-crystal or polycrystalline) is called lattice [71].

3.7 Faraday's law

The amount of material deposited per unit of time is given by the Faraday's law of electrolysis. The mass of deposited material can be expressed by Eq. 3.17

$$m = \frac{MQ}{zF} \tag{3.17}$$

where M is the molecular mass, Q is the electrical charge, z is the number of transferred electrons and F is the Faraday constant (F= 96 485 C/mol). The volume of deposited material can be expressed by Eq. 3.18

$$V = \frac{MQ}{\rho zF} = Al \tag{3.18}$$

where ρ is the density of the material, A is the area of deposition and l is the deposit thickness. For practical applications we are interested in the weight of material deposited onto cathode. Therefore, we define the current efficiency (CE) by the Eq.3.19

$$CE = \frac{M_{\mathrm{a}}}{M_{\mathrm{t}}} \times 100 \tag{3.19}$$

where M_{a} is the actual amount of the deposited material, and M_{t} is the theoretically calculated amount of material from Faraday's law [71], [73].

3.8 Electrodeposited bismuth telluride thin films

Currently, there is a range of fabrication techniques being used for thin film fabrication, such as sputtering, chemical vapour deposition (CVD), pulse laser deposition (PLD), molecular beam epitaxy (MBE), evaporation and electrodeposition. In comparison to other methods for thin film fabrication, electrodeposition has advantages of being relatively cost-effective as it does not require high vacuum and elevated temperatures, easier control over thickness and composition, and deposition of films with thicknesses ranging from nanometers to hundreds of micrometers over a large area.

Electrodeposition of bismuth telluride thin film has been well studied and so far the material has been deposited by different electrochemical methods, such as potentiostatic electrodeposition [8][9][10][11][12][13], galvanostatic electrodeposition [14] and pulsed electrodeposition [15][16][17][18]. The most popular method is potentiostatic electrodeposition from nitric acid electrolyte containing Bi^{3+} and $HTeO_2{}^+$, which was studied extensively in [19]. Besides nitric acid, other inorganic acids were investigated for potentiostatic and galvanostatic electrodeposition. Heo *et al.*[10] studied electrodeposition from sulfuric acid aqueous solution on Au working electrode of $Bi_2(SO_4)$ and K_2TeO_3 at constant potential obtaining films with a dense and smooth surfaces. The obtained Seebeck coefficient is about -100 μV/K, the conductivity 500-1000 S/cm and the carrier concentration 6.6×10^{20} cm^{-3}. The unexpectedly high Seebeck coefficient is thought to be due to high crystallinity of the films with strongest [1 1 0] peak. Kang *et al.*[12] studied electrodeposition of Bi_2Te_3 in nitric and hydrochloric acid solutions on Au working electrode. In comparison to nitrate bath, the reduction of Bi^{3+} cation was retarded but the reduction of Te^{4+} was promoted in hydrochloric acid. The deposits electroplated in HNO_3 bath exhibit closely stoichiometric composition, while the composition of deposits from HCl bath strongly depends of deposition potentials and Te-rich films were obtained. Furthermore, the morphology of deposits grown in HCl bath is featureless and smoother than deposits grown in HNO_3 which exhibit needle-like morphology, and the films grown in HCl exhibit higher Seebeck coefficient (-100 μV/K) and resistivity (65.2 μ m) than the films grown in HNO_3 (-72.3 μV/K and 7.1 μ m, respectively). However, the carrier concentration and mobility of the films grown in HCl bath are one-third of values obtained for films grown in HNO_3, which makes the power factor of the films grown in HCl bath smaller than films grown in HNO_3 The films possess strong strong [1 1 0] orientation. Matsuoka *et al.*[14] investigated galvanostatic Bi_2Te_3 electrodeposition from hydrochloric acid-based electrolyte on Ni working electrode. The film with a close stoichiometric composition surface morphology is rough with dendritic growth, and the film exhibited Seebeck coefficient of -90 μV/K but a low electrical conductivity (390.2 S/cm). The films possess the strongest [0 1 5] diffraction peak. A significant increase in Seebeck coefficient was accomplished by electrodeposition on a Bi_2Te_3 seed layer. Yoo *et al.*[74] grown n-type Bi_2Te_3 thin film potentiostatically from nitric acid bath on a sputtered Bi_2Te_3 seed layer achieving the highest Seebeck coefficient of -188.5 μV/K for

a stoichiometric film after annealing at 250 °C for 2 h. The measured resistivity of the films is 2.95-4.58 m cm, and the carrier concentration 1.8-5.6×10^{20}. Takashiri *et al.*[75] investigated electrodeposition of Bi_2Te_3 thin film under galvanostatic conditions from nitric acid bath on a sputtered Bi_2Te_3 seed layer followed by annealing at 300 °C for 1 h, which is the optimum annealing temperature giving improved thermoelectric performance as reported previously [76]. The obtained films exhibited Seebeck coefficient of about -90 μV/K and a high electrical conductivity of about 600 S/cm.

Due to the diffusion coefficients of Bi^{3+} and $TeO_2{}^{+}$ ions in aqueous solutions, electrodeposition of Bi_2Te_3 thin films is a diffusion-controlled process [17]. Hence, by applying pulsed electrodeposition technique for Bi_2Te_3 thin film growth the films' composition and morphology can be modified. Ma *et al.*[15] studied the effect of pulsed electrodeposition of Bi_2Te_3 from nitric acid solution on stainless steel compared to the films grown potentiostatically. The films obtained by pulsed electrodeposition exhibit improved, less porous morphology compared to the films grown potentiostatically. The highest Seebeck coefficient of films grown by pulsed electrodeposition is -58.3 μV/K, which is higher than the Seebeck coefficient of the film grown under constant potential (-51.9 μV/K), and the electrical resistivity of the films grown by pulsed electrodeposition is 9.65 $\mu\Omega$m, lower than electrical resistivity of the film grown potentiostatically (23.2 $\mu\Omega$m). In addition, the [0 1 5] diffraction peak is of the highest intensity for the films grown up to 20 s, while after deposition at 300 s the [1 1 0] peak becomes more intense. Zhou *et al.*[17] studied the effect of off-to-on ratio on thermoelectric performance of Bi_2Te_3 thin films grown by pulsed electrodeposition in nitric acid solution on Au working electrode. It was found that a large off-to-on ratio is advantageous for improving the surface morphology and obtaining stoichiometric films which consequently improves the thermoelectric performance of the film. The optimum off-to-on ratio is 50 yielding a film with reduced grain sizes and surface roughness compared to smaller ratios, Seebeck coefficient of -95 μV/K and electrical conductivity of 420 S/cm. The highest intensity peak is of [1 1 0] diffraction. Manzano *et al.*[16] studied anisotropic effects on thermoelectric properties of [1 1 0] oriented Bi_2Te_3 films obtained by pulsed electrodeposition from nitric acid bath on Au working electrode. In bismuth telluride crystal structure is anisotropic, while the Seebeck coefficient is nearly isotropic. Due to the anisotropic thermoelectric properties of Bi_2Te_3, the orientation parallel to *c-axis* ([1 1 0] orientation) exhibits the best thermoelectric performance in bulk material. The results showed the in-plane electrical resistivity of 15.0±1.5 $\mu\Omega$m and the Seebeck coefficient of -58±4 μV/K, while the out-of-plane electrical conductivity is higher approximately by a factor of five ((3.2±0.4)×10^{-1} S/cm) with the Seebeck coefficient nearly the same (-50±5 μV/K). The ratio between out-of-plane and in-plane figures of merit is approximately 1.8.

Bi_2Te_3 thin films have also been successfully electrodeposited from non-aqueous electrolytes which have advantage of a wider electrochemical window than water allowing the investigation of more negative overpotential on Bi_2Te_3 electrodeposition without

the reduction of solvent. Also, organic solvents allow improved solubility of Bi(III) and Te(IV) salts moderately soluble in acidic media which limits the deposition rate. Abellan *et al.*[20] electrodeposited Bi_2Te_3 thin films from dimetylsulfoxide (DMSO) containing $Bi(NO_3)$ and $TeCl_4$ as precursors by pulsed electrodeposition. A set of constant overpotentials were applied and the current transients were recorded. A detailed chronoamperometric study was conducted in order to obtain the best conditions for growing films of good quality. The nucleation and growth mechanism analysis from current transients showed that the transients have an induction time for the formation of nuclei which decrease as the applied potential is more negative. The current density decreases after the induction time until reaching an approximately constant value. By applying more negative potentials, the current reaches a maximum which indicates a coalescence of nuclei. Afterwards, the current density decreases reaching a constant value which indicates a diffusion process. The fitting of the transients was performed at different potentials including 2D and 3D nucleation process. The simulations showed that less negative overpotential (-0.35 V vs. Ag/AgCl) at short times there is 2D instantaneous nucleation controlled by the charge transfer, and at longer times there is a 3D instantaneous nucleation controlled by charge transfer but there is no contribution related to 3D instantaneous nucleation controlled by diffusion at this potential. By applying a more negative overpotential at longer times there is a contribution of growth controlled by a diffusion process. Therefore, the conditions under which a 2D layer-by-layer growth process controls the deposition are chosen resulting in a homogeneous films. The obtained film is n-type exhibiting uniform granular morphology, with carrier density concentration of 2.856×10^{18} cm^{-3}. Nguyen *et al.*[21] investigated potentiostatic electrodeposition of Bi_2Te_3 from ethylene glycol containing $Bi(NO_3)$ and $TeCl_4$ as precursors at the temperature range from 35 to 100°C. It was found that the film composition and morphology is sensitive to the temperature of deposition. The films deposited at 35°C have small grains with very little needles, the films deposited 50 and 70°C exhibit the same needle-like morphology with bigger grains for films deposited at 70°C, while the films deposited at 100°C show a very rough surface. The compositions of the films deposited at temperatures below 70°C are very similar, depending on electrolyte concentration, while at 100°C the Te content drops. In addition, the agitation is found to influence the composition of the films so that Te content increases with increasing the rotation speed and almost pure Te films are grown when rotation is faster than 200 rpm. The stoichiometric Bi_2Te_3 films were obtained with a uniform, needle-like morphology as in aqueous solutions. The highest Seebeck coefficient of as-deposited film is +240 μV/K. Wu *et al.*[22] studied electrodeposition of Bi_2Te_3 films from chloride-free ethylene glycol solutions on Au working electrode. It was found that chloride ions affect Te reduction but have no effect on Bi reduction. From chloride-free ethylene glycol electrolyte, the composition of the films is less dependent of the applied potential but can be controlled by concentration of precursors in the bath, unlike chloride-containing ethylene glycol solution. Also, the films obtained from chloride-free ethylene glycol exhibited smoother

surface than the films deposited from chloride-containing ethylene glycol. Both n- and p-type Bi_2Te_3 films were prepared, with the highest Seebeck coefficient of -120 μV/K for n-type. Szymczak *et al.*[23] reported Bi_2Te_3 electrodeposition from an ionic liquid binary mixture:1-ethyl-1-octyl-piperidinium bis(trifluoromethylsulfonyl)imide: 1-ethyl-1-octyl-piperidinium bromide (EOPipTFSI:EOPipBr 95:5 (mol%)) on Pt. The deposits have morphology of needle-like spherical aggregates and close stoichiometric composition with [1 1 0] highest intensity diffraction peak. The Seebeck coefficient is -70 μV/K, while the electrical resistivity is higher than of the films grown in aqueous solutions (133 $\mu\Omega$m). The carrier concentration corresponds to the previously reported values (1.21×10^{20} cm^{-3}).

The microstructural properties of Bi_2Te_3, such as crystalline orientation, crystallite size and composition, affect the thermoelectric performance of the material. The deposits with (1 1 0) preferential crystalline orientation, stoichiometric Bi_2Te_3 composition and optimised crystallite size possess the best thermoelectric performance [77]. In order to improve the thermoelectric properties, the effects of additives on the microstructure of Bi_2Te_3 was reported. Naylor *et al.*[77] studied the effect of sodium lignosulfonate (SL) surfactant added to HNO_3 acidic aqueous bath on Bi_2Te_3 films electrodeposited potentiostatically on Au. It was found that stoichiometric films can be obtained with and without addition of SL, but the addition of SL yields more compact films and improves the preferred crystallographic [1 1 0] orientation. The thermoelectric performance of the films were either improved or similar to those reported with the highest value of Seebeck coefficient of -15 μV/K for film deposited with 20 mg dm^{-3} SL concentration, resistivity of 3×10^{-4} Ω cm and carrier concentration of 2.5×10^{20} cm^{-3} for film electrodeposited with 60 mg dm^{-3} SL concentration. Caballero-Calero *et al.* [78] also reported potentiostatically grown Bi_2Te_3 films from HNO_3 acidic aqueous bath with addition of SL on Au working electrode. The [1 1 0] crystallographic orientation of the deposits and the morphology was improved in the presence of SL, with the Seebeck coefficient of -80 μV/K at 105 °C which is by 33% higher that the value obtained for films grown without addition of SL (-60 μV/K). The resistivity measured at 105 °C is 3.5×10^{-3} cm. Song *et al.*[79] investigated potentiostatic electrodeposition of Bi_2Te_3 thin films from HNO_3 acidic aqueous electrolyte with addition of cetyltrimethylammonium bromide (CTAB) on Au. The films deposited in the presence of CTAB showed improved surface morphology and mechanical properties, while the thermoelectric performance was unchanged. Also, the post-deposition annealing did not improve the thermoelectric properties of the films. The Seebeck coefficient of the films obtained by electrodeposition with addition of CTAB is around -85 μV/K and the resistivity is around 1×10^{-2} Ω cm. In addition, the carrier concentration decreased and the mobility increased in the films deposited with addition of CTAB. Kulsi *et al.* [80] reported effect of adding sodium dodecyl sulfate (SDS) and polyvinylpyrrolidone (PVP) to nitric aqueous bath on potentiostatically electrodeposited Bi_2Te_3 on ITO. Comparing the two surfactants,

the films electrodeposited in the presence of SDS exhibited better thermoelectric perfomance which is attributed to improved surface morphology forming better-structured nanoparticles. The authors reported the best ZT value of 0.28 for a film forming 55 nm nanospheres exhibiting Seebeck coefficient of -29 μV/K and the electrical conductivity of 4033 S cm^{-1}. In addition, the effect of the film thickness on the thermoelectric performance was investigated. By decreasing the film thickness the electrical conductivity increases significantly and the Seebeck coefficient decreases, which has overall little effect on the figure of merit (ZT). Liu *et al.* [81] investigated galvanostatic electrodeposition of Bi_2Te_3 from nitric acid bath with added ethylene glycol (EG) on Ti. EG lowers the surface tension and increases the solution viscosity influencing the movement of ions and atoms. This affects largely the surface morphology and the composition of the films. It was found that in the presence of EG, the deposits are denser than without EG and relatively smooth. The Seebeck coefficient of the films deposited with ethylene glycol is -46 to -50 μV/K, improvement compared to films deposted without EG (-28 to -30 μV/K).

One of the methods for ZT improvement of a thermoelectric material is incorporation of nanoparticles which would scatter phonons and decrease the lattice thermal conductivity. Wu *et al.* [82] incorporated 16 nm diameter silica nanoparticles into Bi_2Te_3 films electrodeposited from ethylene glycol solution. The presence of silica nanoparticles in the solution barely affected the deposition behaviour of Bi_2Te_3 films and silica nanoparticles were incorporated as individual particles rather than agglomerates, which is due to the low van der Waals forces between silica nanoparticles in ethlylene glycol solution. However, the incorporation of uniformly dispersed silica nanoparticles did not decrese the thermal conductivity of the films compared to films without silica nanoparticles. The measured Seebeck coefficient of the film containing silica nanoparticles almost identical to the Seebeck coefficient of the particle-free Bi_2Te_3 film (79 μV/K). Therefore, the incorporation of nanoparticles did not improve the thermoelectric performance of Bi_2Te_3 film, as it is commonly believed.

To summarise, electrodeposition of Bi_2Te_3 thin films has mainly been investigated in aqueous solvents such as nitric, sulfuric and hydrochloric acid solution. Different electrodeposition methods have been employed, including potentiostatic, galvanostatic and pulsed deposition. Generally, pulsed deposition yields films with improved morphology and thermoelectric properties compared to those grown under constant potential or current. In addition, improvements of films' properties grown potentiostatically were achieved by addition of surfactants into electrolyte solution. Bi_2Te_3 thin film electrodeposition has also been studied in non-aqueous solvents, as these solvents have a wider electrochemical window allowing investigation of higher overpotentials on Bi_2Te_3 deposition. Also, Bi(III) and Te(IV) salts can be dissolved better in non-aqueous than acidic

aqueous solutions providing improved deposition rates. The electrodeposition from non-aqueous solvents including dimethylsulfoxide, ethyleneglycol, chloride-free ethylene glycol, and 1-ethyl-1-octyl-piperidinium bis(trifluoromethylsulfonyl)imide: 1-ethyl-1-octyl-piperidinium bromide has been reported. There is a range of measured Seebeck coefficients and resistivities reported in literature. For as-deposited Bi_2Te_3 thin films without annealing the reported values are mainly around -50 μV/K for Seebeck coefficient, about 1.5 mΩcm resistivity with carrier concentration in the range of 10^{20} cm^{-3} at room temperature. In order to carry out resistivity measurements on as-deposited films, the film transfer onto an insulating substrate using epoxy resin has been reported. It is generally accepted within the thermoelectric community that the inclusion of nanoparticles into the material improves ZT as nanoparticles scatter phonons, decreasing the lattice thermal conductivity. However, the experimentally reported electrodeposited Bi_2Te_3 thin film with incorporated silica nanoparticles did not show an improvement of thermoelectric properties compared to the particle-free film.

3.9 Electrodeposited antimony telluride thin films

As in the case of bismuth telluride, antimony telluride thin film electrodeposition has mainly been investigated in acidic aqueous solvents. However, not many reports exist in literature on Sb_2Te_3 electrodeposition possibly due to poor solubility of Sb precursor in aqueous solutions. In most cases this consequently leads to amorphous films and a need of post-annealing treatment in order to obtain good thermoelectric performance [32]. Leimkühler *et al.* [83] investigated potentiostatic electrodeposition from hydrochloric acidic aqueous bath on ITO, FTO and Mo working electrode. Polycrystalline Sb_2Te_3 films are obtained by deposition at 372 K, while those grown at room temperature are amorphous. Del Frari *et al.* [26] studied potentiostatic electrodeposition of Sb_2Te_3 films from tartaric and perchloric aqueous acidic bath on stainless steel. The films electrodeposited at room temperature are amorphous but crystallise after post-annealing at 100 °C. Tittes *et al.* [84] electrodeposited Sb_2Te_3 films potentiostatically from diphosphate alkaline aqueous solution with stirring on Cu and Ni foils. The obtained Sb_2Te_3 film is p-type with carrier comcentration of 2.1×10^{17} - 2.7×10^{17} cm^{-3}. Huang *et al.* [27] electrodeposited Sb_2Te_3 films galvanostatically from tartaric-nitric aqueous bath on TiN working electrode. Here as well, room temperature electrodeposition yields amorphous films. The amorphous to crystalline phase transition was observed at 120 °C, while electroplating at high temperature (100 °C) polycrystalline films are obtained without post-annealing. Lim *et al.* [28] electrodeposited potentiostatically Sb_2Te_3 films from tartaric-nitric aqueous bath on Ti working electrode and performed thermoelectric characterisation on amorphous films. The Seebeck coefficient of amorphous electrodeposited films larger than 250 μV/K is in this case higher than in crystalline films grown by other methods, and is ascribed to noncrystallinity of the films. The films electrodeposited at 10 mV vs. Ag/AgCl exhibit high carrier density of $\approx10^{21}$ with the highest power factor of 57×10^{-4} W/K^2 m. Jung *et al.* [85] studied potentiostatic electrodeposition of Sb_2Te_3 films from tartaric-nitric aqueous solution on Au working electrode under influence of agitation. It was found that agitation does not influence the composition but influences morphology and crystallinity of the films. Amorphous films were electrodeposited in the absence of agitation, while films with improved crystallinity were obtained by controlling the agitation rate at room temperature. Lim *et al.* [29] electrodeposited Sb_xTe_y films potentiostatically in aqueous nitric acid on Au working electrode. Films with stoichiometric composition were prepared by applying potential of -0.15 V vs. SCE. At higher potentials insulating films with rough morphologies were obtained. Polycrystalline films were electrodeposited at room temperature with stirring at 300 rpm. Thermoelectric measurements of the stoichiometric films showed that is p-type with hole concentration of 5.8×10^{18} cm^{-3} and mobility of 54.8 cm^2/ V s. The Seebeck coefficient of as-deposited stoichiometric films is 118 μV/K. Lensch-Falk *et al.* [86] examined deposition from tartaric-nitric solution on Au working electrode at room temperature by

pulsed electrodeposition. The films obtained by pulsed electrodeposition exibited improved composition, homogeneity and crystallinity compared to films obtained potentiostatically. Here, polycrystalline films were deposited at room temperature by pulsed electrodeposition without post-annealing. Ma *et al.* [30] reported electrodeposition of Sb_2Te_3 films from nitric aqueous solution on Au working electrode by both constant and pulsed deposition at room temperature without stirring. The obtained as-deposited films were amorphous which crystallise after annealing (phase transition at 130 °C), and Te phase separates. Morphological changes were observed on films with increasing deposition potentials. Rougher films were obtained by increasing deposition potentials even for pulsed deposition which was attributed to severe ion depletion at the electrode surface with increasing potentials. Thermoelectric measurements on the annealed film electrodeposited by pulsed deposition (t_{on}=1 s, t_{off}=10 s) at -0.3 V vs. Ag/AgCl showed the film is p-type with carrier concentration of 9×10^{19} cm^{-3}. Measured resistivity, Seebeck coefficient and power factor were 37.99 $\mu\Omega$ m, 148.2 μV/K and 578.13 $\mu W/mK^2$, respectively. Amorphous films were found to be too resistive to be useful for thermoelectric purposes. Nguyen *et al.* [35] reported electrodeposition from molten mixtures of acetamide at 100°C on Au working electrode, with measured Seebeck coefficient of +80 μV/K. Kim *et al.* [31] reported enhanced thermoelectric properties by preparing γ-SbTe/Sb_2Te_3 nanocomposite films. The films were electrodeposited potentiostatically at room temperature from nitric aqueous solution on Au electrode. After annealing, the as-deposited amorphous films were crystallized. The enhancement of thermoelectric properties was observed in films annealed between 70-100 °C where intermediate γ-SbTe phase appeared. The highest thermoelectric values of conductivity, Seebeck coefficient and power factor of 56.7 S/cm, 322 μV/K and 600 $\mu W/mK^2$, respectively, were measured on film annealed at 80 °C. The proposed explanation of this thermoelectric properties increment is that the two-phase system provides the carrier energy filtering at the interfaces between the phases. Catrangiu *et al.* [36] studied potentiostatic electrodeposition of Sb_2Te_3 films from ionic liquid consisting in mixture of choline chloride with oxalic acid on Cu and stainless steel at 60-70 °C. XRD pattern showed that the Sb_xTe_y electrodeposited from ChCl-OxA ionic liquid at room temperature are amorphous, while those deposited at 60 °C are crystalline. The stoichiometry of the films depends more on the bath composition than on the applied potential. Sides *et al.* [33] investigated nucleation and growth of Sb_2Te_3 films on Au substrates electrodeposited from nitric and acidic aqueous solution. It was found that both Sb and Te follow 3D nucleation growth despite of underpotential deposition. The deposition of Sb corresponds to progressive while Te follows instantaneous nucleation model. Sb_2Te_3 compound nucleation model is more influenced by Te than Sb. Su *et al.* [32] reported thermoelectric characterisation of Sb_2Te_3 films electrodeposited potentiostatically from nitric and tartaric aqueous solution at room temperature on Ti working electrode. The film electrodeposited at -0.3 V vs. SCE is polycrystalline with dense morphology. The film was transferred with epoxy resin to conduct thermoelectric measurements. The Seebeck coefficient decreases

over temperature range from 310-417 K, peaking at 56 μV/K at 310 K. The electrical conductivity increases over the given temperature range, peaking at 7.9×10^{-6} Ω m at 417 K. The corresponding power factor reaches maximum value of 595.9 μW/mK^2 at 310 K. The effect of thermal annealing on thermoelectric properties of electrodeposited Sb_2Te_3 films was also reported in [34]. The films were electrodeposited from hydrochloric aqueous solution on stainless steel and the effect of annealing was investigated over temperature range 200-400 °C. It was observed that as-deposited films are amorphous, while by annealing over temperature range from 200-350 °C the Sb_2Te_3 crystallises and the structure remains unchanged regardless of annealing temperature. After annealing at 400 °C the crystal structure changes drastically. The XRD pattern shows the Sb_2Te_3 peaks are no longer visible, but those coming from chemical compounds after elements from the substrate diffused in the film. Upon annealing up to 350 °C the grain size increases and the morphology of the films stays granular and continuous. When annealed at 400 °C the surface morphology becomes porous with irregularly shaped grains. The stoichiometry of the films remains the same up to 250 °C when impurities from the substrates can be seen. The film annealed at 200 °C possesses the highest Seebeck coefficient of ≈170 μV/K at room temperature. Electrical conductivity of 1034 S/cm is the highest for the film annealed at 300 °C. The power factor maximises at 13.6 μW/cm K^2 for the film annealed at 300 °C. This enhanced thermoelectric properties of the film annealed at 300 °C are attributed to impurities diffusing from the substrate into the film after annealing.

To summarise, Sb_2Te_3 thin film electrodeposition has mainly been studied in aqueous solutions, including hydrochloric and nitric acidic solutions. As in the case with Bi_2Te_3 electrodeposition, potentiostatic, galvanostatic and pulsed deposition were reported. Pulsed conditions achieve more uniform and dense films compared to those electrodeposited under continuous electrodeposition. It has mainly been reported that room temperature deposition without stirring yields amorphous films which crystallize after post-annealing at around 100 °C. The electrodeposition from non-aqueous solutions was reported in molten mixture of acetamide-antimony chloride and tellurium chloride, and ionic liquid consisting in mixture of choline chloride with oxalic acid. The reported thermoelectric measurements vary greatly. The reported Seebeck coefficients vary from 50 to 320 μV/K, the resistivity from 0.5-18 mΩcm with carrier concentration in the range 10^{17}-10^{19} for a polycrystalline film at room temperature.

Chapter 4

Fabrication and Characterisation

4.1 Fabrication of templates for electrodeposition

The fabrication process of templates for electrodeposition of Bi_2Te_3 and Sb_2Te_3 thin films from dichloromethane is shown in Fig. 4.1, and is based on the following steps:

1. **Sputtering of the bottom SiO_2 layer.** In order to isolate working electrode from Si substrate, 500 nm thick layer of SiO_2 insulating layer was obtained by Medium frequency plasma assisted magnetron sputtering using Leybold Helios Pro XL Sputterer DV05 (Fig. 4.1a). Sputtering is a process of ejecting atoms from a solid target material after it is being bombarded by energetic ions generated in plasma. Si target is sputtered under oxygen plasma and the substrates are rotated in a circle during the process passing below the sputtered source and the plasma source [87]. The deposition rate for SiO_2 is 0.51 nm/s. To sputter 500 nm time of the deposition was set to 981 s.

2. **Sputtering of TiN.** Using the Helios system, 200 nm thick layer of titanium nitride (TiN) which serves as working electrode was sputtered on top of SiO_2 layer (Fig. 4.1b). Ti target is sputtered under nitrogen plasma. The deposition rate for TiN is 0.15 nm/s. To sputter 200 nm the deposition time was set to 1334 s.

3. **Spinning, exposure and development of photoresist.** After the sputtering of the TiN layer, a photolithography step is needed to pattern the contact area and working electrode which will allow electrodeposition. Negative photoresist AZ2070 was spin-coated on the TiN, exposed to the UV light through the mask and developed in MF 726, which is illustrated by Fig. 4.1c,d,e.

4. **Sputtering of the top SiO_2 layer.** 200 nm thick SiO_2 layer was sputtered for 393 s on top of TiN layer using the Helios system (Fig. 4.1c).

5. **Lift-off.** The areas of SiO_2 on top of photoresist are lifted in *N*-Methyl-2-pyrrolidone (NMP) (Fig. 4.1g).

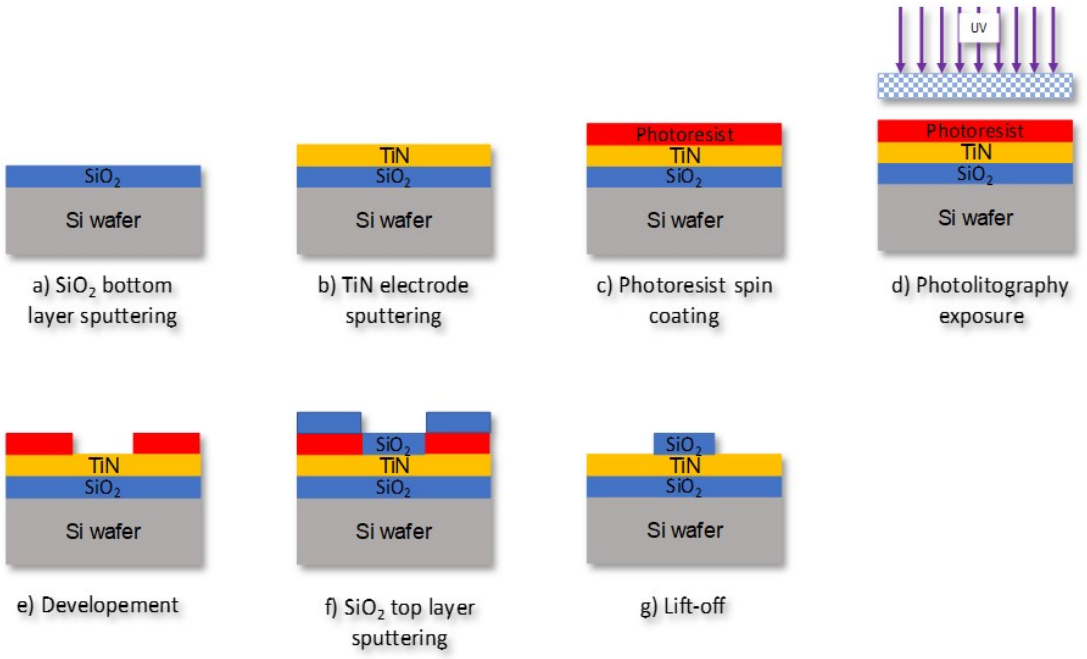

FIGURE 4.1: The schematics of fabrication process of working electrodes for electrodeposition.

Once the process was completed, the wafer was cleaned to remove the photoresist residuals and diced into 25x10 mm substrates, as shown in 4.2b. Fig. 4.2c shows x-section SEM image of Si wafer onto which SiO_2 and TiN layers are sputtered as explained above. The film was electrodeposited onto TiN layer which serves as working electrode. X-section SEM image reveals the actual thicknesses of SiO_2 and TiN of 479 nm and 169 nm, respecively. This fabrication process has been established previously and is described in [88].

4.2 Electrodeposition - materials and methods

Electrolytes were prepared in anhydrous CH_2Cl_2 (Sigma Aldrich, 95%), dried and degassed by refluxing with CaH_2 (followed by distillation and then stored in glovebox, the water content in dried CH_2Cl_2 was *ca.* 18 ppm), with addition of 0.1 M $[N^nBu_4]Cl$ (Sigma Aldrich, $\geq$ 99.0% as-received) as the supporting electrolyte. As Bi, Sb and Te precursors $[N^nBu_4][BiCl_4]$, $[N^nBu_4][SbCl_4]$ and $[N^nBu_4]_2[TeCl_6]$ were synthesized as described [89] (see Appendix 1).

Cyclic voltammetry and electrochemical depositions were carried out in a three-electrode system using an Autolab potentiostat (μAUT70706) in a recirculating glovebox (Belle

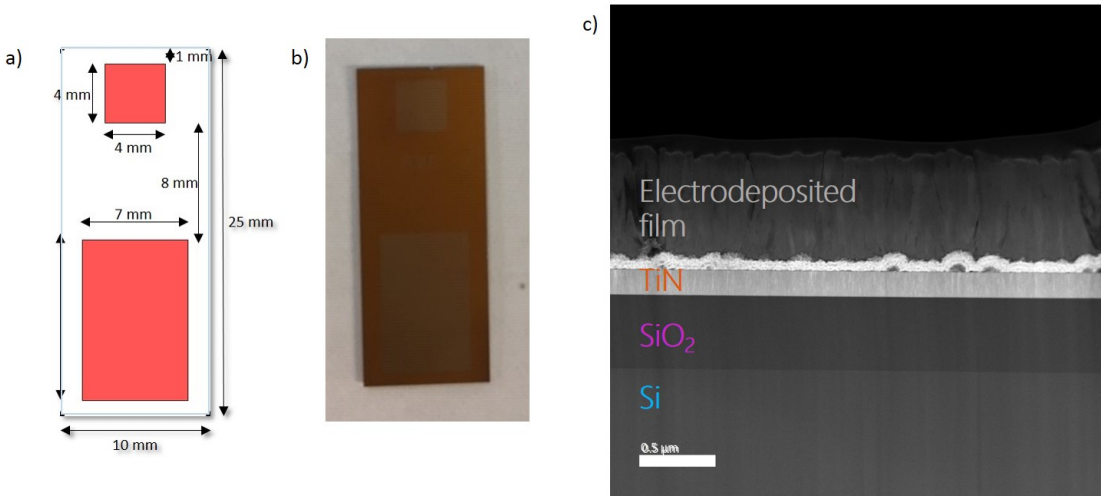

FIGURE 4.2: a) Design of the substrate for electrodeposition of Bi_2Te_3 where the upper square serves as a connection area to connect working and counter electrode, and the rectangle serves as working electrode, b) Photograph of the lithographically fabricated substrate, c) Cross section SEM image of the working electrode area on which the film was electrodeposited.

Technology, UK). A 1 cm diameter Pt disc was used as a counter electrode. An Ag/AgCl electrode (0.1 $[N^nBu_4]Cl$ in anhydrous CH_2Cl_2) was employed as a reference electrode. As a working electrode, either 3 mm diameter glass sealed glassy carbon (GC, Sigradur G, HTW, Germany) electrode or 7x11 mm titanium nitride (TiN) was used. The glass sealed GC electrode was used to characterise the precursors and was polished prior use with alumina powder (1 μm and 0.05 μm diameter in sequence, micropolish, Buehler, Germany) on a water saturated polishing pad (Microcloth, Buehler). The TiN working electrodes were fabricated as described in 4.1.

Scanning electron microscopy (SEM) was performed using a Zeiss EVO LS 25 with an accelerating voltage of 10 kV, and energy-dispersive X-ray (EDX) data were obtained with an Oxford INCAx-act X-ray detector. EDX calibration was carried out using a standard Bi_2Te_3 and Sb_2Te_3 powder (Strem Chemicals, 99.99%). High resolution SEM measurements were carried out with a field emission SEM (Jeol JSM 7500F) at an accelerating voltage of 2 kV. X-ray diffraction (XRD) measurements were carried out using a Rigaku Smartlab diffractometer either in symmetric or grazing incidence mode (θ_1= 1°) with a 9 kW Cu-K_α (λ = 1.5418 Å) source, parallel line focus incident beam and a Hypix detector. Phase matching and lattice parameter refinement were carried out using the PDXL2 software package and diffraction patterns from the Inorganic Crystal Structure Database (ICSD) [42]. X-ray photoelectron spectroscopy (XPS) data were obtained using a ThermoScientific Theta Probe System with Al–K radiation (photon energy= 1486.6 eV). XPS depth profile was performed by using an Ar ion gun at a beam voltage of 3 kV on a 2×2 mm raster area. The in-plane electrical conductivity (σ) and Seebeck coefficient (S) were simultaneously measured on a commercial JouleYacht Thin-film Thermoelectric Parameter Test System (MRS-3L). The system was calibrated using

Nickel foil reference standard and the measurement accuracy was found to be within 5% for resistivity and 7% for Seebeck coefficient measurements. The Hall coefficient (R_H) was determined at 300 K on a Nanometrics HL5500PC instrument using a van de Pauw configuration. The carrier concentration (n) and in-plane mobility (μ) were computed according to 1/n=eR and μ=σR, respectively.

4.3 Characterisation techniques

4.3.1 Scanning electron microscopy

Scanning electron microscopy (SEM) is employed for observation of sample surfaces. The sample is irradiated by a fine electron beam, after which secondary electrons are emitted from the sample surface. The microscope is made of an electron optical system to produce electron beam, a sample stage for the placement of the sample(s), a secondary-electron detector which collects secondary electrons, an image display unit, and an operation system for performing various operations. The surface is observed by two-dimensional scanning of electron beam over the surface, and the image is acquired from secondary electrons. When the electrons enter the sample, they are scattered within the sample gradually losing their energy and eventually being absorbed. The scattering range of the electrons inside the sample will differ depending on the energy of electrons, the atomic number of elements in the sample and the density of the sample. The higher the electron energy, the larger will the scattering range be. On the other hand, the larger the atomic number of elements and density, the smaller will the scattering be. Figure 4.3 illustrates the various signals emitted from the sample after illumination with the electron beam. The SEM uses these signals for imaging of the sample surface.

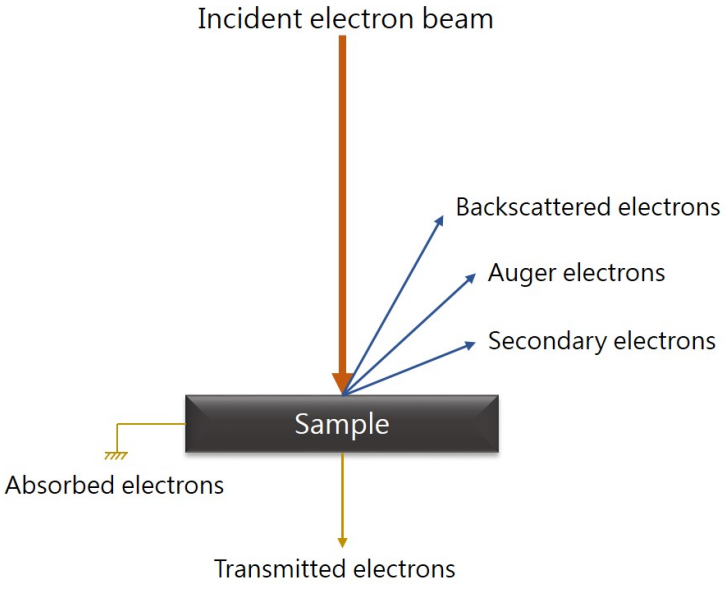

FIGURE 4.3: Schematics illustrating signals emitted from the sample after illuminated by an electron beam.

- *The secondary electrons* are emitted by valence electrons atoms in the sample, and they possess very low energy. Those generated in the deeper regions of the sample are absorbed within the sample due to their low energies, while those coming from the surface are emitted out of the sample. Hence, the secondary electrons

are sensitive to the surface, and they are used to observe the morphology of the sample surface.

- *The backscattered electrons* are electrons scattered backward and emitted out of the sample after the incident electron beam is scattered in the sample. These electrons possess higher energies than the secondary electrons, containing information about deeper regions in the sample. The higher the atomic number of elements in the sample, the higher the emission of backscattered electrons. Imaging from backscattered electrons can be useful for observation of compositional difference.

- *The Auger electrons* are electrons possessing higher energies than backscattered electrons. The Auger effect is a radionless transition in an atom. One of the inner levels of an atom is ionised, causing the ejection of electron known as an Auger electron.

The penetration depth of incident electrons from electron beam depends of an accelerating voltage. The higher the accelerating voltage, the larger the penetration depth will be. By increasing the accelerating voltage the information from inside the sample is obtained degrading the contrast on the sample surface. In order to observe clearly the sample surface, lower accelerating voltages (1-3 kV) are better [90]. Figure 4.4 shows SEM image of Bi_2Te_3 electrodeposited from dichloromethane, taken at the accelerating voltage of 2 kV.

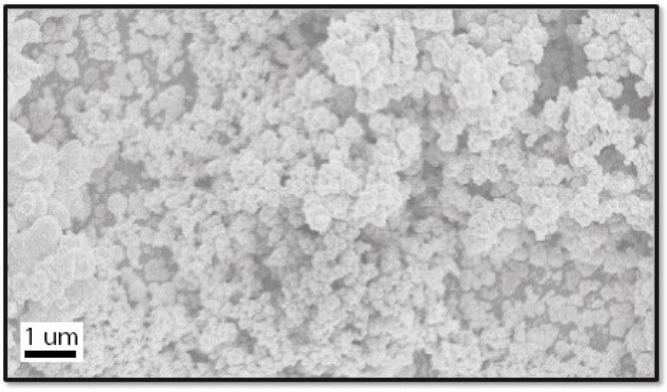

FIGURE 4.4: SEM image of Bi_2Te_3 electrodeposited potentiostatically at -1 V vs. Ag/AgCl on TiN form 2.5 mM $[N^nBu_4][BiCl_4]$, 3 mM $[N^nBu_4]_2[TeCl_6]$ and 0.1 M $[N^nBu_4]Cl$ in CH_2Cl_2. The accelerating voltage is 2 kV.

4.3.2 Energy dispersive X-ray spectroscopy

Energy dispersive X-ray spectroscopy (EDX) is used for elemental analysis of the sample by measuring the X-rays emitted from the sample. As mentioned above, various electrons and electromagnetic waves are emitted from the sample after illumination with an electron beam. Figure 4.5 shows the schematic of characteristic X-ray generation.

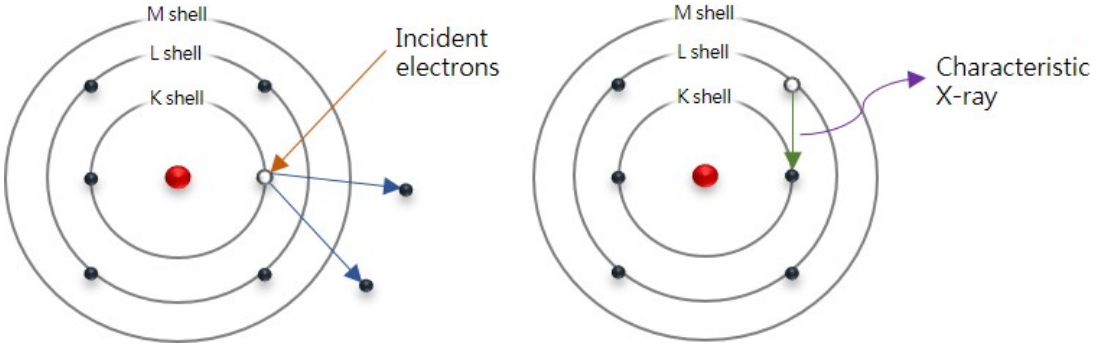

FIGURE 4.5: Schematic of X-ray generation.

When the electrons from the inner shells are kicked out from an atom in the substrate by an incident electron beam, their vacant orbitals are filled by outer-shell electrons and X-ray is emitted. The energy of emitted X-rays equals the energy difference between the outer-shell and inner-shell electrons. These energies (wavelengths) are characteristic for each element, and are called characteristic X-rays. The characteristic X-rays are used for elemental analysis of the sample. The characteristic X-rays emitted from electrons in K shells are called 'K-lines', the ones emitted by electrons in L shells are 'L-lines', and so forth. The heavier the element in the sample, the higher the energy of a characteristic X-ray. Therefore, the higher energy electron beam is needed to emit a characteristic X-ray from a heavier atom. If the incident electrons are decelerated by the nucleus, the so-called continuous X-rays will be emitted with wider distributions of energies (wavelengths) [90]. Figure 4.6 shows an EDX spectrum of Bi_2Te_3 thin film electrodeposited from dichloromethane. The x-axis corresponds to energy of X-ray for each constituent element, and the y-axis to X-ray counts.

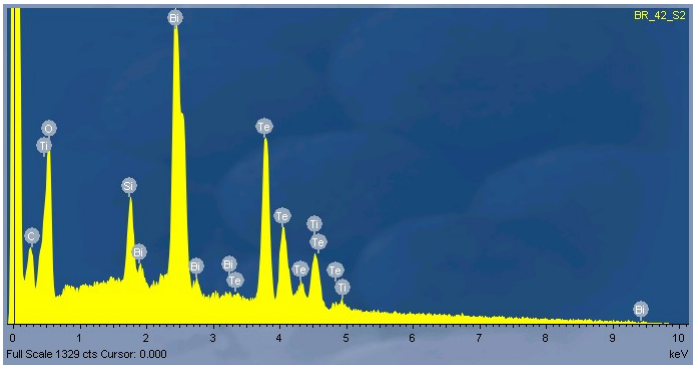

FIGURE 4.6: EDX spectrum of Bi_2Te_3 thin film electrodeposited on TiN at -1 V vs. Ag/AgCl form 2.25 mM $[N^nBu_4][BiCl_4]$, 3 mM $[N^nBu_4]_2[TeCl_6]$ and 0.1 M $[N^nBu_4]Cl$ in CH_2Cl_2.

4.3.3 X-ray diffraction

X-ray diffraction (XRD) is an analysis technique for characterising crystalline materials. X-rays are relatively short wavelength (high-energy) electromagnetic radiation. X-ray

diffraction requires X-rays wavelengths of the order of interatomic spacing to produce interference (0.07-0.2 nm). The most commonly used radiation is from CuK_α source with wavelength λ=0.15406 nm. Interference of the waves scattered from planes within the crystal can be constructive and destructive. Figure 4.7 shows a schematic of two incident beams with identical wavelengths scattering from two different atoms within a crystalline material.

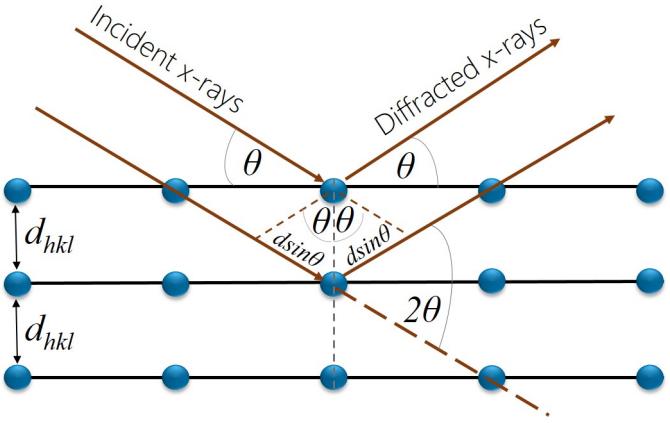

FIGURE 4.7: Schematic principle of X-ray diffraction.

The constructive interference of the scattered waves produces diffraction peaks, and is defined by the Bragg's law:

$$2dsin\theta = n\lambda \tag{4.1}$$

where d is interplanar distance between planes in the crystal, θ is grazing angle, and n is a positive integer. The law states that if the beam below (Fig. 4.7) passes an extra distance of $2dsin\theta$ the constructive interference occurs.

Figure 4.8 shows diffraction pattern of Sb_2Te_3 thin film electrodeposited on TiN from dichloromethane. The pattern consists of diffraction peaks as a function of diffraction angle (2θ), with peaks corresponding to crystallographic planes. Applications of x-ray diffraction analysis method are:

- Qualitative identification of the crystal phases in a sample. The recorded diffraction pattern can be compared to the known powder pattern from a database, and identified in this way.
- Quantitative analysis of each crystal phase in a multiphase sample.
- The size and shape of the unit cell in a crystalline material.
- Orientation of crystallites in a polycristalline material.
- The strain present in crystallites.

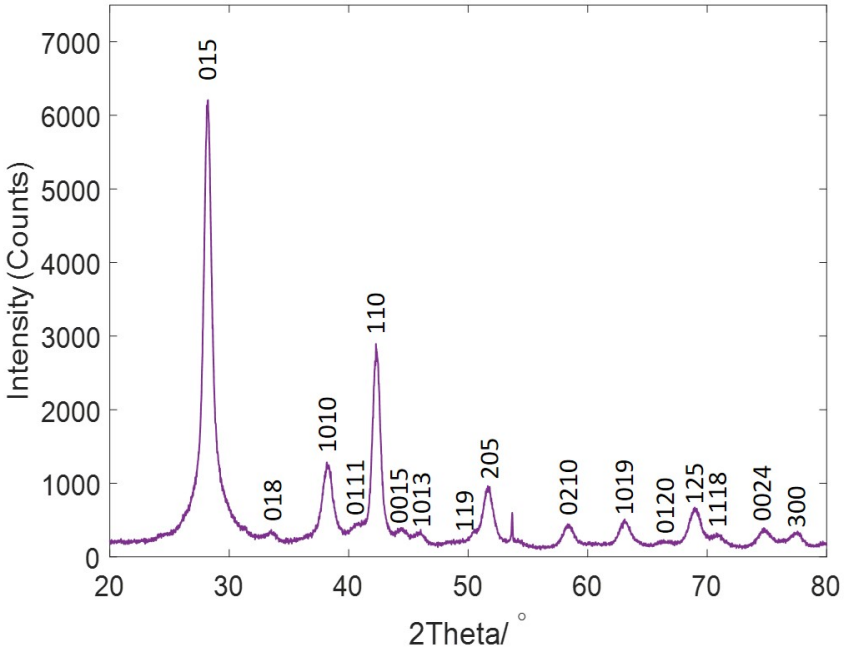

FIGURE 4.8: X-ray diffraction pattern of Sb_2Te_3 thin film electrodeposited on TiN at -0.8 V vs. Ag/AgCl (t_{on}=5 s/t_{off}=10 s) form 1.75 mM $[N^nBu_4][SbCl_4]$, 3 mM $[N^nBu_4]_2[TeCl_6]$ and 0.1 M $[N^nBu_4]Cl$ in CH_2Cl_2, after annealing at 100°C for 30 minutes.

- Microstructural properties of a polycrystalline material (crystallite size, microstrain within the crystallite, defect densities) [91].

4.3.4 X-ray photoelectron spectroscopy

X-ray photoelectron spectroscopy (XPS) is a surface-sensitive analytical method for determination of the kinetic energy of photoelectrons ejected from a sample after irradiation by X-rays in high vacuum (usually higher than 10^{-7} Pa). The binding energy (E_B) of the emitted electron can be determined by the Eq. 4.2.

$$E_{\mathrm{B}} = h\nu - (E_{\mathrm{K}} + \phi) \tag{4.2}$$

where hν is energy of incident X-ray, E_K is the measured kinetic energy of ejected electron, and ϕ is the work function of the material. The E_B value is characteristic for each element and is used to identify the chemical bonding state of an element in the sample. If an acquired spectrum is expected to contain several components, the peak separation computer-aided technique can be used to obtain individual bonding states of an element. Figure 4.9a shows Bi scan in Bi_2Te_3 thin film electrodeposited from dichloromethane, and peak deconvolution corresponding to Bi chemically bonded

to either Te or O. The x-axis corresponds to binding energy E_B of Bi with Te and O, and the y-axis corresponds to counts of electrons which kinetic energy is being measured.

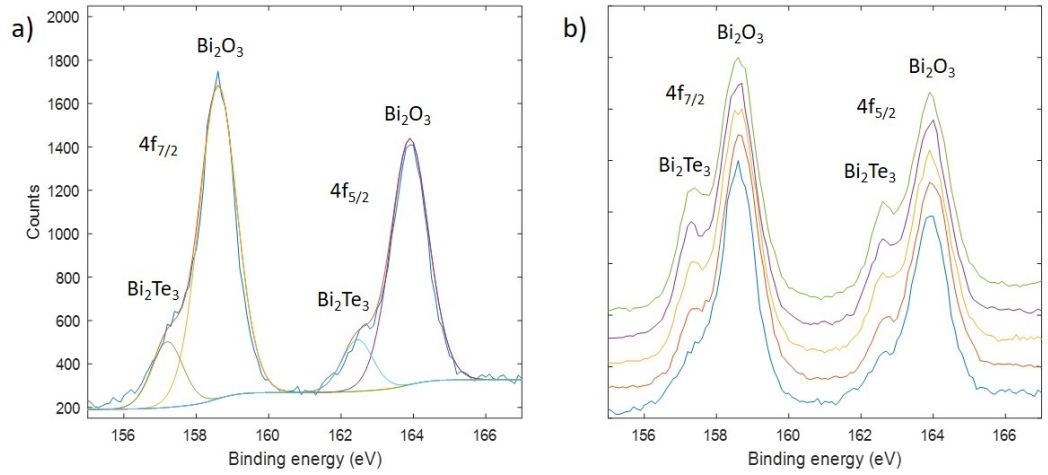

FIGURE 4.9: Bi scan in Bi_2Te_3 thin film electrodeposited on TiN at -0.6 V preceded by a nucleation pulse at -1 V vs. Ag/AgCl form 2.25 mM $[N^nBu_4][BiCl_4]$, 3 mM $[N^nBu_4]_2[TeCl_6]$ and 0.1 M $[N^nBu_4]Cl$ in CH_2Cl_2. a) first scan prior to etching with peak separation, and b) five scans after etching. Blue: surface prior to etching, orange: after 60 s of etching,yellow: after 120 s of etching, purple: after 180 s of etching, and green: after 240 s of etching.

Only electrons from approximately 0.3-4 nm (depending on E_K) depth in the sample can escape and reach the detector. Thus, the information is very shallow, and differs for different elements and electron orbitals [92]. The surface contamination of the sample can be removed by etching with Ar ions, or to deliberately expose the deeper layers to investigate bulk of the material. Figure 4.9b shows Bi scan Bi_2Te_3 thin film electrodeposited from dichloromethane after four cycles of etching exposing the deeper layers.

4.3.5 Hall effect measurements

Hall effect is the result of the Lorentz force on the free charge carriers in a solid. Lorentz force is the force exerted on a charged particle q moving with velocity v through an electric E and magnetic field B. The entire electromagnetic force F on the charged particle is called the Lorentz force. This is illustrated on Fig 4.10.

When a magnetic field perpendicular to the charge carrier flow is applied to the sample, the charge accumulates at the faces of the sample as their paths are being deflected. In a semiconductor, where both electrons and holes are presents, both charge carriers experience the Lorentz force and drift in the opposite directions. At the equilibrium, a voltage (V_H) appears at the edges. Hence, when both electrons and holes are present Hall effect includes concentrations and drift mobilities of both electrons and holes. The Hall coefficient (R_H) is given by the equations 4.3 and 4.4.

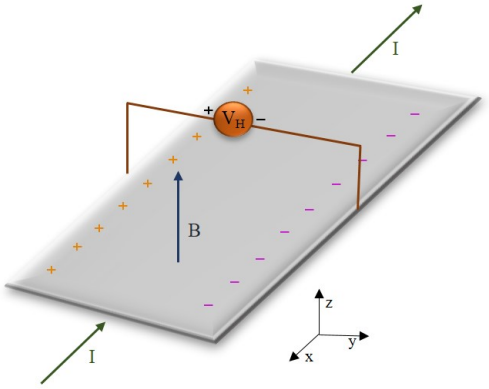

FIGURE 4.10: An illustration of the Hall effect on free charge carriers in a solid. The charge carriers are deflected by the Lorentz force and accumulated at the face of the sample.

$$R_{\mathrm{H}} = \frac{E_{\mathrm{y}}}{j_{\mathrm{x}} B_{\mathrm{z}}} \tag{4.3}$$

where E_y is the electric field in the direction of y-axis, j_x is the current flowing in the direction of x-axis and B_z is the magnetic field applied in the direction of z-axis.

$$R_{\mathrm{H}} = \frac{p{\mu_{\mathrm{h}}}^2 - n{\mu_{\mathrm{e}}}^2}{e(p\mu_{\mathrm{h}} + n\mu_{\mathrm{e}})^2} \tag{4.4}$$

where n is the electron concentration, μ_e is the electron mobility, p is the hole concentration, μ_h is the hole mobility, and e is the elementary charge. In order to measure the resistance (R), a current (I) is made to flow along the sample and the voltage (V) is measured at the opposite edges. The resistance can be calculated using the Ohm's law defined by the Eq. 4.5.

$$R = \frac{V}{I} \tag{4.5}$$

If the dimensions of the sample are known, resistivity (ρ) can be calculated by using Eq. 4.6.

$$\rho = R\frac{A}{d} \tag{4.6}$$

where A is the area and d is the thickness of the sample.

The commonly used technique for resistivity and Hall coefficient measurements is van der Pauw Method. In this method, four probes are placed on the perimeter of approximately two-dimensional sample. The resistivity is calculated from eight voltage measurements

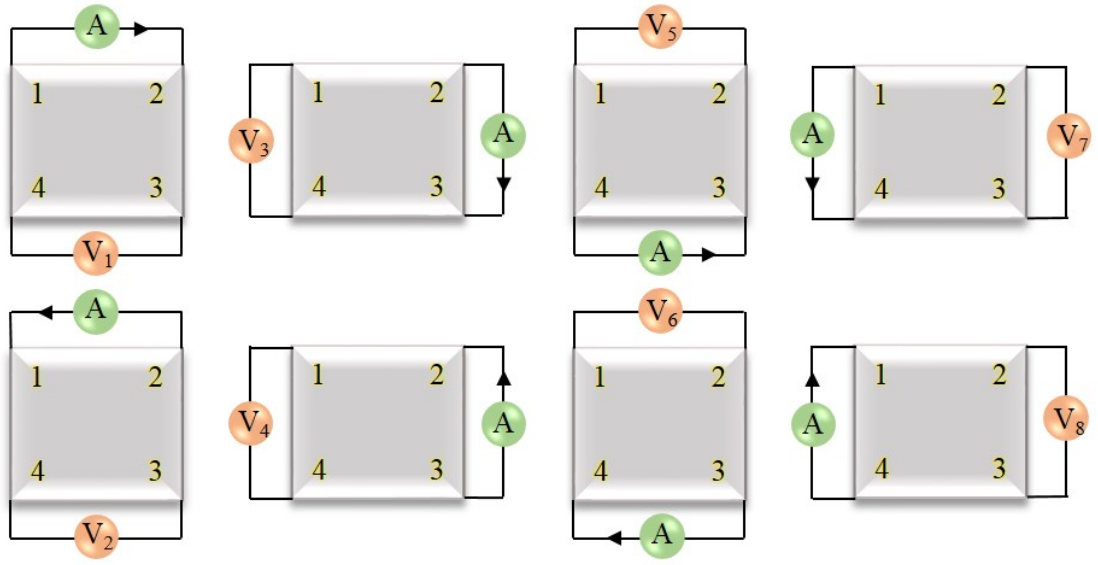

FIGURE 4.11: Van der Pauw voltage measurements configurations.

on the sample with configurations shown in Fig. 4.11. Two values of resistivity (ρ_A and ρ_B) are obtained defined bz the Eq. 4.7 and 4.8.

$$\rho_A = \frac{\pi}{ln2} f_A t_s \frac{(V_1 - V_2 + V_3 - V_4)}{4I} \tag{4.7}$$

$$\rho_B = \frac{\pi}{ln2} f_B t_s \frac{(V_5 - V_6 + V_7 - V_8)}{4I} \tag{4.8}$$

where ρ_A and ρ_B are volume resistivities, t_s is the sample thickness, V_1-V_8 are measure

ρ_A and ρ_B are known, the average resistivity can be calculated using the Eq. 4.9.

$$\rho_{AVG} = \frac{\rho_A + \rho_B}{2} \tag{4.9}$$

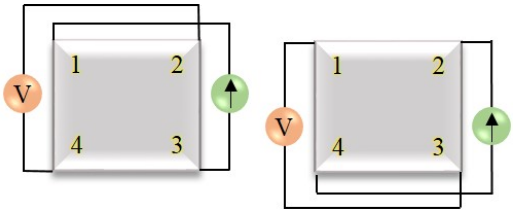

FIGURE 4.12: Hall voltage measurements configurations.

Hall effect measurements are carried out with an applied magnetic field (B), and the Hall voltage is measured using configurations shown in Fig. 4.12. Two values of Hall coefficients are obtained from eight Hall voltage measurements using the Eq. 4.10 and 4.11

$$R_{\mathrm{HC}} = \frac{t_{\mathrm{s}}(V_{\text{4-2+}} - V_{\text{2-4+}} + V_{\text{2-4-}} - V_{\text{4-2-}})}{4BI} \tag{4.10}$$

$$R_{\mathrm{HD}} = \frac{t_{\mathrm{s}}(V_{\text{3-1+}} - V_{\text{1-3+}} + V_{\text{1-3-}} - V_{\text{3-1-}})}{4BI} \tag{4.11}$$

With a positive magnetic field (B) and an applied current between points 1 and 3, the voltage drop between points 2 and 4 is measured ($V_{2\text{-}4+}$). By applying the reverse current the voltage drop $V_{4\text{-}2+}$ is measured. By applying current between points 2 and 4 the voltage drop between points 1 and 3 is measured ($V_{1\text{-}3+}$), with the reversed current $V_{3\text{-}1+}$ is measured. With the negative magnetic field the following four voltages are measured: $V_{2\text{-}4-}$, $V_{4\text{-}2-}$, $V_{1\text{-}3-}$ and $V_{3\text{-}1-}$. The average Hall coefficient can be calculated using the Eq. 4.12.

$$R_{\mathrm{AVG}} = \frac{R_{\mathrm{HC}} + R_{\mathrm{HD}}}{2} \tag{4.12}$$

The mobility can be calculated from the resistivity and the Hall coefficient using the Eq. 4.13 [93],[94],[95].

$$\mu_{\mathrm{H}} = \frac{\mid R_{\mathrm{AVG}} \mid}{\rho_{\mathrm{AVG}}} \tag{4.13}$$

4.3.6 Temperature dependent Seebeck coefficient and resistivity measurements

For simultaneous measurements of Seebeck coefficient and resistivity as function of temperature, sample is placed between four electrodes. One electrode contains a heater which heats the sample to set temperature. Two thermocouples contacting the sample measure the temperature gradient (ΔT=T_{hot}-T_{cold}), and the two thermocouples measures the thermalvoltage (V_{th}) that occurs due to the temperature gradient. Measurements are performed so that one side of the sample is heated up, and on the other side of the sample several values of temperature difference and Seebeck coefficients are being measured giving linear fitting and a gradient of dV/dT. The Seebeck coefficient is calculated from the obtained measurements using the Eq. 4.14.

$$S = \frac{-V_{\mathrm{th}}}{T_{\mathrm{hot}} - T_{\mathrm{cold}}} \tag{4.14}$$

Figure 4.13 shows raw Seebeck coefficient data. The voltage measurements were taken at one set temperature at equilibrium, and the Seebeck coefficient is calculated from linear fit. To measure the resistance, DC four-terminal technique is employed. Under thermal

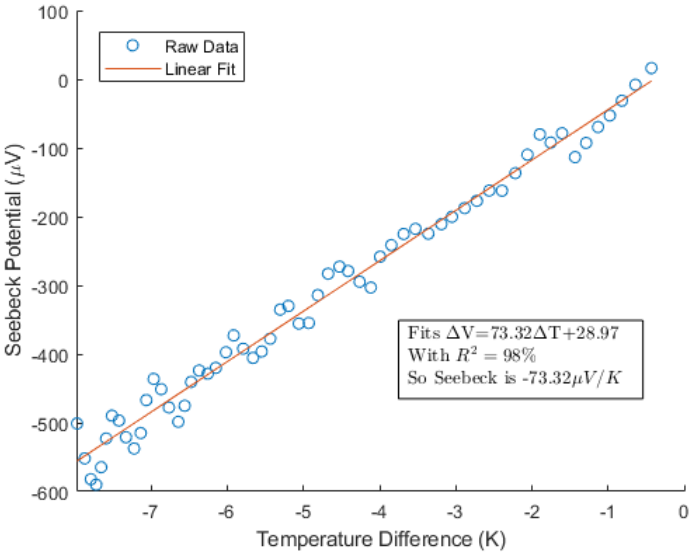

FIGURE 4.13: Raw Seebeck coefficient data showing voltage measurements (blue) at the set temperature at equilibrium and linear fit (orange) used for determination of Seebeck coefficient.

equilibrium (ΔT=0 K), a constant direct current (I) is forced through the sample by using two electrodes, and the resulting voltage drop (V) is measured utilising the two thermocouples. If the area (A) and the thickness (l) of the sample are known, the resistivity (ρ) can be calculated using the Eq. 4.15 [96].

$$\rho = \frac{V}{I} \times \frac{A}{l} \tag{4.15}$$

Figure 4.14 shows temperature dependent Seebeck coefficient and resistivity measurements taken on bismuth telluride film electrodeposited by pulse electrodeposition at -0.6 V vs. Ag/AgCl (t_{on}=5 s, t_{off}=10 s) preceded by a nucleation pulse at -1 V vs. Ag/AgCl for 5 s.

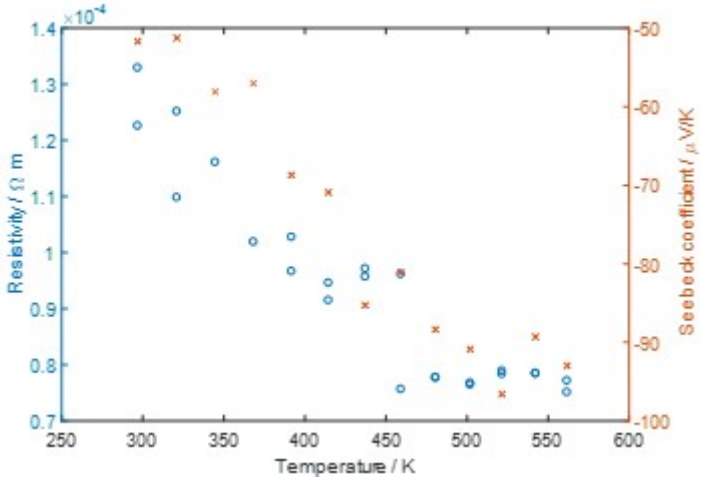

FIGURE 4.14: Temperature dependent Seebeck coefficient (orange) and resistivity (blue) measurements for the bismuth telluride film electrodeposited by pulse electrodeposition at -0.6 V vs. Ag/AgCl (t_{on}=5 s, t_{off}=10 s) preceded by a nucleation pulse at -1 V vs. Ag/AgCl for 5 s. Each measurement was taken twice for the given set temperature.

4.4 Thin film transfer process

4.4.1 Introduction

The thin film transfer process of electrodeposited materials is crucial in order to carry out electrical characterisation of films deposited on conductive surfaces. Techniques to transfer 2D materials have mostly been studied in the field of graphene. Currently, the most widely used technique for thin film transfer relies on using poly(methyl methacrylate) (PMMA) as a polymer supporting layer which allows effective transfer of 2D materials onto arbitrary substrates [97]. However, this technique requires the use of the substrate etchants in order to delaminate thin films from the substrates which contaminate the films. Also, removal of PMMA after the transfer is usually incomplete leaving the transferred films with polymer residues, as PMMA is difficult to remove after the transfer. In order to overcome these issues, modification of PMMA transfer method by adding water-soluble polyvinyl alcohol layer between PMMA and the film has been reported [98]. Alternative carrier polymers such as polystyrene (PS) [99], poly-trimethoxyphenylsilane [100], poly(lactic acid), poly(phthalaldehyde), poly(bisphenol A carbonate) [101], and Formvar (polyvinyl formal) [102] have also been investigated. In comparison to PMMA transfer technique, these alternative polymers allow more efficient removal after the transfer. Other transfer methods which do not involve a sacrificial polymer layer, such as by utilising thermal release tape (adhesive tape that adheres tightly at room temperature and can be peeled off by heating) [103], adhesive polyimide tape [104], use of an insulating epoxy adhesive to peel away the films [105] [106] [107], and growing the film on conductive poly(3,4-ethylenedioxythiophene):poly(styrene sulfonate) which can afterwards be dispersed in water [108], have also been reported.

Herein, attempts to transfer electrodeposited Bi_2Te_3 thin films from conductive TiN substrate onto insulating SiO_2 substrate the methods by using poly(methyl methacrylate) (PMMA) as a carrier polymer, thermal release tape and polystyrene (PS) as a carrier polymer were employed.

4.4.2 Experimental

The first method of the transfer of potentiostatically electrodeposited Bi_2Te_3 thin films at -1 V vs. Ag/AgCl from TiN substrates onto insulating substrate was carried out using PMMA as a carrier polymer. 4 % W/V PMMA/anisole solution was dropped on the films and baked at 100 °C for 2 minutes to dry the polymer. The substrates were left in AZ 400K (2% W/V KOH solution) to float for 90 minutes. PMMA layer with Bi_2Te_3 film was then peeled off from TiN substrates, rinsed with deionised water and transferred onto 50 nm thick SiO_2 layer on Si substrate. The 50 nm of insulating SiO_2 was grown on Si wafer by dry oxidation in a furnace for 60 min at 1000 °C. SiO_2 The

removal of the top PMMA layer was attempted by dipping the sample into acetone, N-Methyl-2-pyrrolidone (NMP) and by oxygen plasma etching for 15 minutes, UV/ozone exposure for 30 min and by plasma ashing for 50 minutes.

The second method of the transfer of potentiostatically electrodeposited Bi_2Te_3 thin films at -1 V vs. Ag/AgCl was with thermal release tape (Thermal Release Sheet for Electronic Component Processing REVALPHA, Nitto). The tape was placed on top of the film and left to float in AZ400K for 30, 75 and 90 minutes. After the separation, the tape with the film was transferred onto 50 nm thick SiO_2 layer thermally grown on the Si wafer and baked at 150 °C to release the film.

A modification of the transfer method with PMMA of potentiostatically electrodeposited Bi_2Te_3 thin films at -1 V vs. Ag/AgCl from TiN substrates onto SiO_2 and fused silica substrates was carried out in AZ 400K using PS as a carrier polymer. Figure 4.15 shows schematic diagram of the transfer process. For this transfer process, either 9 or 20 W/V % PS/toluene solution was spin-coated on the Bi_2Te_3 thin films. The samples were then baked at 85 °C for 30 min to dry the polymer. A cut was made on the samples to allow water to penetrate between Bi_2Te_3 films coated with PS and TiN substrates. The samples were dipped either into deionised (DI) water or AZ 400K solution which resulted in exfoliation of Bi_2Te_3 films coated with PS from TiN substrates. Films coated with polymer were then transferred onto insulating substrates and left to dry in air for 3 days. As the target substrates, thermally grown 50 nm SiO_2 on Si wafer, fused silica and fused silica activated with O_2 plasma for 5 min in order to improve adhesion of transferred films were chosen. Finally, the carrier polymer was removed from Bi_2Te_3 films by dipping the samples in chloroform. The films were then dipped into acetone and isopropanol to remove the solvent.

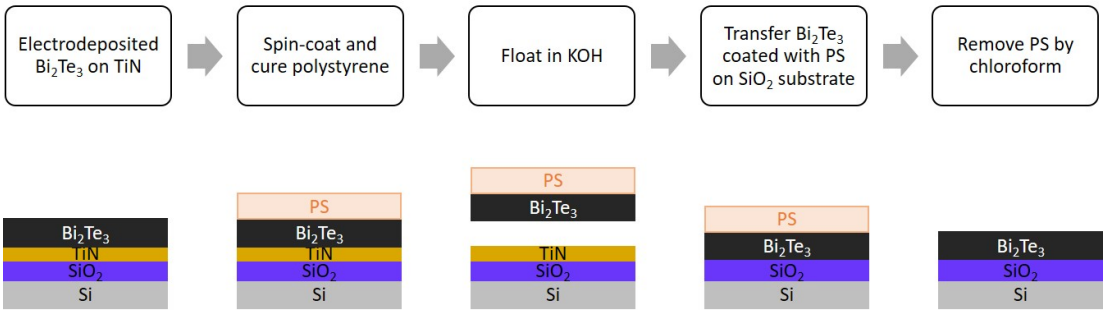

FIGURE 4.15: Schematic diagram of polystyrene-based transfer process of Bi_2Te_3 electrodeposited on TiN to an insulating SiO_2 substrate.

Chapter 5

Thermoelectric Properties of Bismuth Telluride Thin Films Electrodeposited from Dichloromethane

5.1 Preliminary work on electrodeposition of bismuth telluride thin films from dichloromethane

The initial experiments carried out in our group to explore the electrochemistry of individual precursors ($[N^nBu_4][BiCl_4]$ and $[N^nBu_4]_2[TeCl_6]$ in CH_2Cl_2) and investigate the deposition of bismuth telluride thin films from dichloromethane were published in [43]. Figure 5.1 shows cyclic voltammetry experiments of individual precursors $[N^nBu_4][BiCl_4]$ and $[N^nBu_4]_2[TeCl_6]$ in CH_2Cl_2.

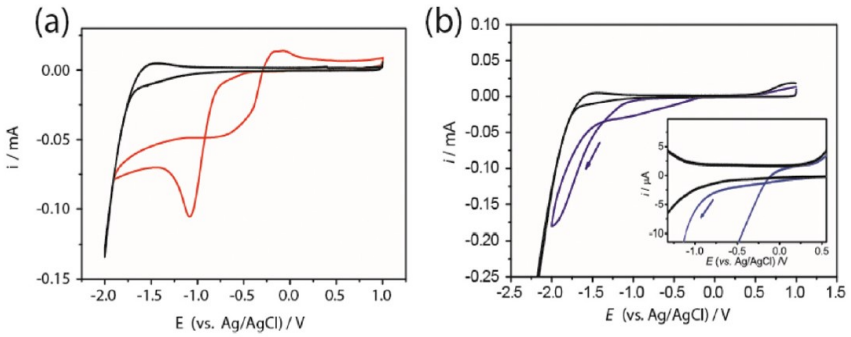

FIGURE 5.1: First cycle cyclic voltammograms for the reduction of a) 2 mM $[N^nBu_4][BiCl_4]$ and b) 3 mM $[N^nBu_4]_2[TeCl_6]$ in 0.1 M $[N^nBu_4]Cl$ in CH_2Cl_2 at TiN electrodes. The scan rate is 50 mV s^{-1}. The black curve for both voltammograms represents the background for 0.1 M $[N^nBu_4]Cl$ in CH_2Cl_2. Reprinted from [43].

Fig. 5.1a shows the voltammetry for reduction of $[N^nBu_4][BiCl_4]$ with 0.1 M $[N^nBu_4]Cl$ in CH_2Cl_2 (red) and the background scan of supporting electrolyte alone (0.1 M $[N^nBu_4]Cl$ (black) in CH_2Cl_2) on TiN electrodes scanning negatively from 1 V to -2 V and back to 1 V. The voltammetry for the reduction of $[N^nBu_4][BiCl_4]$ shows an increase in current at *ca.* -0.6 V vs. Ag/AgCl with the reduction peak at -1.2 V vs. Ag/AgCl and the nucleation loop on the return scan. Scanning positively there is a broad stripping peak at *ca.* -0.1 V vs. Ag/AgCl. The total charge passed for reduction of $[BiCl_4]^-$ is 3.2 mC, while the charge for oxidative stripping is 0.5 mC indicating that the deposited Bi is not fully oxidised. Fig 5.1b shows the voltammetry for reduction of $[N^nBu_4]_2[TeCl_6]$ with 0.1 M $[N^nBu_4]Cl$ in CH_2Cl_2 (blue) on TiN electrodes scanning negatively from 1 V to -2 V and back to 1 V. Here as well black represents the background scan of supporting electrolyte alone (0.1 M $[N^nBu_4]Cl$ in CH_2Cl_2). There are no clear reduction peaks for the reduction of $[TeCl_6]^{2-}$, however, an increase in current is observed for the cathodic scan starting at *ca.* 0.2 V vs. Ag/AgCl which indicates onset of reduction of $[TeCl_6]^{2-}$. The current crossing over at -1.4 V vs. Ag/AgCl on the return scan is larger than on the forward scan, indicating the reduction of $[TeCl_6]^{2-}$ on the as-deposited Te. On the anodic scan a broad and small peak is observed starting at 0.25 V vs. Ag/AgCl which corresponds to anodic stripping of Te. The total charge passed for stripping is clearly much lower than that passed for the reduction.

Fig. 5.2 shows SEM images and EDX measurements of Bi (Fig 5.2a) and Te (Fig 5.2b) electrodeposited on TiN electrode at -2.0 V vs. Ag/AgCl from 2 mM $[N^nBu_4][BiCl_4]$ and 3 mM $[N^nBu_4]_2[TeCl_6]$, respectively, for 600 s.

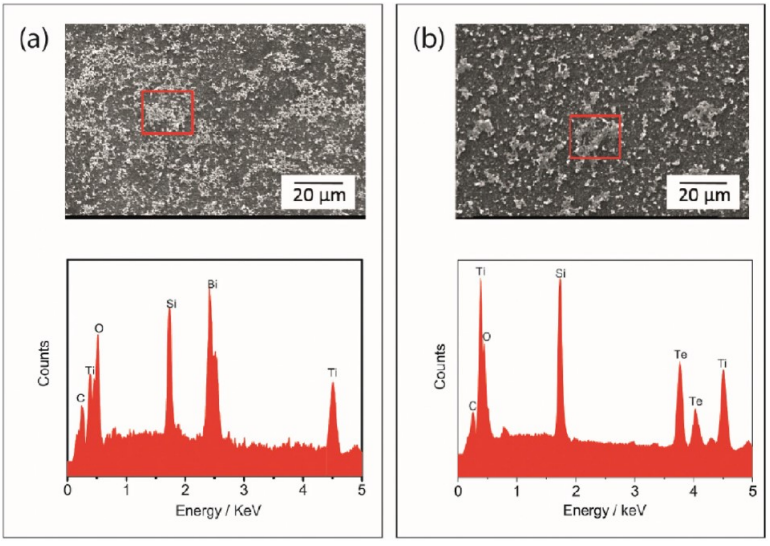

FIGURE 5.2: SEM images and EDX spectra collected on Bi (a) and Te (b) deposits electrodeposited at -2.0 V vs. Ag/AgCl on TiN electrode for 600 s from electrolytes containing 2 mM $[N^nBu_4][BiCl_4]$ and 3 mM $[N^nBu_4]_2[TeCl_6]$, respectively, with 0.1 M $[N^nBu_4]Cl$ in CH_2Cl_2. Reprinted from [43].

SEM images on Fig. 5.2a and b confirms deposits consisting of islands/flakes. EDX spectra on Fig. 5.2a and b show peaks for Bi and Te, respectively, with Ti and Si signals

coming from the substrate. The thicknesses of the deposits measured by cross-sectional SEM are larger by a factor of 4 and 3.5 for Bi and Te deposits, respectively, than the calculated values due to the porosity of the deposits.

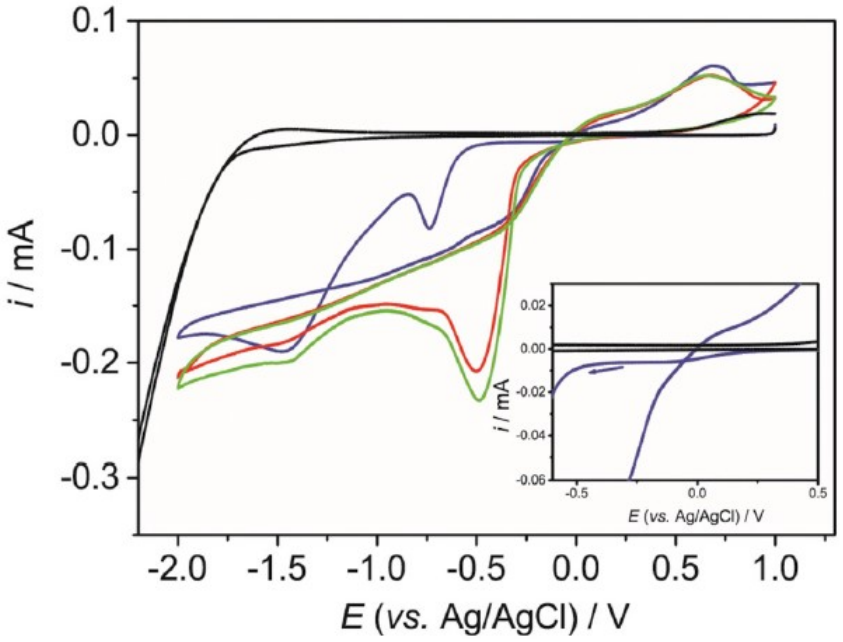

FIGURE 5.3: Three consecutive CVs for the reduction of 2 mM $[N^nBu_4][BiCl_4]$ and 3 mM $[N^nBu_4]_2[TeCl_6]$ in CH_2Cl_2 solution containing 0.1 M $[N^nBu_4]Cl$ supporting electrolyte on a 4 mm diameter TiN electrode. The scan rate is 50 mV s^{-1}. Blue: 1st scan, red: 2nd scan, green: 3rd scan. Black: background scan in 0.1 M $[N^nBu_4]Cl$ supporting electrolyte CH_2Cl_2. Reprinted from [43].

Cyclic voltammetry in an electrolyte containing $[N^nBu_4][BiCl_4]$ and $[N^nBu_4]_2[TeCl_6]$ was carried out to study the deposition of bismuth telluride. Figure 5.3 shows three consecutive cycles for reduction of 2 mM $[N^nBu_4][BiCl_4]$ and 3 mM $[N^nBu_4]_2[TeCl_6]$ with 0.1 M $[N^nBu_4]Cl$ supporting electrolyte in CH_2Cl_2 at TiN electrode. The black curve represents the background scan in 0.1 M $[N^nBu_4]Cl$ supporting electrolyte CH_2Cl_2. Scanning negatively in the first scan (blue curve) a small reduction wave is observed at *ca.* 0.2 V, similar to what is seen for $[TeCl_6]^{2-}$ reduction in Fig 5.1b. This is ascribed to the reduction of $[TeCl_6]^{2-}$ to Te(0). By scanning further negative on the first scan, two reduction peaks are seen at -0.75 and -1.4 V. The passed charge under the peak at -0.75 V is twice of the wave at 0.2 V, and this is ascribed to deposition of Bi onto already deposited Te to TiN electrode. This statement was confirmed by the experiment where Bi was electrodeposited from the solution containing $[N^nBu_4][BiCl_4]$ onto Te coated electrode and the peak at -0.75 V was seen. On the return scan the reduction current is larger and a broad stripping peak appears starting at *ca.* 0.0 V. The charge passed for oxidative stripping is 9% of the charge passed for the reduction indicating that the deposited Bi and Te are not completely oxidised. On the second and third scan the reduction current is larger, with the large reduction peak at *ca.* -0.4 V. This change in voltammetry for the second and third scan is due to the modified electrode surface as

the material is not fully oxidised after the first scan resulting in facilitated deposition onto already deposited material. The oxidative stripping for the second and third scan is very similar to the first scan in both potential and current.

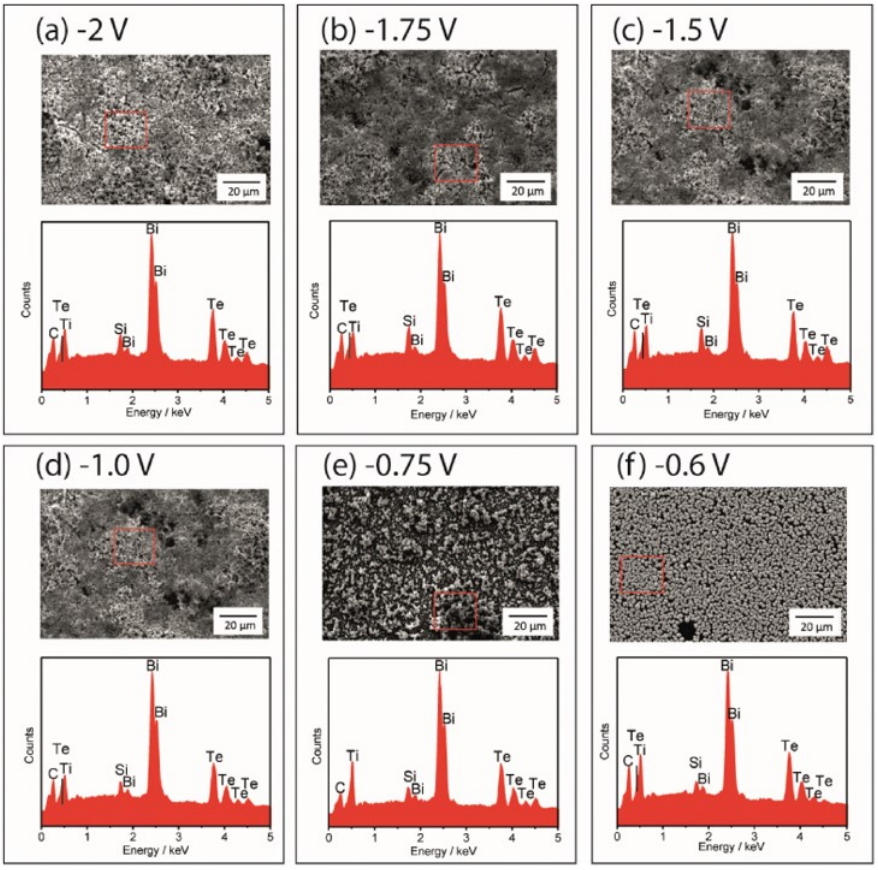

FIGURE 5.4: SEM images and EDX spectra collected on bismuth telluride deposits electrodeposited at a) -2.0 , b) -1.75, c) -1.5, d) -1.0, e) -0.75 and f) -0.6 V vs. Ag/AgCl from 2 mM $[N^nBu_4][BiCl_4]$ and 3 mM $[N^nBu_4]_2[TeCl_6]$ in CH_2Cl_2 solution containing 0.1 M $[N^nBu_4]Cl$ supporting electrolyte on TiN electrode for 600 s. Reprinted from [43].

Fig. 5.4 shows SEM images and EDX spectra for bismuth telluride films electrodeposited from 2 mM $[N^nBu_4][BiCl_4]$ and 3 mM $[N^nBu_4]_2[TeCl_6]$ in CH_2Cl_2 solution containing 0.1 M $[N^nBu_4]Cl$ supporting electrolyte at -2.0 , -1.75, -1.5, -1.0, -0.75 and -0.6 V vs. Ag/AgCl on TiN electrode for 600 s. The chosen potentials for electrodeposition are based on the peak locations in cyclic voltammetry (Fig. 5.3). The films electrodeposited at potentials more negative than -1.5 V are uniform with minor cracks and pinholes. At less negative deposition potentials of -1.0 and -0.75 V the deposits comprise discrete islands with an underlying film, while at -0.6 V the deposits consist of dense crystalline particles. The corresponding EDX spectra show signals of both Bi and Te as well as Si and Ti signals coming from the substrate. The signal intensities for Bi and Te remain nearly constant for all deposition potentials indicating that the film composition is independent, or weakly dependent on the deposition potentials. A cross section SEM image of the film electrodeposited at -2 V reveals thickness 4 times larger than the

calculated, which is due to the porosity of the film. An investigation of the effect of the precursor concentration on the film morphology was conducted with the fixed 3 mM $[N^nBu_4]_2[TeCl_6]$ and varied $[N^nBu_4][BiCl_4]$ concentration (3 mM, 2.5 mM and 2 mM). Electrodeposition was performed at -2.0 , -1.75, -1.5, -1.0, -0.75 and -0.6 V vs. Ag/AgCl on TiN electrode for 600 s. The morphologies of the films electrodeposited with 3 mM and 2.5 mM $[N^nBu_4][BiCl_4]$ have similar morphologies to the films electrodeposited with 2 mM $[N^nBu_4][BiCl_4]$ at different potentials. A relatively constant Bi content at different deposition potentials was also seen for the deposition from electrolyte containing 3 mM $[N^nBu_4][BiCl_4]$ and 3 mM $[N^nBu_4]_2[TeCl_6]$, and the solution containing 2.5 mM $[N^nBu_4][BiCl_4]$ and 3 mM $[N^nBu_4]_2[TeCl_6]$. This is shown in Fig. 5.5.

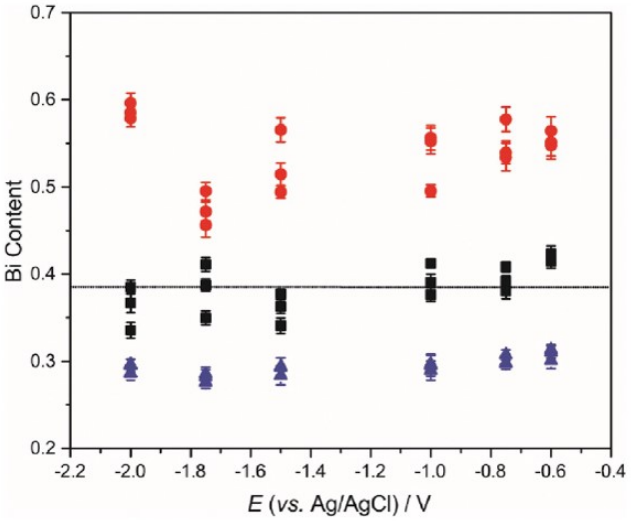

FIGURE 5.5: Bi content for bismuth telluride films electrodeposited at various potentials from electrolyte solution containing 3 mM $[N^nBu_4][BiCl_4]$ and 3 mM $[N^nBu_4]_2[TeCl_6]$ (red), 2.5 mM $[N^nBu_4][BiCl_4]$ and 3 mM $[N^nBu_4]_2[TeCl_6]$ (black) and 2 mM $[N^nBu_4][BiCl_4]$ and 3 mM $[N^nBu_4]_2[TeCl_6]$ (blue) with 0.1 M $[N^nBu_4]Cl$ supporting electrolyte in CH_2Cl_2 on TiN electrode for 600 s. Reprinted from [43].

Fig. 5.6 shows X-ray diffraction patterns for bismuth telluride deposits electrodeposited at various potentials. Fig. 5.6a shows the patterns for films electrodeposited from a solution containing 2.5 mM $[N^nBu_4][BiCl_4]$ and 3 mM $[N^nBu_4]_2[TeCl_6]$, where the peaks are attributed to trigonal Bi_2Te_3 with 2θ angles of 27.59°, 38.10° and 40.80°. In addition, the EDX data collected on the films show close composition to Bi_2Te_3. The patterns do not show the presence of elemental Bi, however, elemental Te shares many reflection positions with Bi_2Te_3 and cannot be discounted. The highest intensity peak is of 015 reflection at 27.59°, broadening at more negative overpotential indicating decreasing crystallite sizes due to the higher nucleation rate at higher overpotentials. Fig. 5.6b shows the patterns for films electrodeposited from a solution containing 3 mM $[N^nBu_4][BiCl_4]$ and 3 mM $[N^nBu_4]_2[TeCl_6]$, where the peaks can be assigned to either Bi_2Te_3 or Bi_4Te_3. The EDX data show closer composition to Bi_4Te_3, the peaks are therefore assigned to the cystal structure of Bi_4Te_3. The highest intensity peak at

107 reflection at 27.52° broadens with more negative overpotentials pointing out smaller crystallite sizes at higher overpotentials here as well.

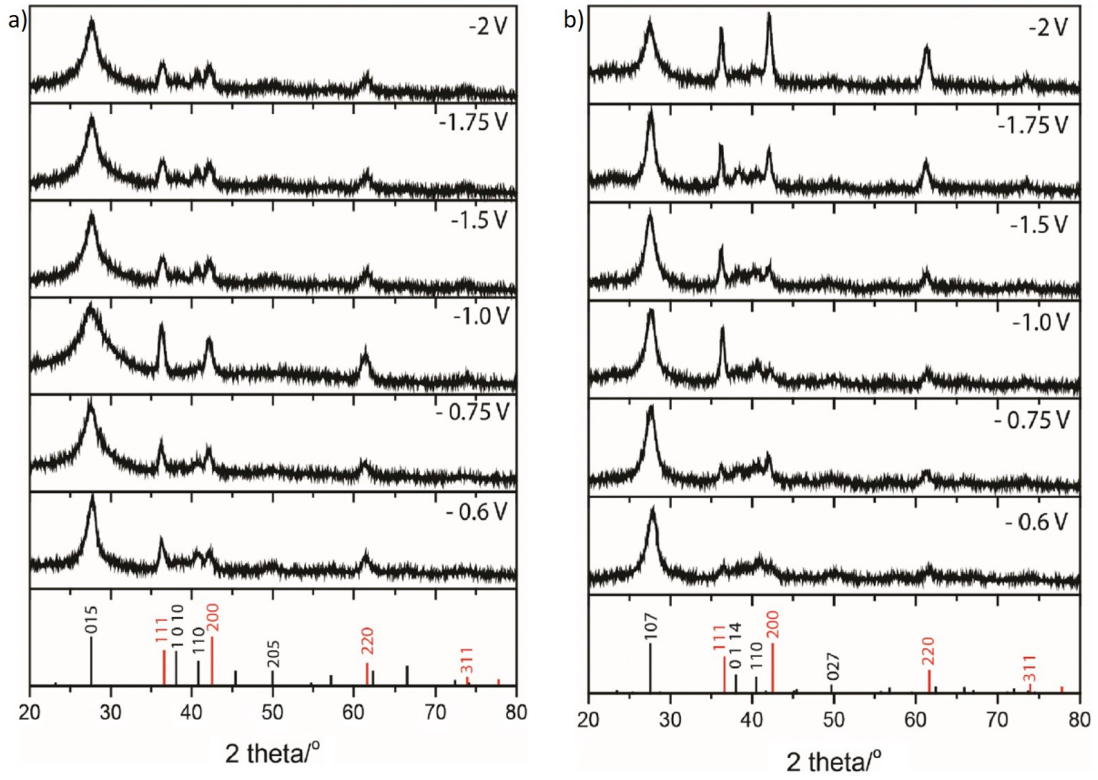

FIGURE 5.6: Grazing incidence XRD patterns of Bi_2Te_3 and Bi_4Te_3 electrodeposited at various potentials on TiN electrode from a solution containing 3 mM $[N^nBu_4]_2[TeCl_6]$ and either a) 2.5 mM $[N^nBu_4][BiCl_4]$ or b) 3 mM $[N^nBu_4][BiCl_4]$ with added 0.1 M $[N^nBu_4]Cl$ supporting electrolyte in CH_2Cl_2. The stick patterns at the bottom represent standard patterns for a) TiN (red) and Bi_2Te_3 (black), and b) TiN (red) and Bi_4Te_3 (black) with Miller indices of key reflections. Reprinted from [43].

To summarise, bismuth telluride thin films were electrodeposited from an electrolyte containing $[N^nBu_4][BiCl_4]$ and $[N^nBu_4]_2[TeCl_6]$ with addion of $[N^nBu_4]Cl$ as a supporting electrolyte in CH_2Cl_2 for the first time. It is shown that the composition of bismuth telluride films varies with precursors concentration but not with the deposition potential. From the solution containing 2.5 mM $[N^nBu_4][BiCl_4]$ and 3 mM $[N^nBu_4]_2[TeCl_6]$ stoichiometric Bi_2Te_3 were obtained as demonstrated by EDX data and XRD patterns. In addition, the diffration patterns show that the crystallite sizes decrease with films electrodeposited at higher overpotentials due to the higher nucleation rate.

5.2 Electrodeposition of bismuth telluride thin films from dichloromethane

The preliminary work on electrodeposition of bismuth telluride thin films from an electrolyte containing $[N^nBu_4][BiCl_4]$ and $[N^nBu_4]_2[TeCl_6]$ as Bi and Te precursors, respectively, with $[N^nBu_4]Cl$ as a supporting electrolyte in CH_2Cl_2 showed that it is possible to obtain bismuth telluride compound. However, the obtained films electrodeposited potentiostatically were very porous and insulating, and as such not useful for thermoelectric applications. Therefore, more work is needed to explore electrodeposition conditions which give dense, compact and conductive films. Prior to electrodeposition, cyclic voltammetry in an electrolyte containing 2.25 mM $[N^nBu_4][BiCl_4]$ and 3 mM $[N^nBu_4]_2[TeCl_6]$ was performed to ensure electrodeposition can be carried out from the prepared electrolyte. Figure 5.7 shows three consecutive cycles for $[N^nBu_4][BiCl_4]$ and $[N^nBu_4]_2[TeCl_6]$ in 0.1 M $[N^nBu_4]Cl$ supporting electrolyte scanning negatively from 1 V to -2 V and back to 1 V at GC working electrode. Scanning negatively in the first scan (black curve) two reduction peaks are observed at -0.75 and -1.4 V. The first peak at -0.75 V was attributed to the underpotential deposition of Bi onto already deposited Te in [43]. The charge under the reduction peaks was calculated to be 3.3 mC. On the return scan there is a large oxidation peak starting from *ca.* -0.2 C and the second oxidation peak at 0.7 V. The charge calculated for oxidative stripping peak is 1.4 mC, which is 42 % of the reduction charge value indicating that the deposited Bi_2Te_3 is not completely oxidised. On the second and third scan (red and blue curve, respectively), the two reduction peaks are noticeable as well. The fist peaks at -0.75 V vs. Ag/AgCl corresponds to the same position as in the first scan, however the reduction current is larger. The second peak at -1.3 V vs. Ag/AgCl is shifted towards more positive potential in comparison to the first scan. This change in voltammetry for the second and third scan is due to the modified electrode surface as the material is not fully oxidised after the first scan resulting in facilitated deposition onto already deposited material. The oxidative stripping for the second and third scan is very similar to the first scan in both potential and current.

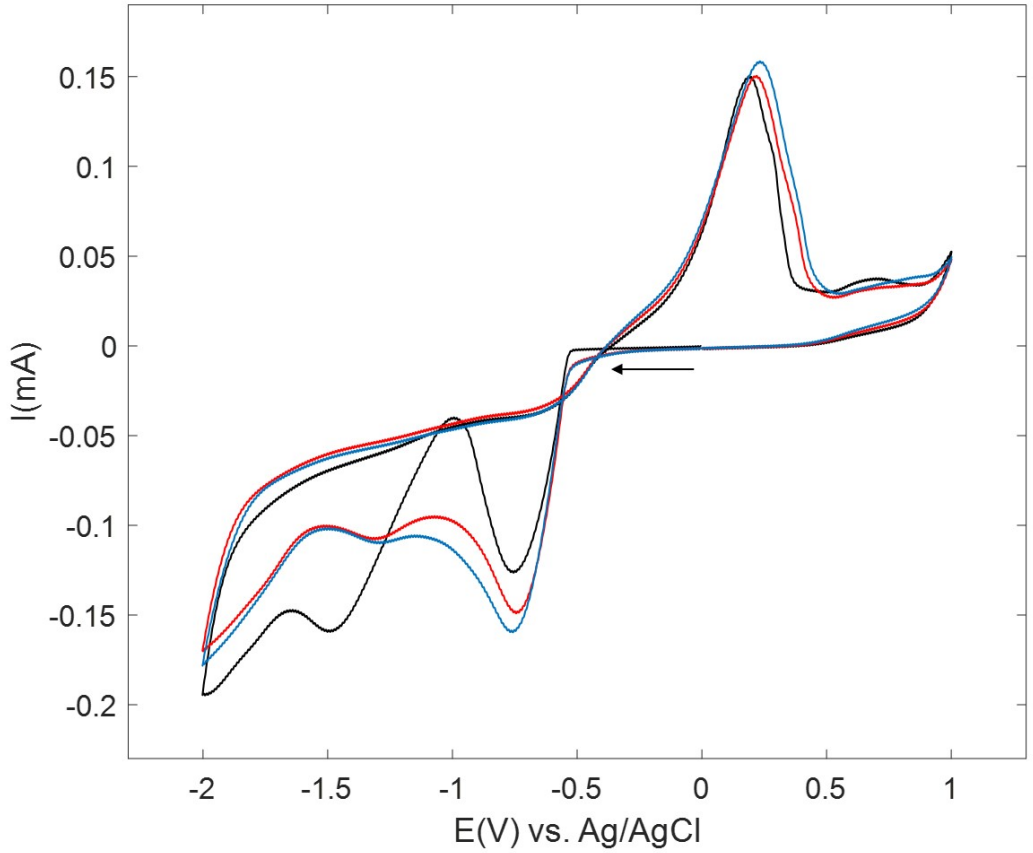

FIGURE 5.7: Three consecutive CVs for the reduction of 2.25 mM $[N^nBu_4][BiCl_4]$, 3 mM $[N^nBu_4]_2[TeCl_6]$ in CH_2Cl_2 solution containing 0.1 M $[N^nBu_4]Cl$ supporting electrolyte on a 3 mm diameter GC electrode. The scan rate is 50 mV s^{-1}. Black: 1st scan, red: 2nd scan, blue: 3rd scan.

5.3 Characterisation of as-deposited films

5.3.1 SEM images and EDX elemental composition

In order to improve the film morphology of the Bi_2Te_3 films electrodeposited using potentiostatic conditions in our previous work [43], conditions of pulsed electrodeposition have been optimised. Pulsed electrodeposition is performed by alternating a constant potential (E_{on}) for a certain period of time (t_{on}), and an open circuit potential (E_{off}) for a period t_{off}. Figure 5.8 provides schematics and SEM images of bismuth telluride films electrodeposited potentiostatically (Fig. 5.8a,b) and by pulsed deposition for various different on- and off-time pulses at -1.0 V vs. Ag/AgCl (Fig. 5.8c-h) with a passed charge of -1.3 C which yields a nominal thickness of 1 μm. As can be seen in Fig 5.8, all films exhibit porous morphologies, however, somewhat smoother films can be obtained under pulsed deposition conditions compared to potentiostatically electrodeposited films. Table 5.1 provides EDX elemental composition measured on three different areas on each film. The table shows that the films consist of the elements Bi, Te, O, Si, Ti, and C. The presence of Bi and Te confirms the deposition of bismuth telluride. The presence of Si and Ti are signals from SiO_2 and TiN in the substrate, respectively. C signal comes from adventitious carbon contamination on the surface. O signal could come from both SiO_2 in the substrate and oxidation of Bi_2Te_3. Small standard deviations ($\leqslant$0.05) in Bi to Te ratios in all films regardless of the method shows excellent uniformity of deposits over the given area.

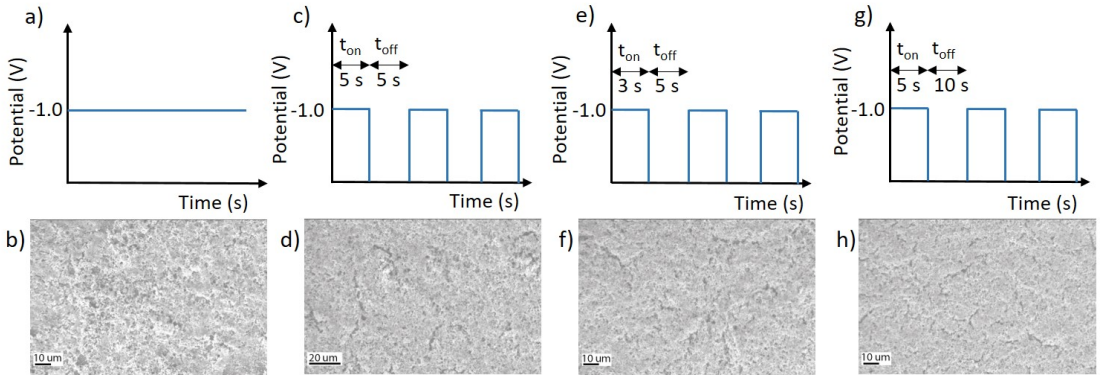

FIGURE 5.8: Schematics and SEM images for potentiostatic (a,b), and pulsed (c-h), electrodeposition of bismuth telluride for t_{on}=5 s t_{off}=5 s (c,d), t_{on}=3 s t_{off}=5 s (e,f), t_{on}=5 s t_{off}=10 s at -1.0 V vs. Ag/AgCl.

The experiments under the same conditions were repeated three times in order to examine composition repeatability for potentiostatic and pulsed electrodeposition. Table 5.2 provides Bi to Te ratios from three different films electrodeposited under the same deposition conditions and solution concentrations, average values of the ratios and their standard deviations. The standard deviation of average Bi to Te ratio of three different films grown potentiostatically is 0.20, while for the films grown under pulsed conditions

TABLE 5.1: Elemental composition showing atomic percentage of each element measured on three different areas of the film. All films are electrodeposited at -1 V vs. Ag/AgCl from an electrolyte containing 2.5 mM $[N^nBu_4][BiCl_4]$, 3 mM $[N^nBu_4]_2[TeCl_6]$ in CH_2Cl_2 solution containing 0.1 M $[N^nBu_4]Cl$ supporting electrolyte by different methods.

	% atomic							
Method	Bi	Te	Si	O	Ti	C	Bi:Te	Average Bi:Te± stdev
Potentiostatic	18.0	29.1	1.0	32.4	1.9	17.6	0.6	0.6±0.01
	18.8	30.0	0.9	31.1	2.0	17.2	0.6	
	19.4	30.5	0.8	30.4	1.8	17.1	0.6	
Pulsed (t_{on}/t_{off}=5s/5s)	10.6	16.0	13.3	28.5	24.3	7.4	0.7	0.7±0.05
	14.4	22.0	8.35	29.1	16.3	9.9	0.7	
	23.9	32.4	0.0	27.6	0.0	16.1	0.7	
Pulsed (t_{on}/t_{off}=3s/5s)	24.6	29.5	0.8	31.9	0.0	13.2	0.8	0.8±0.01
	24.6	29.1	0.6	31.6	0.0	14.1	0.9	
	24.9	30.1	0.9	29.3	0.0	14.8	0.8	
Pulsed (t_{on}/t_{off}=5s/10s)	24.3	31.0	0.0	30.0	0.0	14.7	0.8	0.8±0.03
	24.7	32.5	0.4	28.2	0.0	14.2	0.8	
	24.0	33.0	0.5	29.1	0.0	13.4	0.7	

is significantly lower ($\leqslant$0.06). Therefore, this proves that the films grown by pulsed electrodeposition exhibit improved composition repeatability compared to those grown potentiostatically. Namely, bismuth telluride electrodeposition is a diffusion controlled process meaning that the loss of ions occurs at the electrode surface under potentiostatic conditions after a certain amount of time. During off-time under pulsed deposition condition, the ion concentration at the electrode surface replenishes in the diffusion layer causing a change in the electrical double layer. Hence, under pulsed conditions the composition of the films can be better controlled due to the replenishment of the ions in each cycle [18]. Although all pulsing condition yield similar morphologies, the conditions with on-time 5 s and off-time 10 s (5.8h) were chosen for further improvement of bismuth telluride thin film surface morphology, as it possesses the lowest signals in Si and Ti coming from the substrate indicating the most compact morphology.

For further investigation of the films morphology improvement, nucleation of the film has been optimised. The Bi_2Te_3 films were grown by introducing a short initial nucleation pulse at a high overpotential which generates a large number of nuclei, and then growing them potentiostatically or by pulsed deposition at lower overpotential. Firstly, the early stage of film growth was investigated by applying a short nucleation pulse at high overpotentials after which the nuclei were grown potentiostatically at -0.6 V vs. Ag/AgCl with a passed charge of -0.26 C, which would correspond to 200 nm thickness assuming a uniform distribution over the whole electrode area. Figure 5.9 shows a schematic, SEM images and histograms of the size distribution of the resulting deposited

TABLE 5.2: Bi to Te ratios of three different films electrodeposited at -1 V vs. Ag/AgCl from electrolyte containing 2.5 mM $[N^nBu_4][BiCl_4]$, 3 mM $[N^nBu_4]_2[TeCl_6]$) and 0.1 M $[N^nBu_4]Cl$, average values and standard deviations.

Method	Bi:Te	Average Bi:Te±stdev
Potentiostatic	0.3	0.4±0.20
	0.4	
	0.6	
Pulsed (t_{on}/t_{off}=5s/5s)	0.8	0.7±0.06
	0.7	
	0.7	
Pulsed (t_{on}/t_{off}=3s/5s)	0.8	0.8±0.01
	0.8	
	0.8	
Pulsed (t_{on}/t_{off}=3s/5s)	0.8	0.8±0.03
	0.8	
	0.8	

particles. The deposits were grown by applying an initial nucleation pulse of -1.0 V, -1.2 V, and -1.4 V vs. Ag/AgCl for 1, 3, or 5 s. As can been seen from the figure, by increasing the length of the nucleation pulse, increased coverage of the substrate surface was achieved with smaller and more uniform particles. In addition, by applying a higher initial overpotential for the same amount of time the same effect of generating smaller, denser and more uniform nuclei was achieved. This indicates progressive nucleation meaning that the nucleation process is slow and new nuclei continue to form during the deposition while those already formed continue to grow. Hence, by applying a potential of -1.4 V for 5 s and then growing the nuclei at -0.6 V vs. Ag/AgCl, almost full coverage of uniform, densely packed particles was obtained. ImageJ [109] was used to extract the number and the areal size of the electrodeposited crystallites plotted as histograms. The deposits formed with nucleation potentials of -1.0 V for 5 s and -1.4 V for 5 s show particle counts of at least a factor of 10 higher than the deposited formed with shorter pulses at lower potential. This corresponds to a volume particle size reduction of the same factor. These nucleation pulse values were therefore selected for further investigation and optimisation of bismuth telluride thin film growth.

Figure 5.10 shows linear (a) and quadratic (b) fit of cathodic current increase region which is due to either growth of independent nuclei (instantaneous nucleation) or simultaneous growth of independent nuclei and formation of new ones (progressive nucleation), as discussed earlier. The linear relationship of current-time corresponds to instantaneous nucleation, and the quadratic corresponds to progressive nucleation. As can be seen from the figure, the coefficient of determination R^2 equals 1 for quadratic

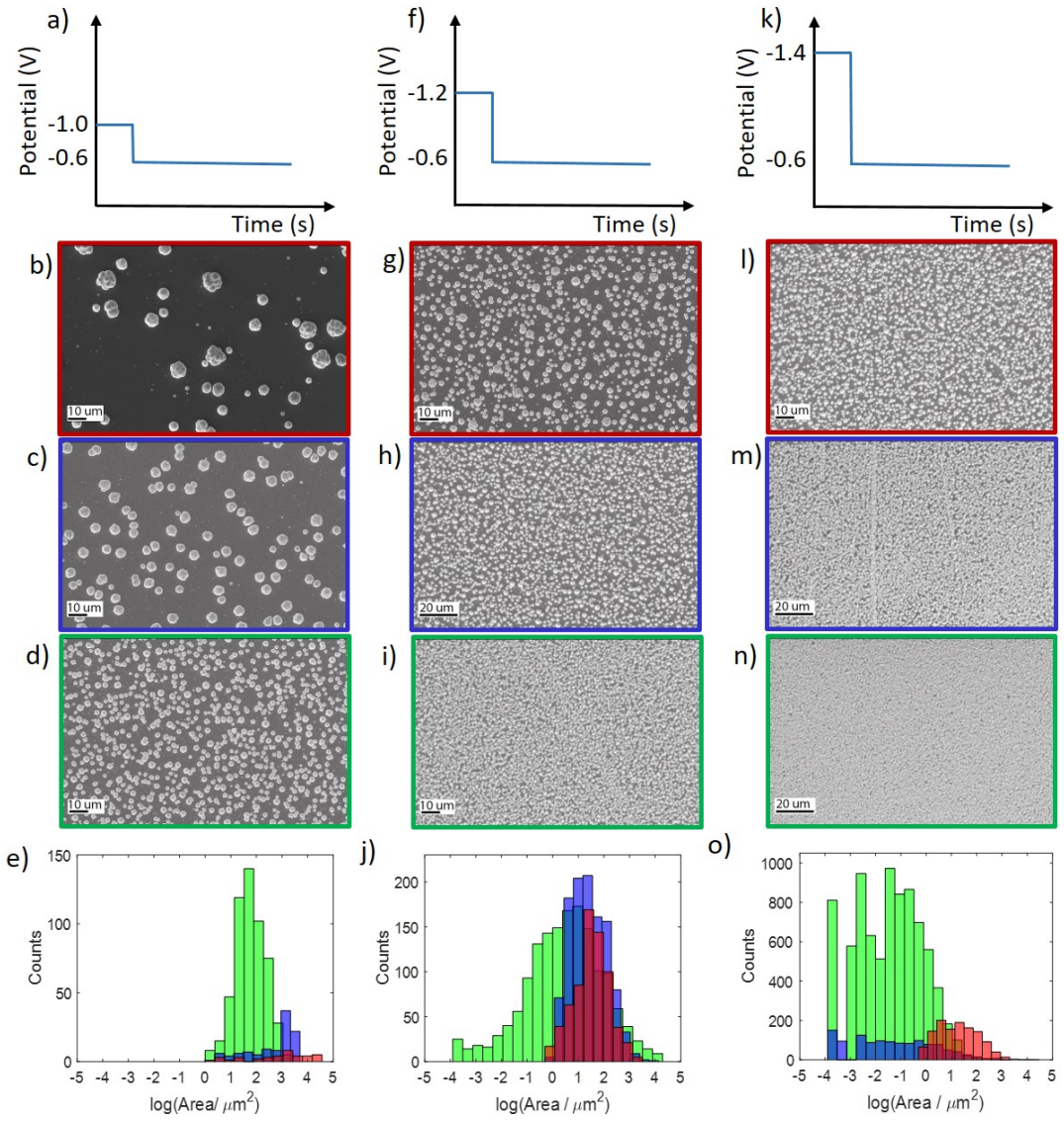

FIGURE 5.9: SEM images and histograms of electrodeposited bismuth telluride deposits grown at E_{dep}=-0.6 V, preceded by nucleation pulses of E_{nuc}=-1.0 V (a-e), -1.2 V (f-j) and -1.4 V vs. Ag/AgCl (k-o) with nucleation pulse times t_{nuc}=1 s (red: b,g,l), 3 s (blue: c,h,m), and 5 s (green d,i,n).

fit meaning that the fit is perfect, while for the linear is below 1. Therefore, this proves that the nucleation of bismuth telluride from dichloromethane is progressive.

Figure 5.11 shows SEM images of films grown potentiostatically (5.11b,c,d), by pulsed electrodeposition (5.11f,g,h), potentiostatically preceded by a nucleation pulse (5.11j,k), and by pulsed deposition preceded by a nucleation pulse (5.11m,n). As can be seen from Fig. 5.11, the films grown potentiostatically and by pulsed electrodeposition at potentials of -1.0 V (5.11b,f) and -0.8 V (5.11c,g) vs. Ag/AgCl both exhibit similar porous but continuous morphologies. The thickness of the films is estimated to be 1 μm from the total charge passed of -1.3 C for potentiostatically grown films. For the films grown by pulsed deposition, the estimated thickness is 950 nm from the charge

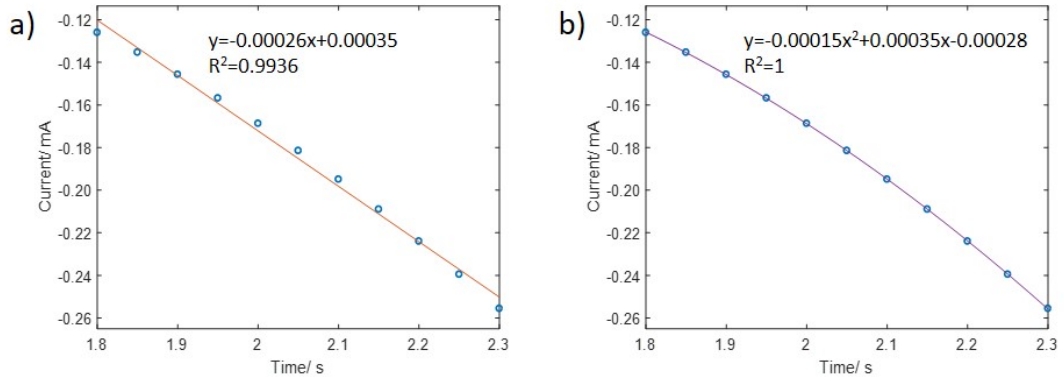

FIGURE 5.10: Potentiostatic current-time transient (i_{free} region) of electrodeposition of Bi_2Te_3 from 2.25 mM $[N^nBu_4][BiCl_4]$, 3 mM $[N^nBu_4]_2[TeCl_6]$ and 0.1 M $[N^nBu_4]Cl$ in CH_2Cl_2 solution at -1.0 V vs. Ag/AgCl on TiN electrode. a) linear fit, and b) quadratic fit.

passed of 1.2 C and 1.4 μm from the charge passed of 1.8 C for films grown at -1.0 and -0.8 V vs. Ag/AgCl, respectively. However, when growing films potentiostatically and by pulsed electrodeposition at a lower potential of -0.6 V vs. Ag/AgCl, a significant change in morphology was observed (5.11d,h). The resulting deposits in this case are not films but rather comprise discontinuous islands. Furthermore, the deposits obtained by pulsed electrodeposition are smoother, slightly larger and more uniform in size than the deposits obtained potentiostatically. The calculated thickness of the uniform film over the given area grown potentiostatically is 1 μm, and 1.8 μm from a charge of -2.3 C for the film grown by pulsed deposition at -0.6 V vs. Ag/AgCl. Table 5.3 gives the average and standard deviation of Bi to Te ratios and atomic percentage of oxygen measured by EDX elemental analysis on three different areas of the films. The presence of Bi and Te confirms the deposition of bismuth telluride, with slight variation of average Bi to Te ratios from stoichiometric composition (0.7) when applying different potentials and deposition methods. Furthermore, the small standard deviation ($\leq$ 0.05) in Bi to Te ratios obtained in all films proves excellent composition uniformity regardless of the method. The O signal most probably indicates oxidation of the bismuth telluride films.

Comparing to films grown without a nucleation pulse, the films were grown potentiostatically and by pulsed electrodeposition preceded by a nucleation pulse. As can be seen in Figure 5.11, considerable change in morphology is noticeable between films grown potentiostatically (5.11j,k) and by pulsed electrodeposition (5.11m,n) after introducing an initial nucleation pulse at higher potential. The films grown by pulsed electrodeposition are compact, continuous and smooth, while those grown potentiostatically are discontinuous. The importance of introducing a nucleation pulse at high deposition current followed by the film growth galvanostatically at lower current was reported in [110], where copper zinc tin sulfo-selenide thin films obtained in this way were much smoother than those grown without a nucleation pulse. Cross section SEM images of the films grown potentiostatically and by pulsed electrodeposition preceded by a nucleation pulse

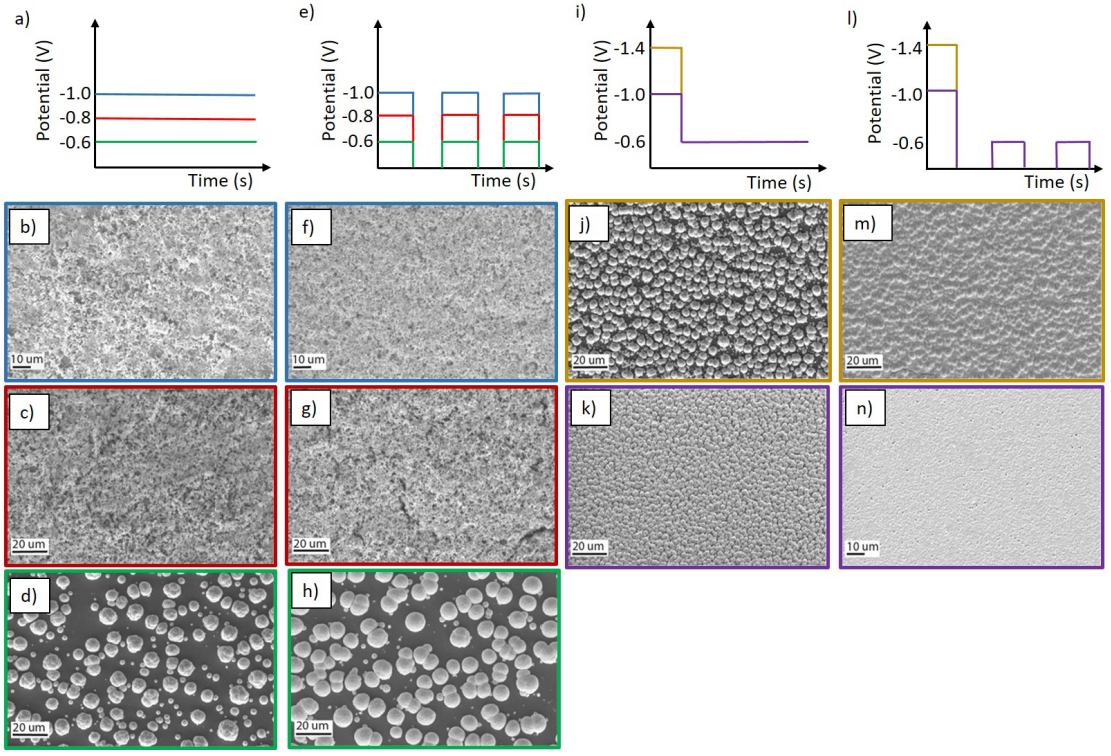

FIGURE 5.11: Schematics and SEM images of potentiostatic (a-d), pulsed (e-h), potentiostatic preceded by nucleation pulse (i-k), and pulsed preceded by nucleation pulse (l-n) bismuth telluride deposition for potentials of -1.0 V (b,f), -0.8 V (c,g), -0.6 V (d,h), -0.6 V preceded by nucleation pulse of -1.4 V (j,m) and -1.0 V (k,n) vs. Ag/AgCl. ton=5 s and toff=10 s for all pulsed electrodepositions.

are shown in Fig. 5.12. The calculated thickness of the deposits electrodeposited potentiostatically is 1 μm. For the films grown by pulsed electrodeposition, the calculated thickness from the passed charge of -0.6 C is 500 nm and 1.4 μm for charge of -1.8 C for nucleation potentials of -1.0 and -1.4 V vs. Ag/AgCl, respectively. Cross section SEM images of the films electrodeposited by pulsed electrodeposition preceded by a nucleation pulse reveals the actual thicknesses of 675 nm and 2 μm for nucleation pulses of -1.0 and -1.4 V vs. Ag/AgCl, respectively. The 35 % discrepancy between the calculated and measured value is possibly due to the residual porosity in the films. On the other hand, the calculated thickness of the porous film electrodeposited potentiostatically at -1 V vs. Ag/AgCl is 1 μm, while the cross sectional SEM reveals a thickness of 4.5 μm. This large factor of 4 discrepancy between theoretical and measured value is due to the porosity of the film, as can be seen in Fig. 5.12a. Figure 5.12 b and c show that the porosity is significantly reduced in the films grown by pulsed electrodeposition preceded by a nucleation pulse, however, the obtained thicknesses somewhat higher than than the calculated ones could be due to the residual porosity in the films. Furthermore, as shown in Table 5.3, the oxygen content is significantly lower in films grown by pulsed deposition preceded by a nucleation pulse compared to films obtained by other methods. This is probably due to the compact and smooth surface morphology of these films which have a smaller exposed surface area than the porous films, and are therefore less prone

TABLE 5.3: Elemental composition showing Bi to Te ratios and atomic percentage of O measured on three different areas of the film showing average values and standard deviation. All films are electrodeposited from an electrolyte containing 2.25 mM $[N^nBu_4][BiCl_4]$, 3 mM $[N^nBu_4]_2[TeCl_6]$) and 0.1 M $[N^nBu_4]Cl$ by different methods. t_{on}=5 s and t_{off}=10 s for all pulsed depositions.

Method	Potential vs. Ag/AgCl	Bi:Te ± stdev	% atomic O ± stdev
Potentiostatic	E_{dep}=-1.0	0.5 ± 0.01	32.4 ± 1.08
Potentiostatic	E_{dep}=-0.8	0.5 ± 0.01	38.0 ± 0.25
Potentiostatic	E_{dep}=-0.6	0.8 ± 0.03	13.1 ± 0.46
Pulsed	E_{dep}=-1.0	0.7 ± 0.03	33.8 ± 1.83
Pulsed	E_{dep}=-0.8	0.6 ± 0.02	17.8 ± 4.41
Pulsed	E_{dep}=-0.6	0.8 ± 0.05	13.8 ± 3.73
Potentiostatic with nucleation pulse	E_{dep}=-0.6 E_{nuc}=-1.4	0.6 ± 0.04	4.4 ± 0.26
Potentiostatic with nucleation pulse	E_{dep}=-0.6 E_{nuc}=-1.0	0.9 ± 0.01	26.0 ± 1.44
Pulsed with nucleation pulse	E_{dep}=-0.6 E_{nuc}=-1.4	0.5 ± 0.02	0.3 ± 0.50
Pulsed with nucleation pulse	E_{dep}=-0.6 E_{nuc}=-1.0	0.7 ± 0.01	6.5 ± 0.95

to atmospheric oxidation. However, most of the films obtained by different electrodeposition methods from electrolyte containing 2.25 mM and 3 mM Bi and Te precursor concentration, respectively, do not have stoichiometric Bi_2Te_3 composition (Bi:Te=0.7), as can be seen in Table 5.3.

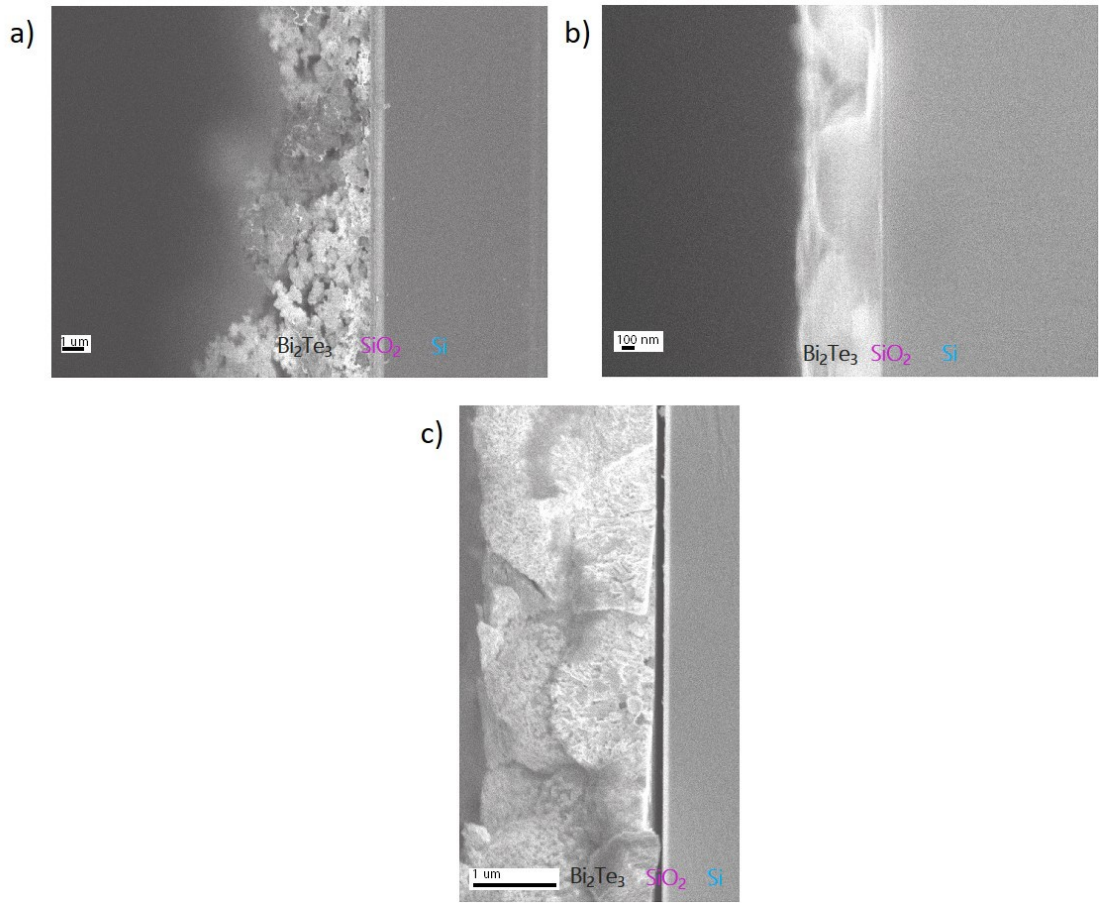

FIGURE 5.12: Cross section SEM images of bismuth telluride films electrodeposited potentiostatically at -1.0 V (a), by pulsed deposition at -0.6 V with an initial nucleation pulse at -1.0 V (b) and -1.4 V (c) vs. Ag/AgCl. t_{on}=5 s and t_{off}=10 s for all pulsed depositions.

5.3.2 X-ray diffractograms

Figure 5.13 shows diffraction pattern of bismuth telluride thin film electrodeposited from dichloromethane and fitted against literature patterns [42]. As can be seen from the figure, the pattern does not match to elemental Bi literature pattern (5.13a), however, many reflection positions do match elemental Te pattern (5.13b). Comparing between Bi_4Te_3 (5.13c) and Bi_2Te_3 literature patterns (5.13d), there is somewhat better agreement with Bi_2Te_3 literature pattern. Furthermore, EDX compositional analysis confirmed that Bi to Te ratio in bismuth telluride thin film electrodeposited from dichloromethane by pulsed deposition at -0.6 V preceded by an initial nucleation pulse at -1.0 V vs. Ag/AgCl is 0.7, closer to Bi_2Te_3 than Bi_4Te_3. The peaks are therefore attributed to trigonal Bi_2Te_3, although the presence of elemental Te cannot be completely discounted as they share many reflection positions.

Figure 5.14 shows the diffraction patterns of bismuth telluride films electrodeposited onto TiN electrodes; there are peaks at 2θ angles of 23.64°, 27.71°, 38.31°, 40.97°, 45.10°and 50.05°. The X-ray diffraction analysis of bismuth telluride thin films electrodeposited by different methods shows that the diffraction patterns are very similar regardless of the method. The 015 reflection at 27.7°is of the highest intensity for all the films, and its width indicates crystallite size with the broadest indicating the smallest and the narrowest indicating the biggest crystallite size. This relationship between the peak width and the crystallite size is given by the Scherrer equation (Eq. 5.1):

$$\tau = \frac{K\lambda}{\beta cos\Theta} \tag{5.1}$$

where τ is the crystallite size, K is dimentionless shape factor (value close to 1), λ is the X-ray wavelength, β is the full width at half maximum (FWHM) and Θ is the Bragg angle. Crystallite sizes of bismuth telluride films electrodeposited by different methods were obtained using the PDXL package and are shown in Table 5.4. The smallest crystallite size was obtained for films electrodeposited potentiostatically at -1 V vs. Ag/AgCl, which corresponds to the highest nucleation rate. The films obtained by pulsed electrodeposition at the same potential exhibit bigger crystallite size. Growing films at an even lower overpotential of -0.6 V vs. Ag/AgCl by pulsed electrodeposition gave much bigger crystallite size due to the lower nucleation rate at the lower overpotential. The films electrodeposited by pulsed electrodeposition at the lower overpotential of -0.6 V vs. Ag/AgCl preceded by a nucleation pulse also possess a larger crystallite size, comparable to those grown without a nucleation pulse. Thus it is possible to alter the crystallite sizes of bismuth telluride films which, in turn, could have a beneficial effect on the electrical conductivity and therefore the thermoelectric properties of the films. As mentioned previously in Chapter 2.3.1, the best thermoelectric properties are achieved in Bi_2Te_3 crystals with 110 crystallographic orientation (perpendicular to the

TABLE 5.4: Lattice parameters and crystallite sizes for different bismuth telluride films from X-ray diffraction data obtained using the PDXL programme.

Method	Potential/ V vs.Ag/AgCl	a (Å)	c (Å)	Crystallite size (Å)
Potentiostatic	E_{dep}=-1.0	4.16(10)	30(3)	18
Pulsed	E_{dep}=-1.0	4.1(4)	30.0(19)	27
Pulsed	E_{dep}=-0.6	4.48(6)	28.8(5)	35
Pulsed with an initial nucleation pulse	E_{dep}=-0.6 E_{nuc}=-1.0	4.35(8)	29.2(5)	41
Pulsed with an initial nucleation pulse	E_{dep}=-0.6 E_{nuc}=-1.4	4.33(4)	30.0(5)	36

basal plane). However, this orientation is not obtained in films electrodeposited from CH_2Cl_2 potentiostatically nor by pulsed electrodeposition considering the 015 peak is of highest intensity.

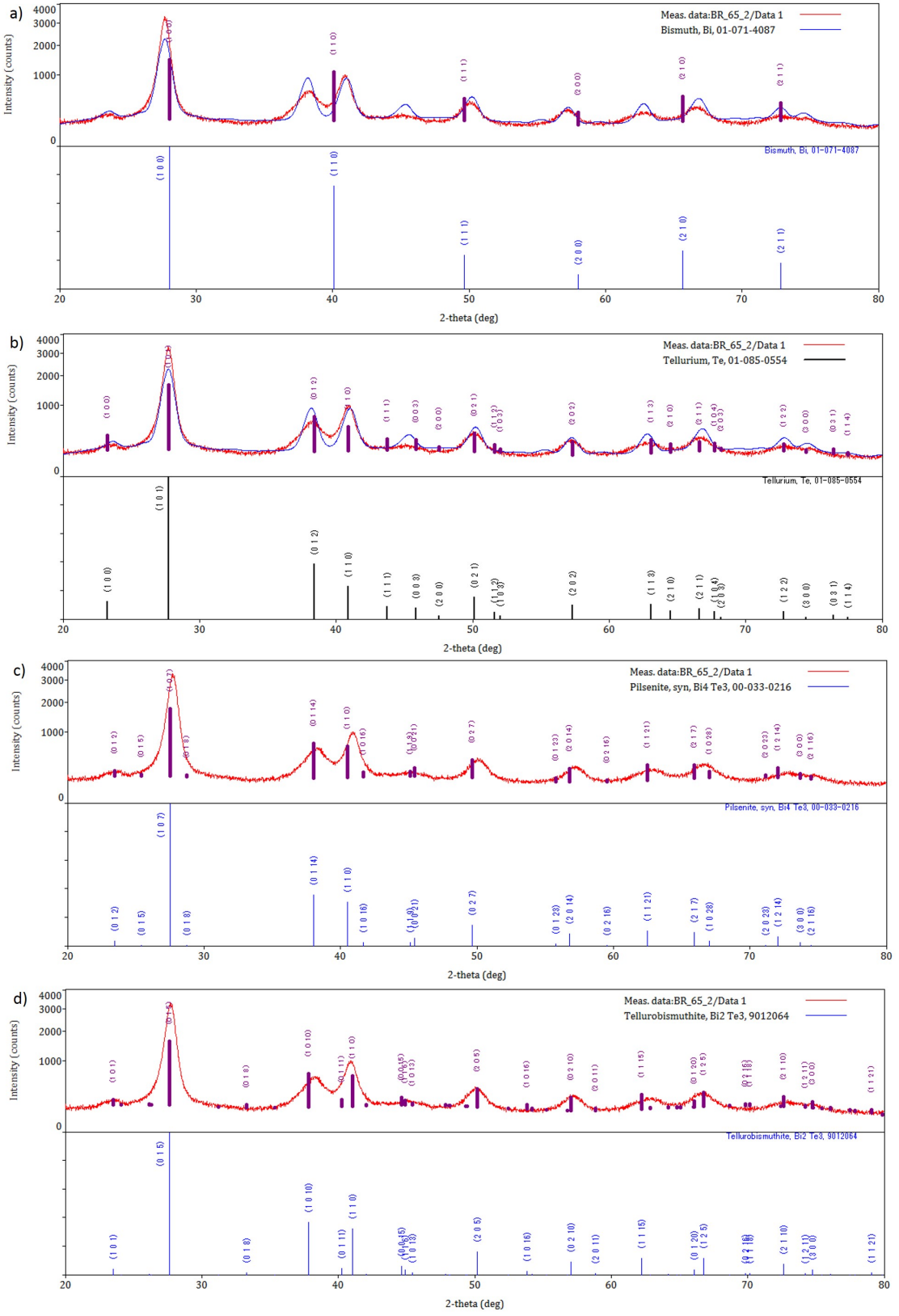

FIGURE 5.13: X-ray diffraction pattern of bismuth telluride thin film electrodeposited by pulsed deposition at -0.6 V preceded by an initial nucleation pulse at -1.0 V vs. Ag/AgCl fitted against a) Bi, b) Te, c) Bi_4Te_3, and d) Bi_2Te_3 literature pattern [42].

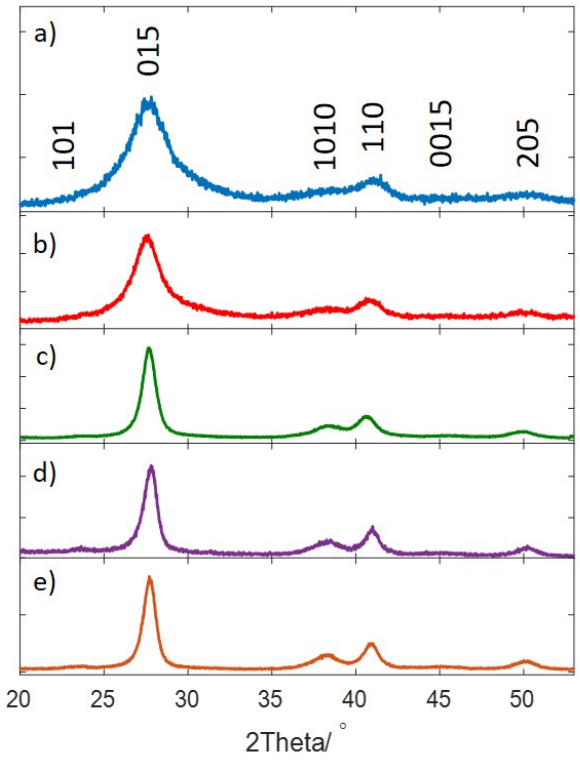

FIGURE 5.14: XRD patterns collected on bismuth telluride films electrodeposited potentiostatically at -1.0 V (a), by pulsed deposition at -1.0 V (b), by pulsed deposition at -0.6 V without an initial nucleation pulse (c) and by pulsed deposition at -0.6 V with an initial nucleation pulse at -1.0 V (d) and -1.4 V (e) vs. Ag/AgCl. t_{on}=5 s and t_{off}=10 s for all pulsed depositions.

5.3.3 XPS spectra

Surface oxidation of electrodeposited bismuth telluride films was investigated by X-ray photoelectron spectroscopy (XPS). XPS measurements were carried out on films electrodeposited by pulsed electrodeposition either with or without an initial nucleation pulse as shown in Fig. 5.15. The samples were taken out of the solution after the deposition and transferred onto an insulating substrate within a couple of days before the measurements were taken. The scans show the Bi 4f and Te 3d doublets. For each sample, the first measurement was taken at the surface layer followed by four cycles of etching with Ar ions for 60 s in order to expose deeper layers in the bulk of the material. The etching rate is approximately 0.5 nm/s, meaning that after each etching cycle measurements were taken 30 nm deeper in the bulk of the material. The reference for XPS spectra analysis is the C 1s peak at a binding energy of 284.8 eV. The Bi $4f_{7/2}$ peak is composed of two contributions at 157.4±0.3 and 158.6±0.4 eV corresponding to Bi in Bi_2Te_3 and Bi in Bi_2O_3, respectively with the associated Bi $4f_{5/2}$ peaks at 162.8±0.3 and 163.9±0.5 eV [111],[112],[113]. The two peaks for Bi-Te and Bi-O are observed due to spin orbital splitting of the f-orbital into $f_{5/2}$ and $f_{7/2}$ components with area ratio of 3/4. In our cases, the free fitted area ratio is 0.79 for both Bi-Te and Bi-O. The Te has contributions of $3d_{5/2}$ at 572.1±0.4 and 575.8±0.5 eV correspond to Bi_2Te_3 and TeO_2, respectively. The contributions of $3d_{3/2}$ are at 582.6±0.4 eV and 586.2±0.5 eV [111],[112],[113]. The free fitted area ratio of the $d_{5/2}$ and $d_{3/2}$ doublet is 0.69, close to the theoretical value of 2/3.

The Bi peaks in films electrodeposited by pulsed electrodeposition show that the Bi_2O_3 peaks have higher intensities than Bi_2Te_3 even in deeper layers of the material, although the Bi_2Te_3 peak intensities increase slightly as deeper layers are exposed (Fig. 5.15a). The more compact and smoother film electrodeposited by pulsed electrodeposition with an initial nucleation pulse at -1.0 V shows a similar trend (Fig. 5.15c). For both films, the Te on the surface is mainly in the form of TeO_2, while after exposure of the deeper layers Te in the form of Bi_2Te_3 is more prominent although a significant contribution from TeO_2 is still present (Fig. 5.15b and d).

In contrast, in the case of the film electrodeposited with an initial nucleation pulse at -1.4 V, there is no Bi at all in the surface layer, and the deeper layers are composed of Bi_2Te_3 with an almost negligible amounts of Bi_2O_3 (Fig. 5.15e). The Te spectra confirm the Bi spectra observation for this film. Here, the surface layer is predominantly Te in the form of TeO_2 with a significant amount of Bi_2Te_3, and the deeper layers are in the form of Bi_2Te_3 with a negligible amount of oxidised Te (Fig. 5.15f). The film possesses Te termination which is mainly oxidised and prevents further oxidation of the underlying film. These data are in full agreement with the EDX data which showed 33.8% and 6.5% of oxygen for the former two films, and 0.3% for the film with the initial nucleation pulse at -1.4 V followed by the pulsed electrodeposition at -0.6 V. Music *et al.*

[114] also observed that Te termination of bismuth telluride slows down the oxidation of Bi_2Te_3. After the last etching cycle, the measurements were taken about 120 nm into the bulk of the material still revealing at least some oxidation in the bulk as a result of oxygen diffusion. Luu *et al.* [115] reported good thermoelectric properties of oxytelluride Bi_2O_2Te, however, in this case the XRD pattern does not match to such structure and it could be that the oxidised surface layer is amorphous as suggested in [114]. Although it was reported that Bi_2Te_3 thin films grown by molecular beam epitaxy are stable and surface oxidation occurs on the time scale of months [116], in the case of porous films the oxidation is significant and can be reduced by decreasing the surface-to-volume ratio and more importantly, by obtaining Te termination on the surface.

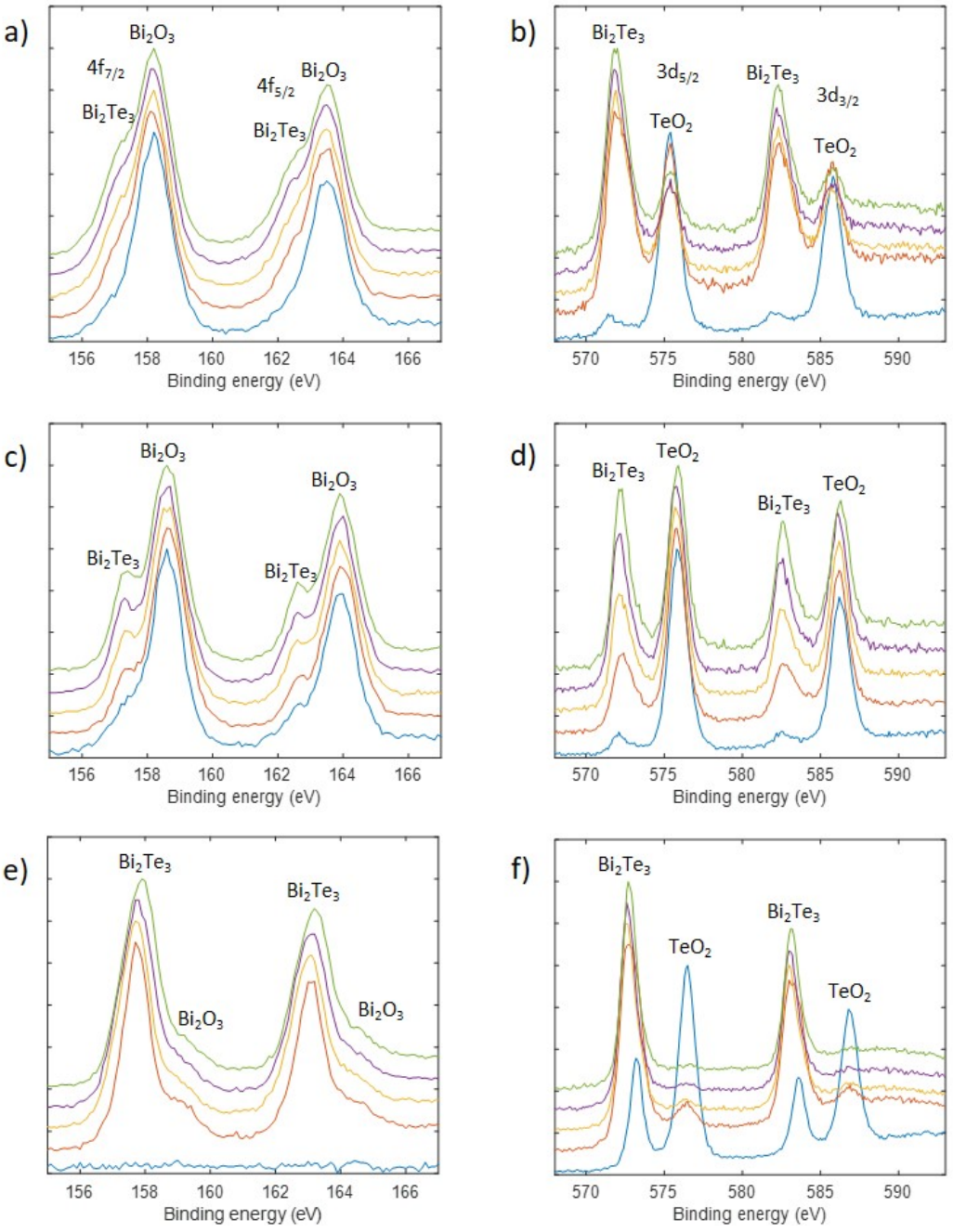

FIGURE 5.15: The Bi 4f (left) and Te 3d (right) regions of the XPS spectra for bismuth telluride films electrodeposited: by pulsed electrodeposition at -1.0 V (a, b), pulsed electrodeposition at -0.6 V preceded by a nucleation pulse at -1.0 V (c, d), a nucleation pulse at -1.4 V (e, f). Blue: surface prior to etching, orange: after 60 s of etching, yellow: after 120 s of etching, purple: after 180 s of etching, and green: after 240 s of etching.

5.4 Characterisation of the films before and after the transfer

The first method of film transfer using PMMA as a carrier polymer resulted in successful lift off of Bi_2Te_3 thin film (Fig. 5.16). The separation of the film from the substrate in KOH solution was successful since KOH is etching the substrate acting on the interface between the film and the substrate while the film is protected with the polymer on top, and therefore facilitating the lift off. However, the removal of the top PMMA layer from Bi_2Te_3 film was unsuccessful in acetone and it resulted in flaking and complete loss of the film into the solution.

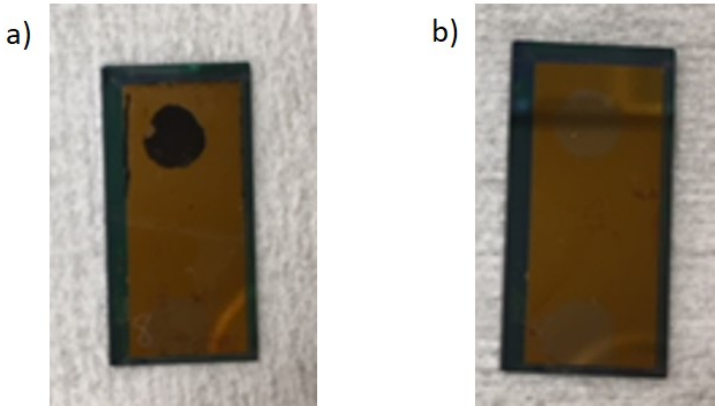

FIGURE 5.16: a) Electrodeposited Bi_2Te_3 thin film on TiN substrate before the transfer with PMMA as a carrier polymer (black spot), b) TiN substrate after the transfer.

The attempt to remove PMMA top layer from Bi_2Te_3 film by oxygen plasma etching was also unsuccessful since the polymer layer on top was still very thick, almost unchanged, after 15 minutes of etching (Fig. 5.17c). The improvement was achieved when PMMA top layer was exposed to UV/ozone for 30 minutes and then dipped into acetone, but still the removal was not complete (Fig.5.18a). Further attempt to remove PMMA was carried out by plasma ashing for 50 minutes (Fig.5.18b), however there was no improvement compared to previous attempt. Lastly, an attempt was made to remove PMMA by dipping the sample into NMP which also resulted in an incomplete removal (Fig.5.18c). The method of film transfer with thermal release tape resulted in separation of the film after it was floated in AZ 400K solution for 90 minutes, but the tape could not be removed from the film after it was transferred onto SiO_2 substrate.

For the last attempt to transfer Bi_2Te_3 thin films, PS was used as a carrier polymer. Figure 5.19 provides photographs of the film on TiN substrate before the transfer (a) and on SiO_2 substrate after the transfer (c). As can be seen from the figure, the film is transferred successfully and the top PS layer was dissolved completely. It was found that thin films ($\leq$550 nm) can be lifted off in water with PS spinned from 9% W/V PS/toluene solution. The separation is enabled due to different materials properties of the TiN substrate and the Bi_2Te_3 film. Namely, TiN is hydrophilic while Bi_2Te_3 and

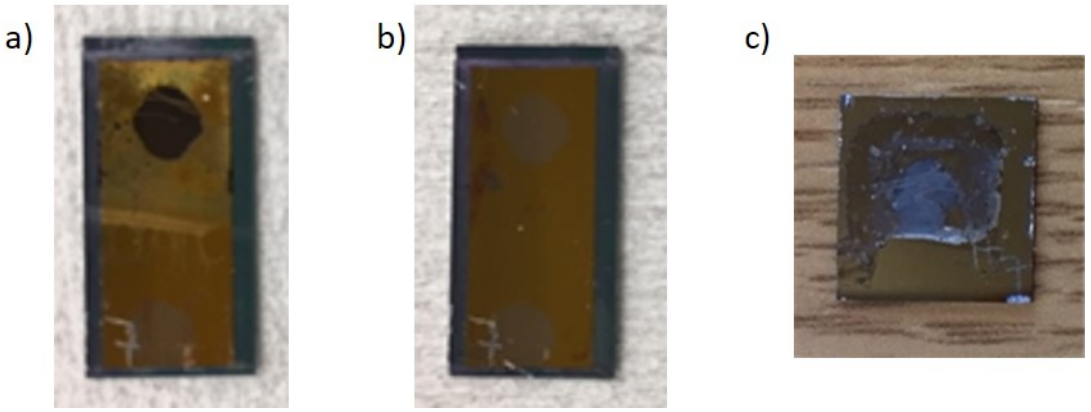

FIGURE 5.17: a) Electrodeposited Bi_2Te_3 thin film on TiN substrate before the transfer with PMMA as a carrier polymer (black spot), b) TiN substrate after the transfer, c) Bi_2Te_3 thin film on thermally grown SiO_2 substrate after the transfer and removal of PMMA by oxygen plasma etching.

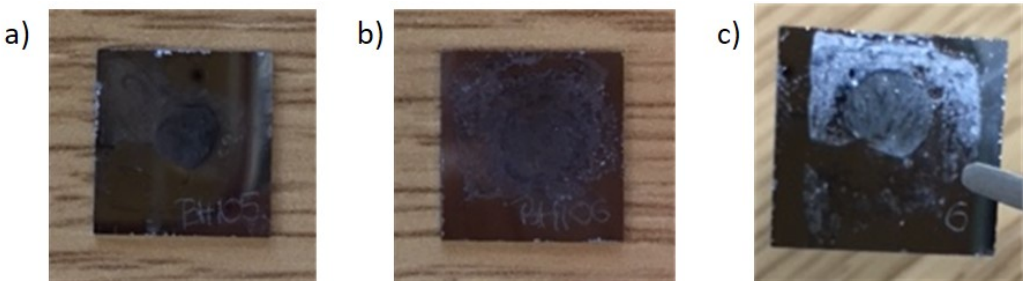

FIGURE 5.18: a) Bi_2Te_3 thin film on thermally grown SiO_2 substrate after the transfer and removal of PMMA by UV/ozone exposure and acetone, b) Bi_2Te_3 thin film on thermally grown SiO_2 substrate after the transfer and removal of PMMA by plasma ashing, c) Bi_2Te_3 thin film on thermally grown SiO_2 substrate after the transfer and removal of PMMA by NMP solution.

PS exhibit hydrophobic nature, which induces dipole water molecules to penetrate into the interface between the substrate and the film coated with polymer and results in separation. For thicker films, the separation was achieved in AZ 400K (2% W/V KOH) solution with PS spinned from 20% W/V PS/toluene solution. The separation was successful in this case because KOH is etching the substrate and acting on the interface between the substrate and the film. Then, the separation is gradually spreading possibly due to capillary wetting. Afterwards, the films were characterised by Optical Microscope, Scanning Electron Microscope (SEM) and Energy Dispersive X-ray Spectroscopy (EDX) before and after the transfer.

Figure 5.20a and b show optical images of Bi_2Te_3 film electrodeposited onto TiN substrate and Bi_2Te_3 film transferred to thermally grown SiO_2 substrate, respectively. Although PS residues are visible on the film after the transfer, the transfer process is complete and the transferred films are uniform without wrinkles or cracks. More PS residues are visible under optical microscope on film transferred onto surface activated by oxygen plasma. Figure 5.20c and d show SEM images of Bi_2Te_3 film before and after the transfer, respectively, also proving there are no cracks in the film after the transfer.

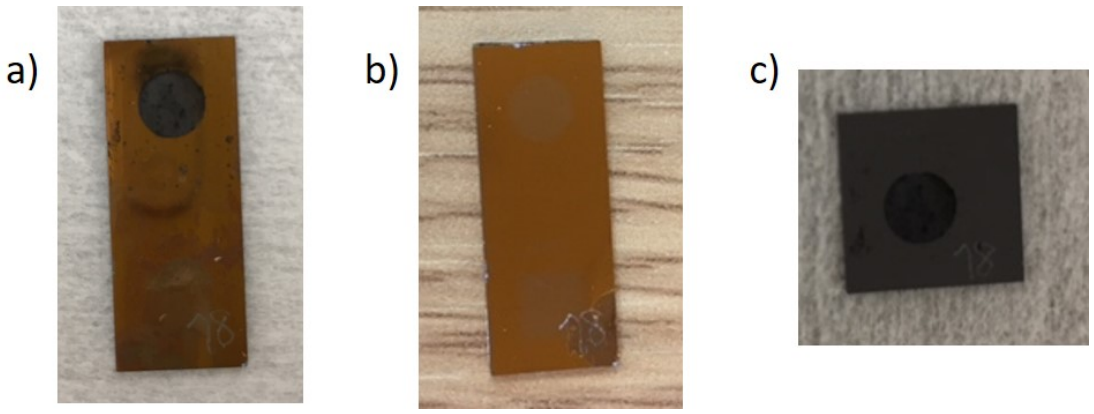

FIGURE 5.19: a) Electrodeposited Bi_2Te_3 thin film on TiN substrate before the transfer (black spot), b) TiN substrate after the transfer, c) Bi_2Te_3 thin film on thermally grown SiO_2 substrate after the transfer.

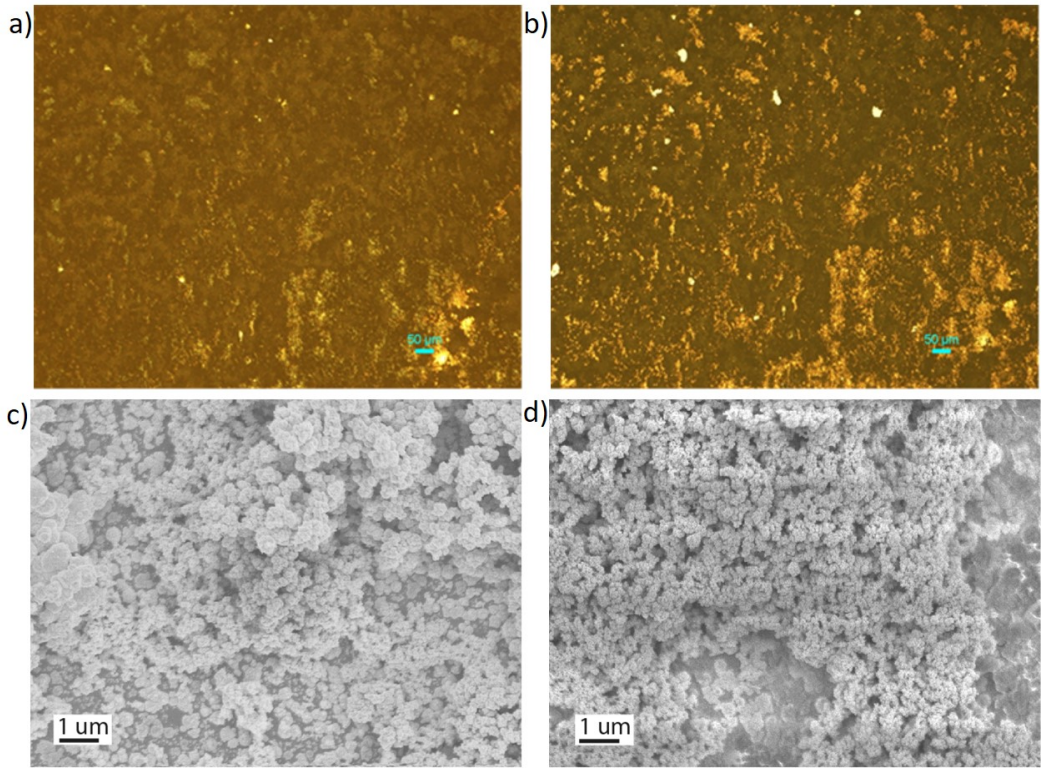

FIGURE 5.20: a) Optical image of Bi_2Te_3 thin film electrodeposited on TiN substrate before the transfer, b) Optical image of Bi_2Te_3 thin film transferred to thermally grown SiO_2 substrate, c) SEM image of Bi_2Te_3 thin film before the transfer, and d) SEM image of Bi_2Te_3 thin film after the transfer.

Activating the target SiO_2 substrate improves the adhesion of transferred films, and no flaking of films was observed while removing PS on top in chloroform after the transfer.

Table 5.5 provides atomic % of Bi and Te of bismuth telluride films electrodeposited potentiostatically at -1 V vs. Ag/AgCl from solution containing 2.5 mM $[N^nBu_4][BiCl_4]$ and 3 mM $[N^nBu_4]_2[TeCl_6]$ with 0.1 M $[N^nBu_4]Cl$ in CH_2Cl_2 before and after being transferred on thermally grown SiO_2, activated fused silica and fused silica substrate. In

TABLE 5.5: Atomic % of Bi and Te before and after the transfer of the films transferred on thermally grown SiO_2, activated fused silica and fused silica substrates.

	Before transfer			After transfer			
Target substrates for transfer	Bi	Te	Bi:Te	Bi	Te	Bi:Te	average Bi:Te ± stdev
Thermally grown SiO_2 substrate	14.9	23.4	**0.64**	11.3	19.0	**0.59**	0.62±0.04
Activated fused silica substrate	14.2	17.9	**0.79**	15.9	20.1	**0.79**	0.79±0.00
Fused silica substrate	14.4	35.2	**0.41**	10.4	19.8	**0.53**	0.47±0.08

the case of film transferred onto activated fused silica substrate, Bi:Te ratio is the same, while films transferred onto thermally grown SiO_2 and fused silica substrate show close values (standard deviation $\leqslant$0.08), proving the integrity of transfer process. Differences in Bi:Te ratios before and after the transfer are possibly because the chosen area for EDX spectrum is not the same, and not due to the loss of elements during the transfer process.

Fig 5.21, 5.22 and 5.23 provide EDX spectra of bismuth telluride thin films electrodeposited potentiostatically at -1 V vs. Ag/AgCl from solution containing 2.5 mM $[N^nBu_4][BiCl_4]$ and 3 mM $[N^nBu_4]_2[TeCl_6]$ with 0.1 M $[N^nBu_4]Cl$ in CH_2Cl_2 before (blue) and after (orange) the transfer. Fig. 5.21 shows that the signal intensities of Bi and Te before (blue) and after the transfer (orange) are close but the O signal is slightly higher. Also, the Si signal is significantly higher on the film after the transfer compared to the signal before the transfer, and the O signal could arise from SiO_2 in the substrate. Fig. 5.22 shows almost the same signal intensities of Bi, Te and O before (blue) and after the transfer (orange). However, the Si signal is higher is film before than after the transfer. On the Fig. 5.23 the Te signal is somewhat higher in the film before the transfer in comparison to after the transfer, but the Bi and O signal intensities are very close. In this case, there is no Si signal in spectra both before and after the transfer. Considering the same intensities in O before and after the transfer it can be concluded that O signal comes from oxidised Bi_2Te_3 surface. Moreover, this also shows that transfer process does not oxidise the films after the transfer considering that the aqueous solution is used to delaminate films from TiN electrodes they were grown on. The differences in signals are possibly coming from different area chosen for EDX measurements before and after the transfer.

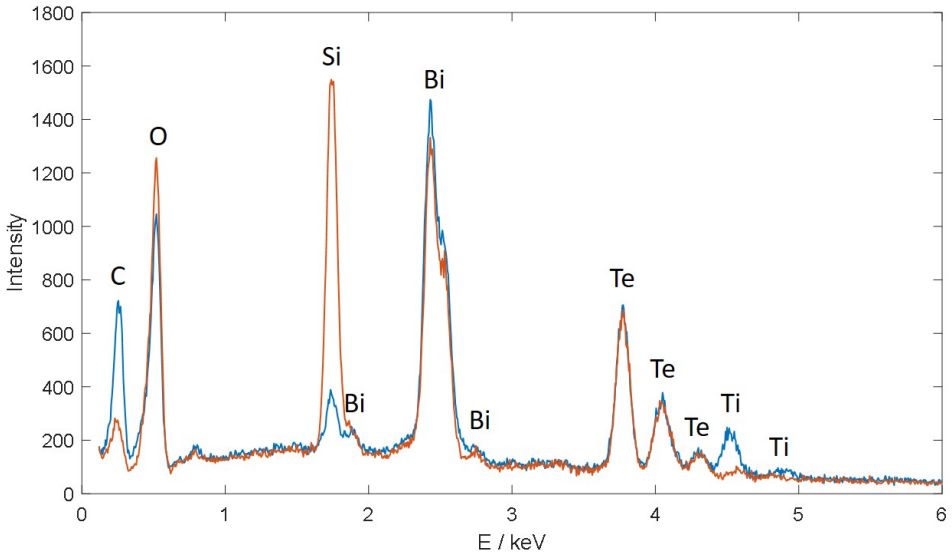

FIGURE 5.21: EDX spectra collected on Bi_2Te_3 film electrodeposited potentiostatically at -1 V vs. Ag/AgCl before and after the transfer onto thermally grown SiO_2 substrate. Blue: before transfer, orange: after transfer.

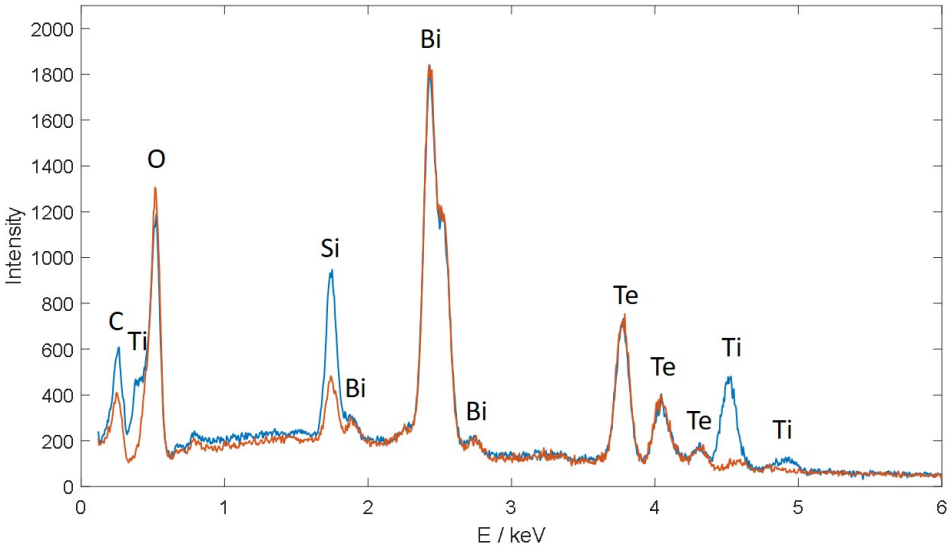

FIGURE 5.22: EDX spectra collected on Bi_2Te_3 film electrodeposited potentiostatically at -1 V vs. Ag/AgCl before and after the transfer onto activated fused silica substrate. Blue: before transfer, orange: after transfer.

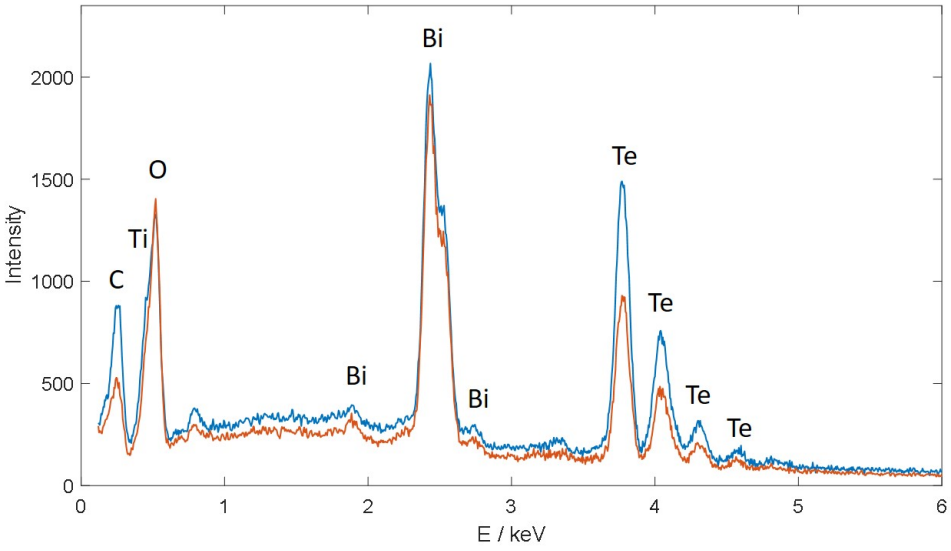

FIGURE 5.23: EDX spectra collected on Bi_2Te_3 film electrodeposited potentiostatically at -1 V vs. Ag/AgCl before and after the transfer onto fused silica substrate. Blue: before transfer, orange: after transfer.

5.5 Thermoelectric characterisation of the transferred film

Thermoelectric characterisation was conducted on the film electrodeposited by pulsed electrodeposition at -0.6 V vs. Ag/AgCl for on-time 5 s and off-time 10 s with an initial nucleation pulse of -1.0 V vs. Ag/AgCl for 5 s after the transfer to an insulating SiO_2 substrate. The electrodeposited film is n-type with a charge carrier concentration of (2.8±1.2) $\times 10^{20}$ cm^{-3}, resistivity of 15.9 mΩ cm and mobility of (0.92±0.13) cm^2/V s at room temperature obtained from Hall measurements. The resistivity decreases with increasing temperature (Fig. 5.24a), meaning that the electrodeposited bismuth telluride film exhibits semiconducting behaviour with further thermal activation at higher temperature. The film exhibits a Seebeck coefficient of -51.7 μV/K at 300 K, which increases with temperature reaching a value of -96.6 μV/K at 520 K (Fig 5.24a). The decrease in Seebeck coefficient after 520 K is due to the bipolar effect. At the temperature of ∼500 K electrons from the valence band are elevated into the conduction band. This gives rise to minority carriers (in this case holes), travelling in the opposite direction. The two types of carriers have opposite signs of Seebeck coefficient cancelling each other, and therefore decreasing the material's Seebeck coefficient with further temperature increment. The power factor is defined as $S^2\sigma$ meaning that it depends only on the Seebeck coefficient and the electrical conductivity of the material. Fig. 5.24b shows the power factor of the thin film as a function of temperature, showing that the power factor increases with increasing temperature reaching a value of 88.2 μW/ m K^2 at 520 K, in accordance with the increase in Seebeck coefficient. The porous films obtained potentiostatically or by pulsed electrodeposition are insulating probably due to oxidation of the films as a result of high surface-to-volume ratio, and no Seebeck or resistivity data could be extracted. There is a range of values for Seebeck coefficient and resistivity of electrodeposited bismuth telluride thin films reported in literature. However, we compare our data to that from the Martin-Gonzalez group [18],[16],[78] who have carried out an extensive study on electrodeposition of bismuth telluride thin films from an aqueous solution. The obtained carrier concentration and the Seebeck coefficient values of our electrodeposited bismuth telluride films are close to the reported data, however the resistivity value is higher than the reported ones. Manzano et al. [16] reported carrier concentration of 3.2×10^{20} cm^{-3} and Seebeck coefficient of -58 μV/K, which correspond to our measured values of $(2.8\pm1.2)\times10^{20}$ cm^{-3} for carrier concentration and -51.7 μV/K for Seebeck coefficient. The reported resistivity is 1.5 mΩ cm, lower than our measured value of 15.9 mΩ cm. Comparing to films electrodepsited from non-aqueous solutions, Szymczak et al. [23] reported thermoelectric measurements on Bi_2Te_3 films electrodeposited from piperidinium ionic liquid binary mixture. The reported resistivity of 133 $\mu\Omega$ m is as well higher than that of the films electrodeposited from aqueous solutions, and comparable to that of films electrodeposited from dichloromethane (15.9 mΩ cm). The reported Seebeck coefficient is somewhat higher (-70 μV/K) and the carrier concentration of 1.21×10^{20} cm^{-3} close to the value measured on the film electrodeposited from

dichloromethane (-51.7 μV/K and (2.8±1.2)×10^{20}, respectively). More results on reproducibilty of thermoelectric measurements of Bi_2Te_3 films electrodeposited from CH_2Cl_2 can be found in Appendix 7.1.

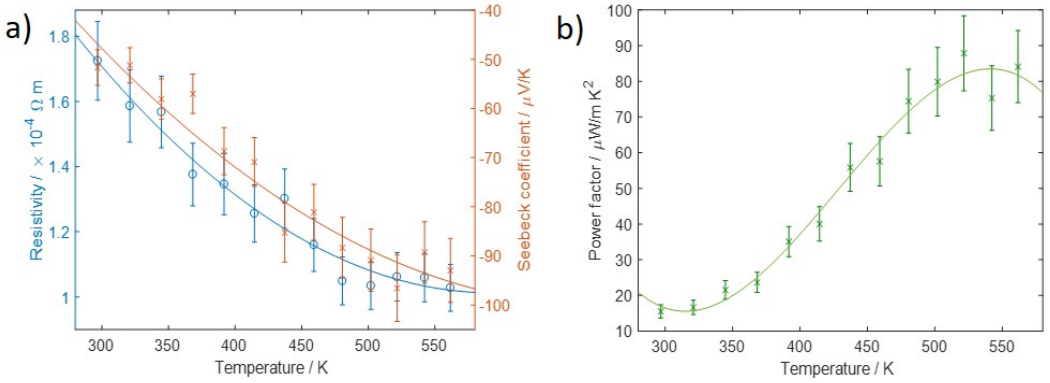

FIGURE 5.24: Dependence of a) resistivity and Seebeck coefficient, and b) power factor with temperature for bismuth telluride film electrodeposited by pulsed electrodeposition at -0.6 V vs. Ag/AgCl for on-time 5 s and off-time 10 s with an initial nucleation pulse to -1 V vs. Ag/AgCl for 5 s. Error bars are based on tool manufacturers information. Lines are guides to the eye.

5.6 Summary

Bismuth telluride thin films were electrodeposited from electrolyte containing $[N^nBu_4][BiCl_4]$ and $[N^nBu_4]_2[TeCl_6]$ as Bi and Te precursors, respectively, and $[N^nBu_4]Cl$ as supporting electrolyte dissolved in dichloromethane (CH_2Cl_2). Potentiostatic and pulsed electrodeposition achieved either discontinuous or porous films. However films obtained by pulsed electrodeposition possessed improved composition repeatability between replicate samples and somewhat denser morphologies compared to those deposited potentiostatically. The conditions for pulsed electrodeposition were optimised to 5 s on-time and 10 s off-time. In order to further improve the film's morphology, an initial nucleation pulse at higher overpotential was introduced after which the films were grown at lower overpotential either potentiostatically or by pulsed electrodeposition. The conditions were optimised to potential of -0.6 V vs. Ag/AgCl for the film growth potentiostatically or by pulsed electrodeposition (t_{on}=5 s, t_{off}=10 s), preceded by a nucleation of either -1.0 or -1.4 V vs. Ag/AgCl for 5 s. The films grown potentiostatically at lower overpotential preceded by a nucleation pulse at higher overpotential were discontinuous, while those grown by pulsed electrodeposition at lower overpotential preceded by a nucleation pulse at higher overpotential were compact, continuous and smooth. EDX compositional analysis showed the presence of Bi and Te signals indicating bismuth telluride compound, and the XRD patterns confirmed deposition of trigonal Bi_2Te_3 compound. The crystallite sizes calculated from peak widths in XRD patterns showed that the films deposited by pulsed electrodeposition at lower overpotential of -0.6 V vs. Ag/AgCl possess bigger crystallites than those deposited at higher overpotential of -1.0 V vs. Ag/AgCl due to the lower nucleation rate at lower potential. Furthermore, the films deposited by pulsed electrodeposition at -0.6 V vs. Ag/AgCl either with or without an initial nucleation pulse possess the same crystallite size. XPS measurements showed that the oxidation of porous films is significant, probably due to the high surface-to-volume ratio of these films. In addition, the high oxygen amount was observed by EDX compositional analysis as well. The oxidation of compact and smooth films obtained by pulsed electrodeposition at lower overpotential preceded by a nucleation pulse at higher overpotential was remarkably reduced, which is confirmed by both XPS and EDX measurements. More notably, it was shown that if the smooth Bi_2Te_3 film possesses Te termination, there is only surface oxidation of Te protecting the bulk from oxygen diffusion and further oxidation. In order to perform electric measurements, the films were transferred from conductive TiN electrode to the insulating SiO_2 substrate using polystyrene as the carrier polymer. The thermo-electric characterisation was carried out on Bi_2Te_3 film obtained by pulsed electrodeposition at -0.6 V vs. Ag/AgCl (t_{on}=5 s, t_{off}=10 s) preceded by a nucleation pulse at -1.0 V vs. Ag/AgCl for 5 s. Hall measurements showed that the film is n-type with a charge carrier concentration of $(2.8\pm1.2) \times 10^{20}$ cm^{-3} and resistivity of 15.9 mΩ cm at room temperature. Temperature dependent resistivity measurements showed that the resistivity decreases with increasing temperature, meaning that the electrodeposited

bismuth telluride film exhibits semiconducting behaviour. The film possessed a Seebeck coefficient of -51.7 μV/K at 300 K, which increases with temperature reaching a value of -96.6 μV/K at 520 K. The decrease of Seebeck coefficient with the further temperature increase is due to the bipolar effect. The power factor increased in line with the Seebeck coefficient increase, reaching a value of 88.2 μW/ m K^2 at 520 K.

Chapter 6

Thermoelectric Properties of Antimony Telluride Thin Films Electrodeposited from Dichloromethane

6.1 Electrodeposition of antimony telluride thin films from dichloromethane

To explore electrochemistry of individual precursors, cyclic voltammetry experiments were carried out on $[N^nBu_4][SbCl_4]$ and $[N^nBu_4]_2[TeCl_6]$ in CH_2Cl_2.

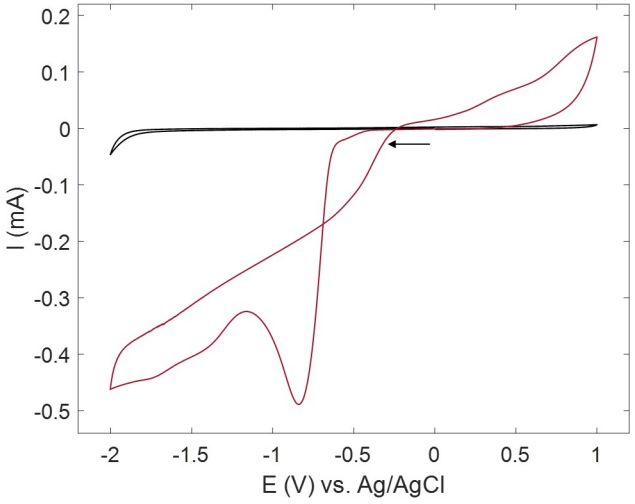

FIGURE 6.1: First cyclic voltammogram of 2 mM $[N^nBu_4][SbCl_4]$ in CH_2Cl_2 solution containing 0.1 M $[N^nBu_4]Cl$ supporting electrolyte CH_2Cl_2 on TiN electrode. Black: scan in 0.1 M $[N^nBu_4]Cl$ supporting electrolyte. Scan rate 50 mV s^{-1}.

Fig. 6.1 shows voltammetry for reduction of $[N^nBu_4][SbCl_4]$ on TiN electrode (red) scanning negatively from 1 V to -2 V and back to 1 V, and the background scan in 0.1 M $[N^nBu_4]Cl$ supporting electrolyte. On the cathodic scan, there an increase in current for the reduction of $[SbCl_4]^-$ starting at *ca.* -0.4 V vs. Ag/AgCl with a reduction peak at -0.8 V and a nucleation loop on the return scan. The peak at -0.8 V is attributed to reduction of Sb^{3+} to Sb(0) by the work previously done in our group (see Appendix 7.1). Scanning positively, an increase in current is observed starting at -0.2 V with a small stripping wave at *ca.* 0.4 V. The total charge passed for the reduction of $[SbCl_4]^-$ (10.7 mC) is much higher than the charge for the oxidation (1.5 mC), meaning that the material electrodeposited onto working electrode is not completely oxidised. Cyclic voltammetry of $[N^nBu_4]_2[TeCl_6]$ precursor on TiN is presented in Section 5.1.

Prior to antimony telluride electrodeposition, cyclic voltammetry was carried out in the electrolyte solution containing 2 mM $[N^nBu_4][SbCl_4]$ and 3 mM $[N^nBu_4]_2[TeCl_6]$ in CH_2Cl_2 containing 0.1 M $[N^nBu_4]Cl$ supporting electrolyte to investigate the electrodeposition conditions of antimony telluride. Figure 6.2a shows three consecutive voltammograms on glassy carbon (GC) working electrode scanning negatively from 1 V to -2 V and back to 1 V. Scanning negatively from 0 to -2 V in the first scan (blue curve), two reduction peaks at 0.47 and -1.05 V vs. Ag/AgCl are noticeable. The charge for the reduction peaks is calculated to be 2.9 mC. In the anodic scan, the current increase starts at 0 V vs. Ag/AgCl, with two waves at 0.40 V and 0.55 V. The charge calculated for oxidation peaks is 0.95 mC which is 31% of reduction charge value, indicating that the deposited material is not completely oxidised. For the second and third cathodic scan (red and green curve, respectively) reduction peaks are at -0.5 V and -1.0 V, slightly shifted with respect to the first scan. On the return scan, the two oxidation waves are at 0.3 V and 0.5 V. The change in voltammetry for reduction and oxidative stripping in the second and third scan is due to the modified electrode surface as the material is not fully oxidised after the first scan resulting in facilitated deposition onto already deposited material. The black curve shows voltammetry in $[N^nBu_4]Cl$ supporting electrolyte. Figure 6.2b shows three consecutive voltammograms on titanium nitride (TiN) working electrode scanning negatively from 1 V to -2 V and back to 1 V. Scanning negatively in the first scan (blue curve), a small increase in cathodic current can be seen at *ca.* 0.2 V (see inset in 6.2b), similar to the one observed for reduction of 2 mM $[N^nBu_4][BiCl_4]$ and 3 mM $[N^nBu_4]_2[TeCl_6]$ attributed to reduction of $[TeCl_6]^{2-}$ to Te(0) (see Fig. 5.1b). Scanning further negatively, one reduction peak at *ca.*-0.8 V can be seen, similar to the peak observed in reduction of 2 mM $[N^nBu_4][SbCl_4]$ (Fig. 6.1) attributed to reduction of Sb^{3+} to Sb(0). The total passed charge under reduction peak is 18.8 mC. Scanning positively from -2 to 1 V in the first scan, there is a broad oxidation peak starting at 0 V with the two waves at 0.4 and 0.7 V. The calculated charge for the oxidation is 6.8 mC, 36% of reduction charge indicating here as well that the deposited material is not fully oxidised. In the cathodic scan for the second and third scan, there are peaks at -0.9 V and -1.2 V, and one peak in the anodic scan at 0.7 V. The second and third

scan (red and green curve, respectively) differ from the first scan, as the material is not completely oxidised after the first scan facilitating the deposition in the second and third scan. The black curve represents voltammetry in $[N^nBu_4]Cl$ supporting electrolyte. As the electrodeposition of antimony telluride is carried out on TiN working electrode, the deposition potentials are chosen considering positions of reduction peaks in cyclic voltammetry on TiN. The chosen potentials for electrodeposition experiments of Sb_2Te_3 are: -0.80, -0.95, -1.10, -1.25, -1.40, -1.55 and -1.70 V vs. Ag/AgCl.

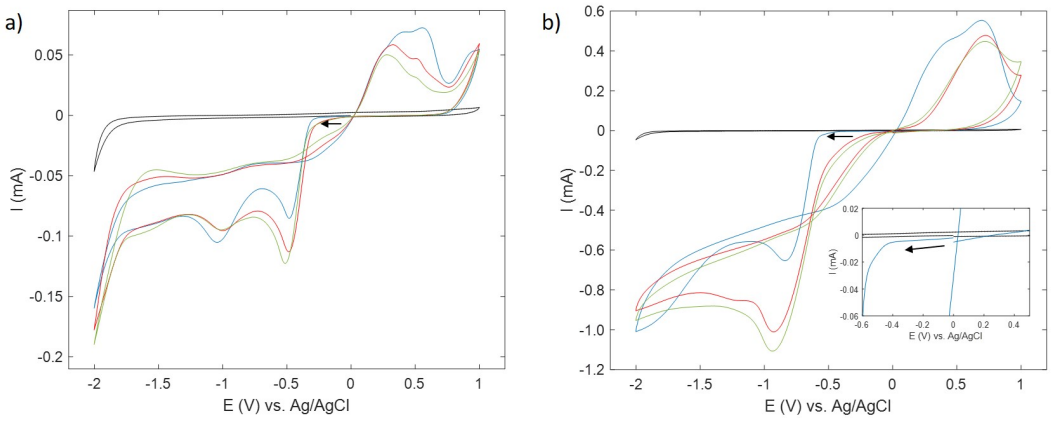

FIGURE 6.2: Three consecutive cyclic voltammograms of 2 mM $[N^nBu_4][SbCl_4]$, 3 mM $[N^nBu_4]_2[TeCl_6]$ in CH_2Cl_2 solution containing 0.1 M $[N^nBu_4]Cl$ supporting electrolyte CH_2Cl_2 on a) 3 mm diameter GC electrode, and b) 7×11 mm TiN electrode. Blue: 1^{st}, red: 2^{nd}, green: 3^{rd} scan. Black: scan in supporting electrolyte. Scan rate 50 mV s^{-1}.

6.2 Characterisation of as-deposited films

6.2.1 SEM images and EDX spectra

Figure 6.3 shows SEM images of Sb_2Te_3 thin films electrodeposited potentiostatically at various potentials to nominal thickness of 500 nm based on the passed charge of -0.7 C. As can be seen on the figure, all the films exhibit porous morphologies, and the discontinuity increases by increasing the deposition potential.

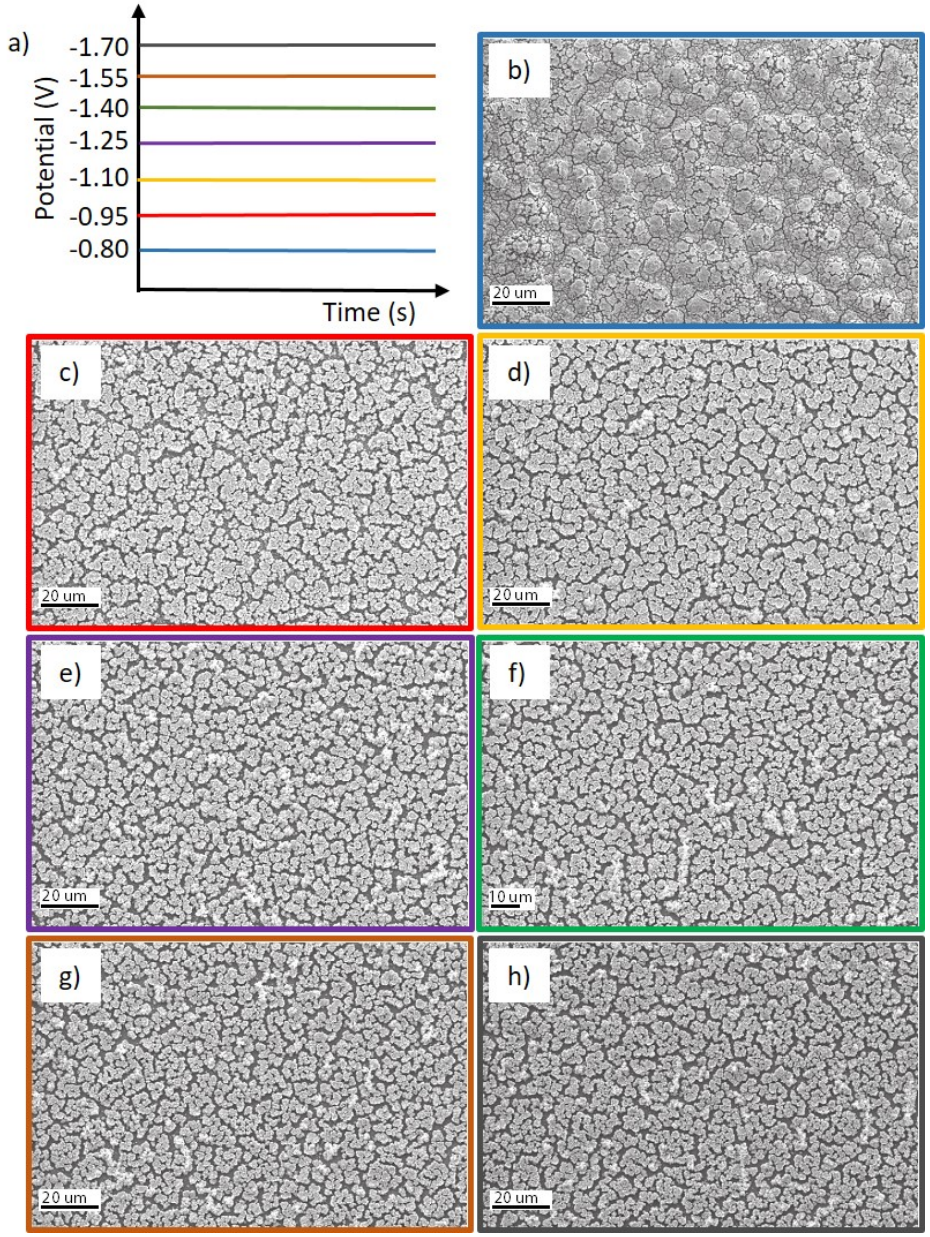

FIGURE 6.3: Schematic and SEM images of Sb_2Te_3 electrodepsoted from 2 mM $[N^nBu_4][SbCl_4]$, 3 mM $[N^nBu_4]_2[TeCl_6]$ in CH_2Cl_2 solution containing 0.1 M $[N^nBu_4]Cl$ supporting electrolyte CH_2Cl_2 potentiostatically at: -0.80 (b), -0.95 (c), -1.10 (d), -1.25 (e), -1.40 (f), -1.55 (g), and -1.70 (h) V vs. Ag/AgCl.

TABLE 6.1: Elemental composition showing atomic percentage of each element measured on three different areas of the film. All films are electrodeposited potentiostatically from an electrolyte containing 2 mM $[N^nBu_4][SbCl_4]$, 3 mM $[N^nBu_4]_2[TeCl_6]$ and 0.1 M $[N^nBu_4]Cl$ in CH_2Cl_2.

	Atomic %							
E_{dep} / V vs. Ag/AgCl	Sb	Te	O	C	Si	Ti	Sb/Te	Average Sb/Te ± stdev
-0.80	23.6	35.1	9.4	11.3	6.8	14.0	0.7	0.8±0.10
	27.6	33.6	9.3	10.3	5.8	12.4	0.8	
	27.1	31.2	9.5	11.5	6.8	12.8	0.9	
-0.95	24.1	39.5	6.1	10.9	6.2	13.2	0.6	0.6±0.02
	24.7	40.6	6.1	9.3	5.2	13.7	0.6	
	25.3	39.5	7.6	10.8	4.6	17.2	0.6	
-1.10	23.6	33.3	6.6	10.1	8.6	17.2	0.7	0.7±0.02
	25.3	34.2	7.1	11.3	7.1	14.5	0.7	
	26.8	35.4	8.4	12.4	5.0	11.3	0.8	
-1.25	21.9	29.5	7.8	11.0	10.2	18.9	0.7	0.8±0.01
	20.7	27.4	7.9	10.3	12.1	21.3	0.8	
	24.0	32.5	7.8	11.2	8.1	15.7	0.7	
-1.40	19.5	27.2	9.4	8.2	13.1	22.3	0.7	0.7±0.03
	19.8	27.9	9.6	10.4	10.9	20.8	0.7	
	22.7	29.6	10.1	12.4	8.0	16.4	0.8	
-1.55	15.3	23.6	6.2	9.7	17.1	28.2	0.7	0.7±0.04
	19.6	30.4	6.6	11.7	11.3	19.8	0.7	
	22.9	32.0	7.6	13.0	7.9	16.0	0.7	
-1.70	16.8	24.1	6.2	10.0	16.1	26.4	0.7	0.7±0.02
	20.8	29.7	6.7	11.1	10.9	20.4	0.7	
	23.1	31.8	6.4	17.2	7.4	13.4	0.7	

Table 6.1 provides EDX elemental composition measured on three different areas on each film. The films consist of the following elements: Sb, Te, O, Si, Ti, and C. The presence of Sb and Te indicates either the deposition of antimony telluride or elemntal Sb and Te. The presence of Si and Ti signals come from SiO_2 and TiN in the substrate, respectively. C signal comes from adventitious carbon contamination on the surface. O signal could come from both SiO_2 in the substrate and oxidation of Sb_2Te_3. Small standard deviations ($\leqslant$0.10) in Sb to Te ratios in all films regardless of the deposition potential show excellent uniformity of deposits over the given area. The Sb to Te ratios change slightly with different applied potential, hence it can be concluded that the deposition potential does not affect the stoichiometry as in the case of Bi_2Te_3 electrodeposition.

In order to achieve denser and smoother films needed for thermoelectric purpose, pulsed electrodeposition was employed as in the case of Bi_2Te_3 electrodeposition. Also, the concentration of $[N^nBu_4][SbCl_4]$ precursor was decreased from 2 to 1.75 mM which gave stoichiometric composition at pulsed conditions. Figure 6.4 shows SEM images of Sb_2Te_3 films electrodeposited by pulsed electrodeposition with on-time=5 s and off-time=10 s, at deposition potentials at -0.80 V (6.4b) and -0.95 V (6.4c) vs. Ag/AgCl. Nominal

thickness of the electrodeposited films electrodeposited is calculated to be 500 nm based on the passed charge of -0.7 C. As can be seen in the figure, the film obtained by pulsed electrodeposition at -0.80 V vs. Ag/AgCl is compact, continuous and smooth, while film deposited at -0.95 V vs. Ag/AgCl is porous. Hence, the film deposited by pulsed deposition at -0.80 V vs. Ag/AgCl was further investigated for its thermoelectric properties. The as-deposited film exhibits poor cristallinity, and was post-annealed at 100°C for 30 minutes. Figure 6.5 shows SEM images of as deposited film obtained by pulsed electrodeposition (t_{on}=5s, t_{off}=10 s) at -0.80 V V vs. Ag/AgCl (6.5a), and the same film after post-annealing (6.5b). As can be seen on the figure, the film's morphology is unchanged after annealing. Table 6.2 provides EDX elemental analysis of films as deposited and post-annealed Sb_2Te_3 at -0.80 V vs. Ag/AgCl by pulsed pulsed electrodeposition, and as-deposited at -0.95 V vs. Ag/AgCl. The elemental analysis shows signals of Sb and Te in stoichiometric ratio (0.7) for as-deposited film at -0.80 V vs. Ag/AgCl, staying unchanged after annealing. In addition, Si and Te signals coming from the substrate, and O signals likely coming from oxidised Sb_2Te_3 are lower compared to the films obtained potentiostatically, indicating as well denser and smoother films.

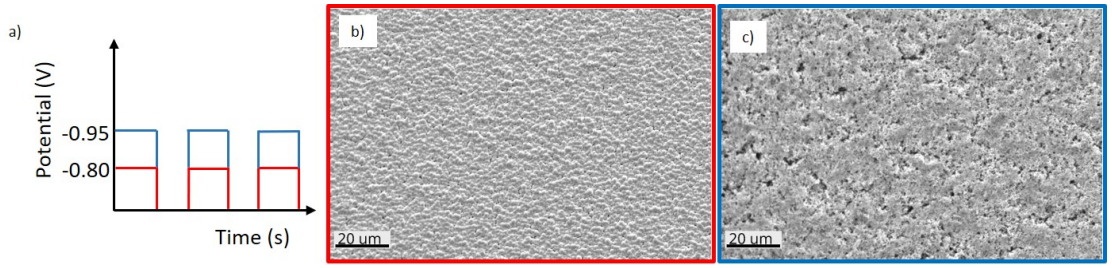

FIGURE 6.4: Schematic and SEM images of Sb_2Te_3 electrodepsoted from 1.75 mM $[N^nBu_4][SbCl_4]$, 3 mM $[N^nBu_4]_2[TeCl_6]$ in CH_2Cl_2 solution containing 0.1 M $[N^nBu_4]Cl$ supporting electrolyte CH_2Cl_2 by pulsed electrodeposition (t_{on}=5s, t_{off}=10 s) at: -0.80 (b) and -0.95 (c) V vs. Ag/AgCl.

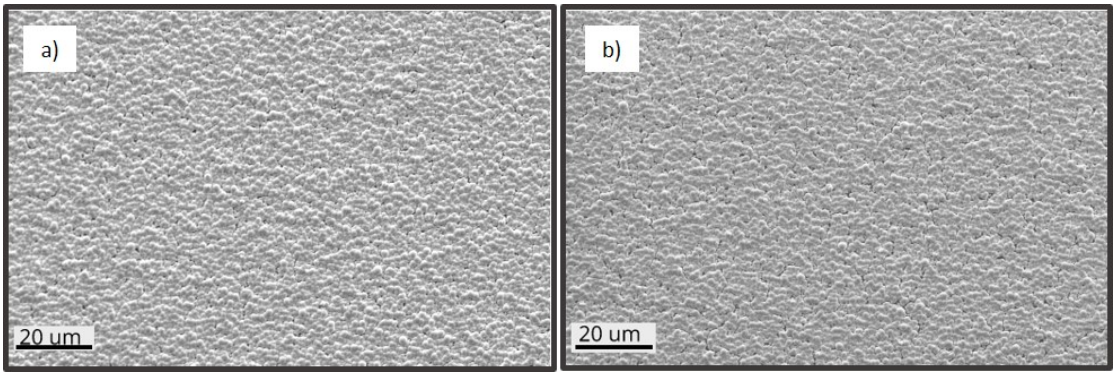

FIGURE 6.5: SEM images of Sb_2Te_3 electrodepsoted from 1.75 mM $[N^nBu_4][SbCl_4]$, 3 mM $[N^nBu_4]_2[TeCl_6]$ in CH_2Cl_2 solution containing 0.1 M $[N^nBu_4]Cl$ supporting electrolyte CH_2Cl_2 by pulsed electrodeposition (t_{on}=5s, t_{off}=10 s) at -0.80 V vs. Ag/AgCl, as-deposited (a), and annealed at 100 °C for 30 minutes (b).

Volykhov et al. [117] investigated oxidation of Sb_2Te_3 single crystals grown by the Bridgman method. It was found that Sb_2Te_3 oxidises much faster than Bi_2Te_3, in humid

TABLE 6.2: Elemental composition showing atomic percentage of each element measured on three different areas of the film. All films are deposited by pulsed electrodeposition (t_{on}=5s, t_{off}=10 s) from an electrolyte containing 1.75 mM $[N^nBu_4][SbCl_4]$, 3 mM $[N^nBu_4]_2[TeCl_6]$ and 0.1 M $[N^nBu_4]Cl$ in CH_2Cl_2.

E_{dep} / V vs. Ag/AgCl	Sb	Te	O	C	Si	Ti	Sb/Te	Average Sb/Te ±stdev
-0.80	32.5	49.9	2.0	5.3	2.8	7.0	0.7	0.7±0.01
	34.5	52.1	1.1	3.5	2.6	5.6	0.7	
	35.5	52.7	1.4	6.6	1.2	2.8	0.7	
-0.80 (after annealing)	33.5	49.5	1.6	3.8	3.4	7.7	0.7	0.7±0.01
	34.3	49.5	2.4	4.3	3.0	6.0	0.7	
	35.3	51.9	2.0	3.4	2.3	4.4	0.7	
-0.95	28.5	59.8	2.6	6.3	0.8	1.6	0.5	0.5±0.03
	27.5	63.2	2.1	5.3	0.6	1.0	0.4	
	27.5	63.7	2.9	4.3	0.7	0.6	0.4	

air on a scale of minutes to hours. The smooth antimony telluride film electrodeposited from dichloromethane possessed oxygen content of 4.2 atomic %, jumping to 17.9 atomic % after 6 weeks of exposure to air. This as well shows that Sb_2Te_3 is very prone to oxidation, and Te termination here as well might slow down this process.

6.2.2 X-ray diffractograms

Figure 6.6 shows X-ray diffraction pattern of antimony telluride thin film electrodeposited by pulsed electrodeposition from dichloromethane and post-annealed fitted against literature patterns [42]. As can be seen from the figure, the diffraction pattern does not agree well with elemental Bi (6.6a) nor elemental Te (6.6b), but does agree with Sb_2Te_3 literature pattern (6.6c). Moreover, EDX elemental analysis of antimony telluride thin film electrodeposited by pulsed electrodeposition at -0.8 V vs. Ag/AgCl (t_{on}=5s, t_{off}=10 s) from dichloromethane showed both Sb and Te are present in close Sb_2Te_3 stoichiometric ratio (0.7). The peaks are therefore attributed to trigonal Sb_2Te_3.

Figure 6.7 shows the diffraction patterns of antimony telluride films electrodeposited onto TiN electrodes potentiostatically (blue), as-desposited by pulsed electrodeposition (green), and post-annealed after pulsed electrodeposition (red) at -0.8 V vs. Ag/AgCl. The X-ray diffraction analysis of as-deposited antimony telluride thin films obtained potentiostatically and by pulsed electrodeposition show poor crystallinity with only broad 015 peak which can be observed (6.7 blue and green). However, by post-annealing the film deposited by pulsed electrodeposition, polycrystalline Sb_2Te_3 is obtained (6.7 red). The post annealing was carried out in nitrogen at 100°C for 30 minutes. There are peaks at 2Θ angles of 28.16°, 33.56°, 37.30°, 38.20°, 41.03°and 42.28°, 44.47°, 45.84°, 50.45°, 51.61°, 53.69°, 53.98°, 54.35°, 58.39°, 62.97°, 66.81°, 68.94°, 70.73°, 74.78°and 77.73°. The 015 reflection at 28.16°is of the highest intensity for all the films, and its width

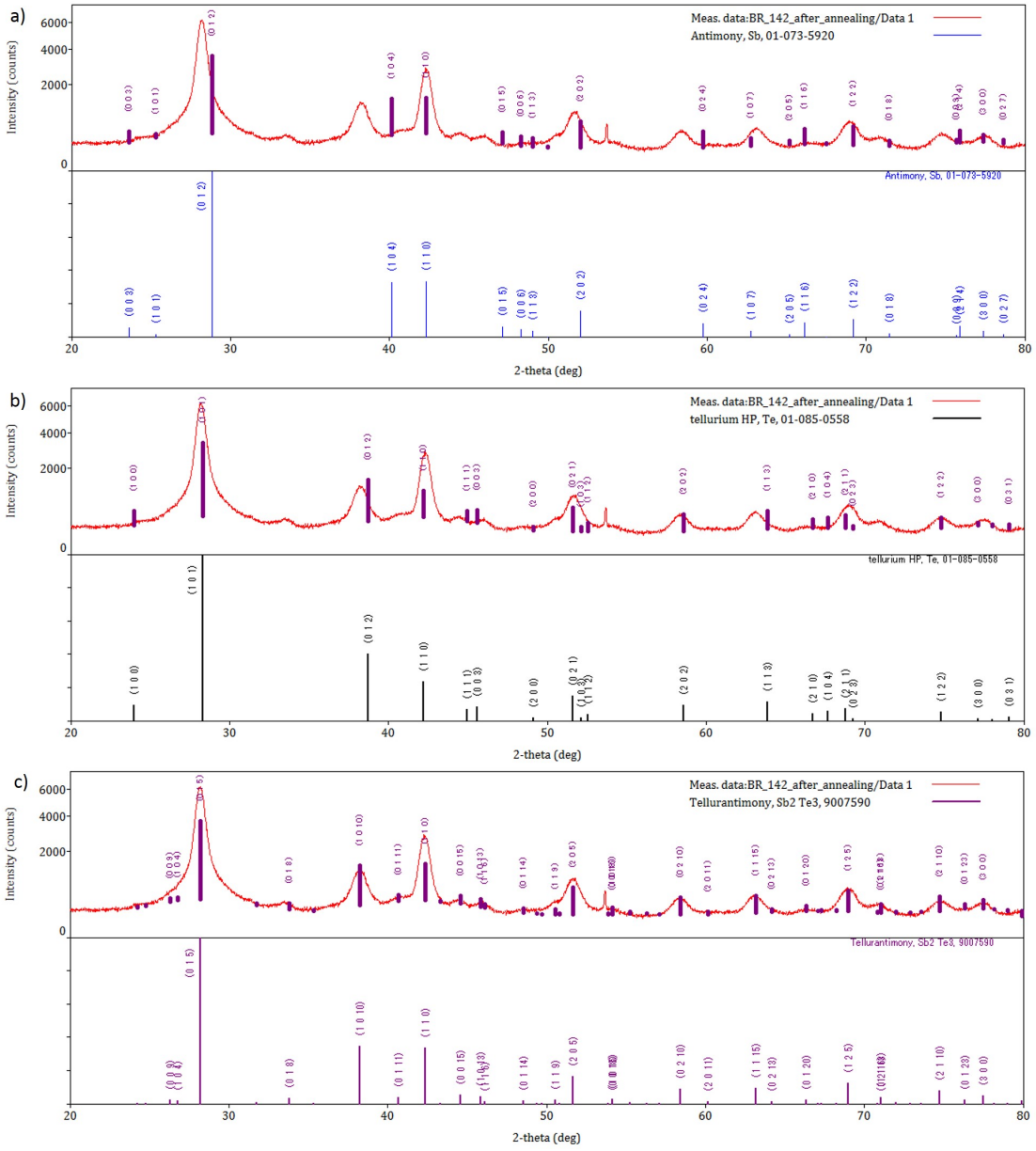

FIGURE 6.6: X-ray diffraction pattern of antimony telluride thin film electrodeposited from dichloromethane by pulsed deposition at -0.8 V vs. Ag/AgCl and post-annealed at 100 °C for 30 minutes fitted against a) Sb, b) Te, and c) Sb_2Te_3 literature pattern [42].

indicates crystallite size with the broadest indicating the smallest and the narrowest indicating the biggest crystallite size.

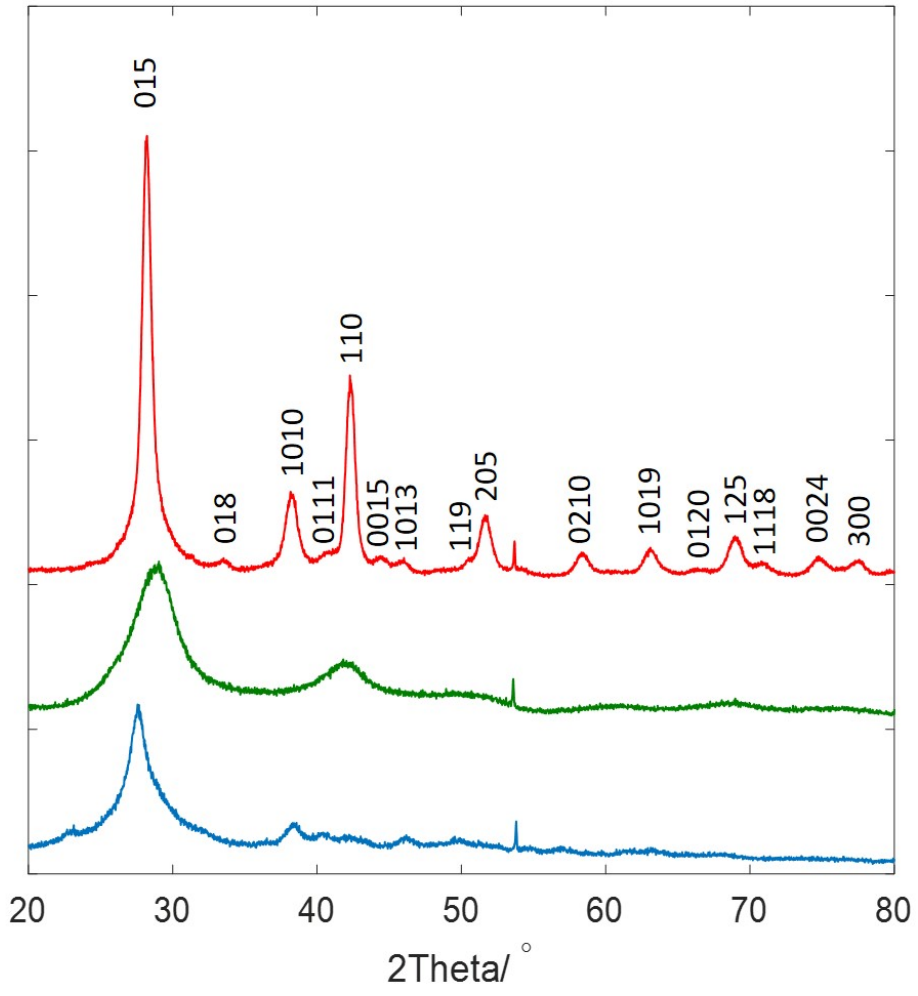

FIGURE 6.7: Grazing incidence X-ray diffraction pattern of Sb_2Te_3 electrodepsoted from 1.75 mM $[N^nBu_4][SbCl_4]$, 3 mM $[N^nBu_4]_2[TeCl_6]$ in CH_2Cl_2 solution containing 0.1 M $[N^nBu_4]Cl$ supporting electrolyte. Blue: potentiostatically, green: as-deposited by pulsed electrodeposition (t_{on}=5s, t_{off}=10 s) and red: post-annealed at 100 °C for 30 minutes deposited by pulsed electrodeposition. All films are electrodeposited at -0.80 V vs. Ag/AgCl.

6.3 Thermoelectric characterisation of the transferred film

Thermoelectric characterisation was conducted on the film electrodeposited by pulsed electrodeposition at -0.8 V vs. Ag/AgCl with on-time 5 s and off-time 10 s, after post-annealing at 100 °C for 30 minutes. The electrodeposited film is p-type with a charge carrier concentration of $(2.5\pm1.8)\times10^{20}$ cm^{-3}, resistivity of 7.9 mΩ cm and mobility of (3.8 ± 3.3) cm^2/V s at room temperature, as obtained from Hall measurements. Figure 6.8 shows resistivity and Seebeck coefficient (6.8a), and power factor (6.8b) as a function of temperature. The resistivity decreases with increasing temperature in the temperature range from 100 to 440 K, when it reaches a value of 0.9×10^{-4} Ω m at 440 K. By further increasing temperature from 440 to 530 K the resistivity increases reaching the value of 1.55×10^{-4} Ω m at 530 K. It might be that after annealing the film at 440 K gaps are introduced between the grains, further increasing with temperature increase. This effect of increasing resistivity by further increase of annealing temperature was observed in [34], although in this case resistivity decreased with increased annealing temperature from room temperature to 300 °C, then sharply increasing with further annealing temperature increase. The Seebeck coefficient increases by increasing the temperature in the temperature range from 100 to 485 K reaching the value of 107.5 μV/K, when it starts decreasing. The decrease in Seebeck coefficient after 485 K is due to the bipolar effect. The power factor is defined as $S^2\sigma$ meaning that it depends only on the Seebeck coefficient and the electrical conductivity of the material. Fig. 6.8b shows the power factor of the thin film as a function of temperature, showing that the power factor increases with increasing temperature reaching a value of 98.7 μW/ m K^2 at 464 K, when it starts decreasing. Thermoelectric properties of Sb_2Te_3 thin films have been much less investigated the thermoelectric properties of Bi_2Te_3 thin films, and the results reported in literature are not consistent. For example, Ma et al. [30] reported deposition of amorphous Sb_2Te_3 thin film from an aqueous solution by pulsed electrodeposition, which crystallises after annealing at 130°C for 2 h. The measured resistivity and Seebeck coefficient are 37.99 μ Ω m and 148.2 μV/K, respectively, with a power factor of 578.13 μW/ m K^2 at room temperature. The measured carrier concentration of the film is 9×10^{19}. Comparing, the thermoelectric properties of Sb_2Te_3 thin film electrodeposited from dichloromethane by pulsed electrodeposition after annealing at 100°C for 30 minutes are much lower. The resistivty and Seebeck coefficient measured at room temperature are 118.6 μ Ω m and 79.5 μV/K, respectively, with the power factor of 53.3 μW/ m K^2. The measured carrier concentration is $(2.5\pm1.8)\times10^{20}$, higher than the reported one.

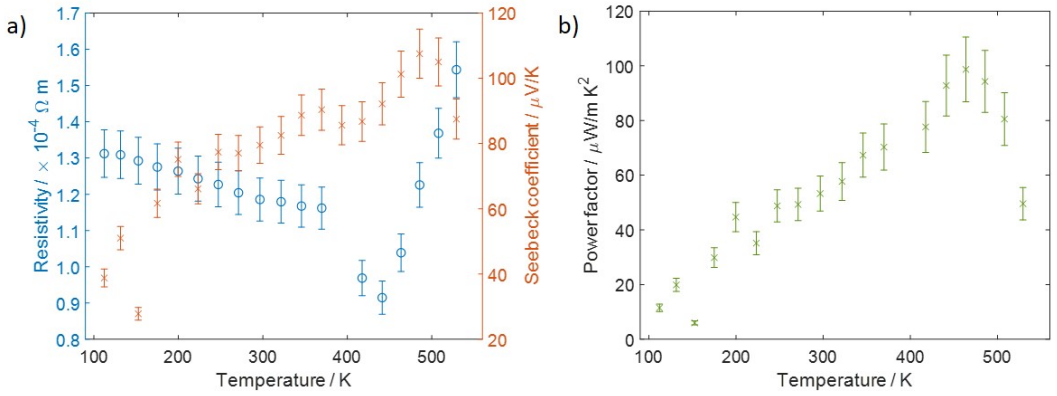

FIGURE 6.8: Dependence of a) resistivity and Seebeck coefficient, and b) power factor with temperature for antimony telluride film electrodeposited by pulsed electrodeposition at -0.8 V vs. Ag/AgCl with on-time 5 s and off-time 10 s.

6.4 Summary

Antimony telluride thin films were electrodeposited from electrolyte containing $[N^nBu_4][SbCl_4]$ and $[N^nBu_4]_2[TeCl_6]$ as Sb and Te precursors, respectively, and $[N^nBu_4]Cl$ as supporting electrolyte dissolved in dichloromethane (CH_2Cl_2). The films electrodeposited potentiostatically were rough and discontinuous, the more so with the higher applied overpotential. Pulsed electrodeposition at -0.8 V vs. Ag/AgCl (t_{on}=5 s, t_{off}=10 s) achieved continuous, compact and smooth film with stoichiometric Sb to Te ratio, as confirmed by EDX. XRD pattern of the film grown by pulsed electrodeposition showed poor crystallinity of as-deposited film. However, after post-annealing at 100°C for 30 minutes the film crystallises as observed in XRD pattern, proving as well the deposition of Sb_2Te_3 compound. Observation under SEM and EDX elemental analysis showed no change in morphology and Sb to Te ratio of the post-annealed film compared to the as-deposited. Thermo-electric measurements were carried out on Sb_2Te_3 film deposited by pulsed electrodeposition at -0.8 V vs. Ag/AgCl (t_{on}=5 s, t_{off}=10 s), post-annealed at 100°C for 30 minutes. In order to carry out electric measurements, the post-annealed film was transferred from the conductive TiN electrode onto insulating SiO_2 substrate using polystyrene as the carrier polymer. Hall measurements showed that the films is p-type with a charge carrier concentration of $(2.5\pm1.8)\times10^{20}$ cm^{-3} and resistivity of 7.9 mΩ cm at room temperature. Temperature dependent resistivity measurements showed that the resistivity decreases with temperature increase reaching a value of 0.9×10^{-4} Ω m at 440 K. By further temperature increase, the resistivity increased reaching a value of 1.55×10^{-4} Ω m at 530 K. The Seebeck coefficient increased with temperature increase reaching a value of 107.5 μV/K at 458 K, when it started decreasing. The corresponding power factor increased up to the value of 98.7 μW/ m K^2 at 464 K, when it started decreasing. Comparing to Bi_2Te_3, electrodeposition of Sb_2Te_3 was shown to be unrepeatable as continuous and smooth films could not be obtained afterwards (see Appendix 7.3), whereas Bi_2Te_3 films were replicated with established combination of pulsed electrodeposition preceded by a short nucleation pulse (see Appendix 7.2).

Chapter 7

Conclusions and Future Work

Bismuth telluride thin films films were fabricated by potentiostatic and pulsed electrodeposition with or without a preceding nucleation pulse from dichloromethane using $[N^nBu_4][BiCl_4]$ and $[N^nBu_4]_2[TeCl_6]$ as the Bi and Te precursors. The composition repeatability between replicate samples was significantly improved in films produced by pulsed electrodeposition compared to those obtained potentiostatically. In addition, somewhat smoother films were obtained by pulsed electrodeposition, however, both methods yield either porous or discontinuous films which are unsuitable for thermoelectric applications. Nucleation of the films was optimised by applying an initial nucleation pulse at high overpotential followed by growth of the films either potentiostatically or by pulsed electrodeposition at lower overpotential. The films grown potentiostatically preceded by a nucleation pulse are discontinuous while those grown by pulsed electrodeposition preceded by a nucleation pulse are continuous, compact and smooth. XPS measurements reveal that the porous films are prone to oxidation possibly due to their high surface to volume ratio, while the smooth and compact films are significantly less oxidised. Moreover, it was found that if the smooth and compact film were Te terminated the oxidation was suppressed. The effect of oxidation was also observed in EDX compositional analysis, where the oxygen content dropped considerably for smooth films obtained by pulsed electrodeposition preceded by a nucleation pulse as compared to the porous films. The XRD measurements show that films grown at the lower overpotential have larger crystallite sizes, and the films grown at low overpotential either with or without a preceding nucleation pulse exhibit similar crystallite sizes. In order to perform electrical measurements the films were transferred using polystyrene as a carrier polymer. The transfer process was complete and the films had no wrinkles or cracks after transfer. The porous films produced by potentiostatic and pulsed electrodeposition were found to be insulating most probably due to their high surface area prone to oxidation, which degrades thermoelectric properties of these films. The compact and smooth film produced by pulsed electrodeposition at -0.6 V preceded by a nucleation pulse at -1.0 V vs. Ag/AgCl exhibits semiconducting behaviour with the resistivity of

the film decreasing with increasing temperature. The film is n-type with a charge carrier concentration of (2.8±1.2) $\times 10^{20}$ cm^{-3} at room temperature as obtained from Hall measurements. The temperature dependent Seebeck coefficient measurements show a Seebeck coefficient of -51.7 μV/K at room temperature, reaching -96.6 μV/K at 520 K. The power factor reaches value of 88.2 μW/ m K^2 at 520 K.

Antimony telluride thin films were fabricated by potentiostatic and pulsed electrodeposition from dichloromethane using $[N^nBu_4][SbCl_4]$ and $[N^nBu_4]_2[TeCl_6]$ as the Sb and Te precursors for the first time. The films electrodeposited potentiostatically are porous and discontinuous, the more so with the higher applied overpotential. The smooth, continuous and compact film was obtained by pulsed electrodeposition at -0.8 V vs. Ag/AgCl, however the experiment is not repeatable. As-deposited film by pulsed electrodeposition exhibits poor crystallinity, but crystallises after annealing. For thermoelectric characterisation, the film was transferred from conductive TiN substrate to insulating SiO_2 using polystyrene as a carrier polymer. Hall measurements show that the film is p-type with a charge carrier concentration of (2.5±1.8)$\times 10^{20}$ cm^{-3} and resistivity of 7.9 mΩ cm at room temperature. Temperature dependent thermoelectric measurements show that the resistivity is decreasing with temperature increase from 100 to 440 K, reaching a lowest value of 0.9×10^{-4} Ω m at 440 K. By further temperature increase resistivity increases reaching the highest value of 1.55×10^{-4} Ω m at 530 K. The Seebeck coefficient increases with temperature increase from 100 to 485 K reaching the value of 107.5 μV/K, when it starts decreasing. The power factor of the thin film as a function of temperature increases with increasing temperature reaching the highest value of 98.7 μW/ m K^2 at 464 K, when it starts decreasing.

Apart from thin film electrodeposition, dichloromethane could enable electrodeposition of nanowires with diameter smaller than 10 nm. As mentioned above, theoretical works predict a great enhancement of thermoelectric properties in Bi_2Te_3 nanowires with diameter of 8 nm and smaller. However, in the most investigated aqueous electrolytes such small diameter cannot be obtained due to surface tension. Therefore, the future work would focus on growing and characterising Bi_2Te_3 and Sb_2Te_3 nanowires in mesoporous silica templates in order to experimentally show whether the great enhancement in thermoelectric properties is possible.

Appendix

Precursors synthesis and characterisation

$[N^nBu_4][SbCl_4]$: A Schlenk tube was loaded with $SbCl_3$ (0.461 g, 2.02×10^{-3} mol) and $[N^nBu_4]Cl$ (0.559 g, 2.01×10^{-3} mol). CH_2Cl_2 (20 mL) was added with stirring giving a clear, colourless solution. After stirring at room temperature for 30 minutes, the solution was concentrated *in vacuo* to *ca.* 10 mL, layered with hexane (20 mL) and stored at *ca.* -18 °C overnight. A large amount of colourless crystals appeared, and was collected by filtration, washed with hexane and dried *in vacuo*. Yield: 0.977 g (96%). Anal. Calcd. for $C_{16}H_{36}Cl_4NSb$: C, 38.0; H, 7.2; N, 2.8. Found: C, 38.0; H, 7.2; N, 2.8%. IR (Nujol/cm-*1*): 269, 345. Raman (cm^{-1}): 254, 288, 345.

$[N^nBu_4][BiCl_4]$: A Schlenk tube was loaded with $BiCl_3$ (0.319 g, 1.01×10^{-3} mol) and $[N^nBu_4]Cl$ (0.280 g, 1.01×10^{-3} mol). MeCN (20 mL) was added with stirring giving a clear, colourless solution. After stirring at room temperature for approximately 2 h, the solution was concentrated *in vacuo* to *ca.* 5 mL, layered with Et_2O and stored at *ca.* -18 °C for a few days. A colourless microcrystalline solid appeared, and was collected by filtration, washed with Et_2O and dried *in vacuo*. Yield: 0.403 g (68%). Anal. Calcd. for $C_{16}H_{36}Cl_4NBi$: C, 32.3; H, 6.1; N, 2.4. Found: C, 33.1; H, 6.1; N, 2.4%. IR (Nujol/cm-*1*): 256, 287. Raman (cm^{-1}): 254, 289.

$[N^nBu_4]_2[TeCl_6]$: A Schlenk tube was loaded with $TeCl_4$ (0.269 g, 9.98×10^{-4} mol) and $[N^nBu_4]Cl$ (0.559 g, 2.01×10^{-3} mol). CH_2Cl_2 (40 mL) was added with stirring giving a cloudy, yellow solution. After stirring at room temperature for approximately 1 h, the solution was filtered. The clear yellow filtrate was concentrated *in vacuo* to *ca.* 5 mL, layered with Et_2O (10 mL) and stored at *ca.* -18 °C overnight. A solid yellow mass formed, and was collected by filtration, washed with Et_2O and dried *in vacuo*. Yield: 0.694 g (84%). Anal. Calcd. for $C_{32}H_{72}Cl_6N_2Te$: C, 46.6; H, 8.8; N, 3.4. Found: C, 46.4; H, 8.7; N, 3.5%. IR (Nujol/cm-*1*): 223. Raman (cm^{-1}): 242, 283. ^{125}Te NMR (CH_2Cl_2/CD_2Cl_2, 298 K): δ=1324 [88].

Electrochemical quartz crystal microbalance (EQCM) study of $[N^nBu_4][SbCl_4]$ precursor

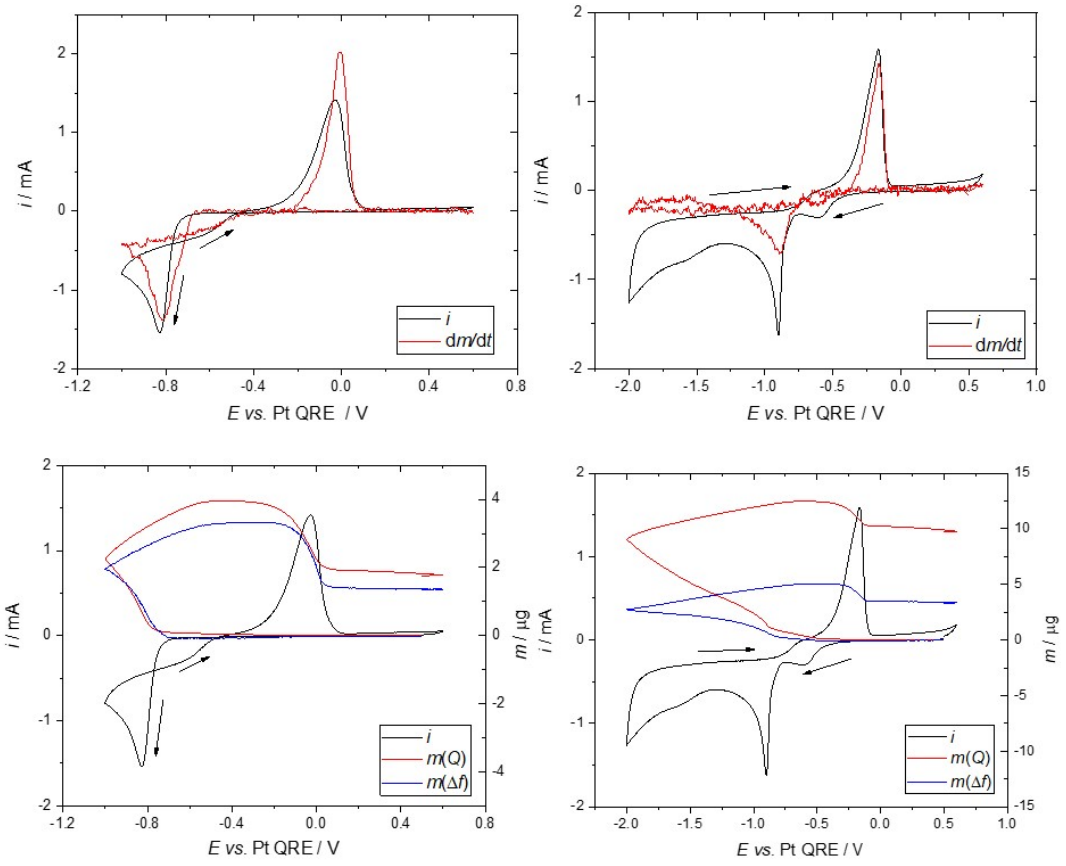

FIGURE 7.1: CVs of 2 mM $[N^nBu_4][SbCl_4]$ in 0.1 M $[N^nBu_4]Cl/CH_2Cl_2$ at 50 mV s^{-1} on a Pt EQCM. dm/dt is the derivative of the mass increase from the frequency response of the EQCM to give a plot of "expected current" from the change in mass, assuming all mass changes are a result of the $3e^-$ reduction/oxidation of $Sb^{3+}/Sb(0)$. m(Q) is the mass calculated as a function of the charge passed. m(f) is the mass calculated as a function of the frequency change of the crystal. (Left) Scan is reversed just after the plating peak. (Right) Scan is reversed just before electrolyte decomposition.

Reproducibility of electrodeposition of Bi_2Te_3 thin films from CH_2Cl_2

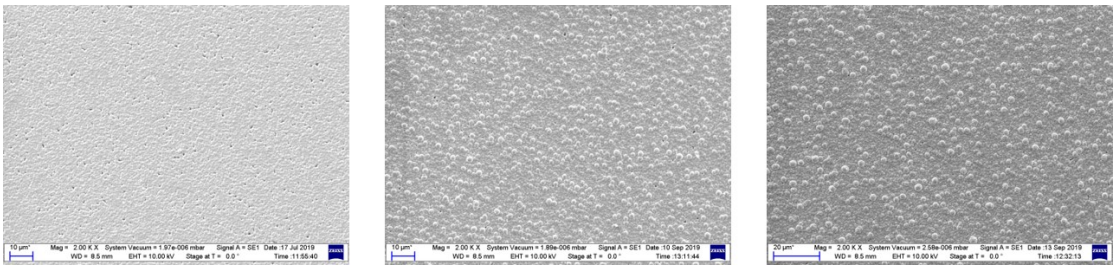

FIGURE 7.2: SEM images of three Bi_2Te_3 thin films electrodeposited by pulsed electrodeposition at -0.6 V vs. Ag/AgCl for on-time 5 s and off-time 10 s with an initial nucleation pulse of -1.0 V vs. Ag/AgCl for 5 s.

TABLE 7.1: Reproducibility results on three Bi_2Te_3 thin films electrodeposited by pulsed electrodeposition at -0.6 V vs. Ag/AgCl for on-time 5 s and off-time 10 s with an initial nucleation pulse of -1.0 V vs. Ag/AgCl for 5 s showing Bi:Te ratio, oxygen content and thermoelectric measurements taken at 300 K.

Bi:Te ± stdev	% atomic O ± stdev	Resistivity (mΩ cm)	Carrier concentration (cm^{-3})	Mobility (cm^2/ V s)	Seebeck coefficient (uV/ K)	Power factor (uW/ m K^2)
0.7 ± 0.01	6.5 ± 1.0	16.9	4.54E+20	0.81	-51.7	14.9
		16.8	3.50E+20	1.06		
		20.8	3.39E+20	0.89		
0.7 ± 0.01	5.8 ± 2.6	21.2	4.82E+19	6.13	-32.6	5.3
		19.6	1.31E+21	0.24		
		18.3	8.48E+20	0.40		
0.7 ± 0.04	3.3 ± 0.4	20.2	1.97E+21	0.16	-68.1	19.3
		23.8	2.32E+20	1.13		
		28.4	3.32E+20	0.68		

Reproducibility of electrodeposition of Sb_2Te_3 thin films from CH_2Cl_2

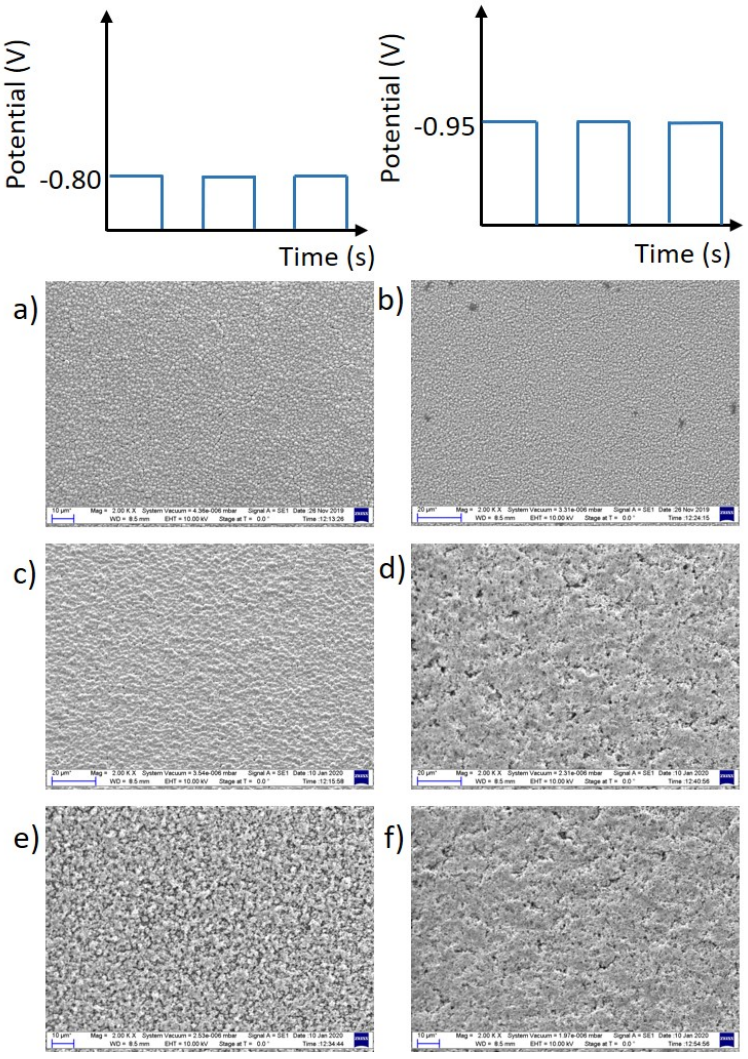

FIGURE 7.3: SEM images of three Sb_2Te_3 thin films electrodeposited by pulsed electrodeposition at -0.8 V (a, c, e), and -0.95 V (b, d, f) vs. Ag/AgCl for on-time 5 s and off-time 10 s with an initial nucleation pulse of -1.0 V vs. Ag/AgCl for 5 s.

Bibliography

[1] U.S. Energy Information Administration. *International energy outlook 2016*. 2016.

[2] Xiao Zhang and Li-Dong Zhao. Thermoelectric materials: Energy conversion between heat and electricity. *Journal of Materiomics*, 1(2):92–105, 2015.

[3] Terry M. Tritt. Thermoelectric Phenomena, Materials, and Applications. *Annual Review of Materials Research*, 41(1):433–448, 2011.

[4] G. Jeffrey Snyder and Eric S. Toberer. Complex thermoelectric materials. *Nature Materials*, 7(2):105–114, 2008.

[5] Ian T. Witting, Thomas C. Chasapis, Francesco Ricci, Matthew Peters, Nicholas A. Heinz, Geoffroy Hautier, and G. Jeffrey Snyder. The Thermoelectric Properties of Bismuth Telluride. *Advanced Electronic Materials*, 5(6):1–20, 2019.

[6] M. R. Burton, S. J. Richardson, P. A. Staniec, N. J. Terrill, J. M. Elliott, A. M. Squires, N. M. White, and Iris S. Nandhakumar. A novel route to nanostructured bismuth telluride films by electrodeposition. *Electrochemistry Communications*, 76:71–74, 2017.

[7] Xiaohong Li, Elena Koukharenko, Iris S Nandhakumar, John Tudor, Steve P Beeby, and Neil M White. High density p-type $Bi_{0.5}Sb_{1.5}Te_3$ nanowires by electrochemical templating through ion-track lithography. *Physical chemistry chemical physics : PCCP*, 11(18):3584–3590, 2009.

[8] In Joon Yoo, Nosang V. Myung, Dong Chan Lim, Youngsup Song, Young Keun Jeong, Yang Do Kim, Kyu Hwan Lee, and Jae Hong Lim. Electrodeposition of Bi_xTe_y thin films for thermoelectric application. *Thin Solid Films*, 546(3):48–52, 2013.

[9] Pallavi B. Patil, Sawanta S. Mali, Kishorkumar V. Khot, Vijay V. Kondalkar, Vishvanath B. Ghanwat, Rahul M. Mane, Rohini R. Kharade, and Popatrao N. Bhosale. Synthesis of Bismuth Telluride Thin Film for Thermoelectric Application Via Electrodeposition Technique. *Macromolecular Symposia*, 361(1):152–155, 2016.

[10] Pilwon Heo, Kenji Hagiwara, Ryoichi Ichino, and Masazumi Okido. Electrodeposition and Thermoelectric Characterization of Bi_2Te_3. *Journal of The Electrochemical Society*, 153(4):C213, 2006.

[11] J. B. Thorat, S. V. Mohite, S. B. Madake, R. D. Suryavanshi, K. Y. Rajpure, T. J. Shinde, V. J. Fulari, and N. S. Shinde. Electrochemical and surface deformation studies on electrodeposited nanostructured Bi_2Te_3 thin films. *Optics and Laser Technology*, 113:384–393, 2019.

[12] Wan Shan Kang, Wen Jin Li, Wei Chen Chou, Mao Feng Tseng, and Chao Sung Lin. Microstructure and thermoelectric properties of Bi_2Te_3 electrodeposits plated in nitric and hydrochloric acid baths. *Thin Solid Films*, 623:90–97, 2017.

[13] Qinglin Jiang, Congcong Liu, Haijun Song, Jingkun Xu, Daize Mo, Hui Shi, Zhipeng Wang, Fengxing Jiang, Baoyang Lu, and Zhengyou Zhu. Free-standing PEDOT: PSS film as electrode for the electrodeposition of bismuth telluride and its thermoelectric performance. *International Journal of Electrochemical Science*, 9(12):7540–7551, 2014.

[14] Ken Matsuoka, Mitsuaki Okuhata, Naoki Hatsuta, and Masayuki Takashiri. Effect of composition on the properties of bismuth telluride thin films produced by galvanostatic electrodeposition. *Transactions of the Materials Research Society of Japan*, 40(4):383–387, 2015.

[15] Yi Ma, Elisabet Ahlberg, Ye Sun, Bo Brummerstedt Iversen, and Anders E.C. Palmqvist. Thermoelectric properties of thin films of bismuth telluride electrochemically deposited on stainless steel substrates. *Electrochimica Acta*, 56(11):4216–4223, 2011.

[16] Cristina V. Manzano, Begoña Abad, Miguel Muñoz Rojo, Yee Rui Koh, Stephen L. Hodson, Antonio M. Lopez Martinez, Xianfan Xu, Ali Shakouri, Timothy D. Sands, Theodorian Borca-Tasciuc, and Marisol Martin-Gonzalez. Anisotropic Effects on the Thermoelectric Properties of Highly Oriented Electrodeposited Bi_2Te_3 Films. *Scientific Reports*, 6(1):19129, 2016.

[17] Aijun Zhou, Qiang Fu, Wenhua Zhang, Bin Yang, Jingze Li, Pawel Ziolkowski, Eckhard Mueller, and Dongyan Xu. Enhancing the Thermoelectric Properties of the Electroplated Bi_2Te_3 Films by Tuning the Pulse Off-to-on Ratio. *Electrochimica Acta*, 178:217–224, 2015.

[18] Cristina V. Manzano, Adriana A. Rojas, Michelle Decepida, Begoña Abad, Yazmin Feliz, Olga Caballero-Calero, Diana-Andra Borca-Tasciuc, and Marisol Martin-Gonzalez. Thermoelectric properties of Bi_2Te_3 films by constant and pulsed electrodeposition. *Journal of Solid State Electrochemistry*, 17(7):2071–2078, 2013.

[19] Marisol S. Martın-Gonzalez, Amy L. Prieto, Ronald Gronsky, Timothy Sands, and Angelica M. Stacy. Insights into the Electrodeposition of Bi_2Te_3. *Journal of The Electrochemical Society*, 149(11):C546, 2002.

[20] M Abellan, R Schrebler, and H Gómez. Electrodeposition of Bi_2Te_3 thin films onto FTO substrates from DMSO solution. *International Journal of Electrochemical Science*, 10:7409–7422, 2015.

[21] Hai P. Nguyen, Minxian Wu, Jiale Su, Ruud J.M. Vullers, Philippe M. Vereecken, and Jan Fransaer. Electrodeposition of bismuth telluride thermoelectric films from a nonaqueous electrolyte using ethylene glycol. *Electrochimica Acta*, 68:9–17, 2012.

[22] Minxian Wu, Hai P. Nguyen, Ruud J. M. Vullers, Philippe M. Vereecken, Koen Binnemans, and Jan Fransaer. Electrodeposition of Bismuth Telluride Thermoelectric Films from Chloride-Free Ethylene Glycol Solutions. *Journal of The Electrochemical Society*, 160(4):D196–D201, 2013.

[23] Jonathan Szymczak, Sophie Legeai, Stéphanie Michel, Sébastien Diliberto, Nicolas Stein, and Clotilde Boulanger. Electrodeposition of stoichiometric bismuth telluride Bi_2Te_3 using a piperidinium ionic liquid binary mixture. *Electrochimica Acta*, 137:586–594, 2014.

[24] Paothep Pichanusakorn and Prabhakar Bandaru. Nanostructured thermoelectrics. *Materials Science and Engineering R: Reports*, 67(2-4):19–63, 2010.

[25] Jaime Martín, Cristina V. Manzano, Olga Caballero-Calero, and Marisol Martín-González. High-aspect-ratio and highly ordered 15-nm porous alumina templates. *ACS Applied Materials and Interfaces*, 5(1):72–79, 2013.

[26] Doriane Del Frari, Sébastien Diliberto, Nicolas Stein, Clotilde Boulanger, and Jean Marie Lecuire. Comparative study of the electrochemical preparation of Bi_2Te_3, Sb_2Te_3, and $(Bi_xSb_{1-x})_2Te_3$ films. *Thin Solid Films*, 483(1-2):44–49, 2005.

[27] Q. Huang, A. J. Kellock, and S. Raoux. Electrodeposition of SbTe phase-change alloys. *Journal of the Electrochemical Society*, 155(2):104–109, 2008.

[28] Su Kyum Lim, Min Young Kim, and Tae Sung Oh. Thermoelectric properties of the bismuth-antimony-telluride and the antimony-telluride films processed by electrodeposition for micro-device applications. *Thin Solid Films*, 517(14):4199–4203, 2009.

[29] Jae Hong Lim, Mi Yeong Park, Dong Chan Lim, Bongyoung Yoo, Jung Ho Lee, Nosang V. Myung, and Kyu Hwan Lee. Electrodeposition of p-type Sb_xTe_y thermoelectric films. *Journal of Electronic Materials*, 40(5):1321–1325, 2011.

[30] Yi Ma, Elisabet Ahlberg, Ye Sun, Bo Brummerstedt Iversen, and Anders E.C. Palmqvist. Thermoelectric characteristics of electrochemically deposited Bi_2Te_3

and Sb_2Te_3 thin films of relevance to multilayer preparation. *Journal of the Electrochemical Society*, 159(2):50–58, 2012.

[31] Jiwon Kim, Miluo Zhang, Wayne Bosze, Su Dong Park, Jae Hong Lim, and Nosang V. Myung. Maximizing thermoelectric properties by nanoinclusion of γ-SbTe in Sb_2Te_3 film via solid-state phase transition from amorphous Sb-Te electrodeposits. *Nano Energy*, 13:727–734, 2015.

[32] Ning Su, Shuai Guo, Fu Li, Dawei Liu, and Bo Li. Electrodeposition of p-Type Sb_2Te_3 Films and Micro-Pillar Arrays in a Multi-Channel Glass Template. *Materials*, 11(7):1194, 2018.

[33] William D. Sides and Qiang Huang. Electrochemical nucleation and growth of antimony telluride binary compound on gold substrate. *Journal of the Electrochemical Society*, 165(11):D568–D573, 2018.

[34] Naoki Hatsuta, Daichi Takemori, and Masayuki Takashiri. Effect of thermal annealing on the structural and thermoelectric properties of electrodeposited antimony telluride thin films. *Journal of Alloys and Compounds*, 685(3):147–152, 2016.

[35] Hai P. Nguyen, Xiaoxu Peng, Ganapathi Murugan, Ruud J.M. Vullers, Philippe M. Vereecken, and Jan Fransaer. Electrodeposition of antimony, tellurium and their alloys from molten acetamide mixtures. *Journal of the Electrochemical Society*, 160(2):75–79, 2013.

[36] Adriana Simona Catrangiu, Ion Sin, Paula Prioteasa, Adina Cotarta, Anca Cojocaru, Liana Anicai, and Teodor Visan. Studies of antimony telluride and copper telluride films electrodeposition from choline chloride containing ionic liquids. *Thin Solid Films*, 611:88–100, 2016.

[37] A. J. Minnich, M. S. Dresselhaus, Z. F. Ren, and G. Chen. Bulk nanostructured thermoelectric materials: current research and future prospects. *Energy & Environmental Science*, 2(5):466, 2009.

[38] Jeannine R. Szczech, Jeremy M. Higgins, and Song Jin. Enhancement of the thermoelectric properties in nanoscale and nanostructured materials. *Journal of Matererials Chemistry*, 21(12):4037–4055, 2011.

[39] Zhi Gang Chen, Guang Hana, Lei Yanga, Lina Cheng, and Jin Zou. Nanostructured thermoelectric materials: Current research and future challenge. *Progress in Natural Science: Materials International*, 22(6):535–549, 2012.

[40] Marisol Martín-González, O. Caballero-Calero, and P. Díaz-Chao. Nanoengineering thermoelectrics for 21^{st} century: Energy harvesting and other trends in the field. *Renewable and Sustainable Energy Reviews*, 24:288–305, 2013.

[41] Lon E. Bell. Cooling, heating, generating power, and recovering waste heat with thermoelectric systems. *Science*, 321(5895):1457–1461, 2008.

[42] Inorganic Crystal Structure Database (ICSD, Fiz Karlsruhe, Germany) accessed via the National Chemical Database Service hosted by the Royal Society of Chemistry.

[43] Lingcong Meng, Katarina Cicvarić, Andrew L. Hector, C.H. de Groot, and Philip N. Bartlett. Electrodeposition of bismuth telluride from a weakly coordinating, non-aqueous solution. *Journal of Electroanalytical Chemistry*, 839:134–140, 2019.

[44] Hilaal Alam and Seeram Ramakrishna. A review on the enhancement of figure of merit from bulk to nano-thermoelectric materials. *Nano Energy*, 2(2):190–212, 2013.

[45] Yucheng Lan, Austin Jerome Minnich, Gang Chen, and Zhifeng Ren. Enhancement of thermoelectric figure-of-merit by a bulk nanostructuring approach. *Advanced Functional Materials*, 20(3):357–376, 2010.

[46] H. Julian Goldsmid. Bismuth telluride and its alloys as materials for thermoelectric generation. *Materials*, 7(4):2577–2592, 2014.

[47] Wolfgang G. Zeier, Alex Zevalkink, Zachary M. Gibbs, Geoffroy Hautier, Mercouri G. Kanatzidis, and G. Jeffrey Snyder. Thinking Like a Chemist: Intuition in Thermoelectric Materials. *Angewandte Chemie - International Edition*, 55(24):6826–6841, 2016.

[48] Weishu Liu, Xiao Yan, Gang Chen, and Zhifeng Ren. Recent advances in thermoelectric nanocomposites. *Nano Energy*, 1(1):42–56, 2012.

[49] Yoichi Ando, N. Miyamoto, Kouji Segawa, T. Kawata, and I. Terasaki. Specific-heat evidence for strong electron correlations in the thermoelectric material (Na,Ca)Co_2O_4. *Physical Review B*, 60(15):5, 1999.

[50] G. Jeffrey Snyder, Mogens Christensen, Eiji Nishibori, Thierry Caillat, and Bo Brummerstedt Iversen. Disordered zinc in Zn_4Sb_3 with phonon-glass and electron-crystal thermoelectric properties. *Nature Materials*, 3(7):458–463, 2004.

[51] Sabah K. Bux, Jean-Pierre Fleurial, and Richard B. Kaner. Nanostructured materials for thermoelectric applications. *Chemical Communications*, 46(44):8311, 2010.

[52] Zhao Wenyu, Wei Ping, Zhang Qingjie, Dong Chunlei, Liu Lisheng, and Tang Xinfeng. Enhanced thermoelectric performance in barium and indium double-filled skutterudite bulk materials via orbital hybridization induced by indium filler. *Journal of the American Chemical Society*, 131(10):3713–3720, 2009.

[53] A. Saramat, G. Svensson, A. E.C. Palmqvist, C. Stiewe, E. Mueller, D. Platzek, S. G.K. Williams, D. M. Rowe, J. D. Bryan, and G. D. Stucky. Large thermoelectric figure of merit at high temperature in Czochralski-grown clathrate $Ba_8Ga_{16}Ge_{30}$. *Journal of Applied Physics*, 99(2):2–6, 2006.

[54] Shawna R. Brown, Susan M. Kauzlarich, Franck Gascoin, and G. Jeffrey Snyder. $Yb_{14}MnSb_{11}$: New high efficiency thermoelectric material for power generation. *Chemistry of Materials*, 18(7):1873–1877, 2006.

[55] Valeriy Yu. Verchenko, Zheng Wei, Alexander A. Tsirlin, Carolien Callaert, Anton Jesche, Joke Hadermann, Evgeny V. Dikarev, and Andrei V. Shevelkov. Crystal Growth of the Nowotny Chimney Ladder Phase Fe_2Ge_3 : Exploring New Fe-Based Narrow-Gap Semiconductor with Promising Thermoelectric Performance. *Chemistry of Materials*, 29:9954–99630, 2017.

[56] Joseph P. Heremans, Vladimir Jovovic, Eric S. Toberer, Ali Saramat, Ken Kurosaki, Anek Charoenphakdee, Shinsuke Yamanaka, and G Jeffrey Snyder. Enhancement of Thermoelectric of the Electronic Density of States. *Science*, 321:1457–1461, 2008.

[57] Lyndon D. Hicks and Mildred S. Dresselhaus. Thermoelectric figure of merit of a one-dimensional conductor. *Physical Review B*, 47:16631–16634, 1993.

[58] Lyndon D. Hicks and Mildred S. Dresselhaus. Effect of quantum-well structures on the thermoelectric figure of merit. *Physical Review B*, 47:12727–12731, 1993.

[59] Mildred S. Dresselhaus, Gang Chen, Ming Y. Tang, Ronggui Yang, Hohyun Lee, Dezhi Wang, Zhifeng Ren, Jean Pierre Fleurial, and Pawan Gogna. New directions for low-dimensional thermoelectric materials. *Advanced Materials*, 19(8):1043–1053, 2007.

[60] Zhen Li, Qiao Sun, Xiang Dong Yao, Zhong Hua Zhu, and Gao Qing (Max) Lu. Semiconductor nanowires for thermoelectrics. *Journal of Materials Chemistry*, 22(43):22821, 2012.

[61] Yangyang Qi, Zhen Wang, Mingliang Zhang, Fuhua Yang, and Xiaodong Wang. Thermoelectric devices based on one-dimensional nanostructures. *Journal of Materials Chemistry A*, 1(20):6110, 2013.

[62] Fitriani, R. Ovik, B. D. Long, M. C. Barma, M. Riaz, M. F.M. Sabri, S. M. Said, and R. Saidur. A review on nanostructures of high-temperature thermoelectric materials for waste heat recovery. *Renewable and Sustainable Energy Reviews*, 64:635–659, 2016.

[63] Azhar Ali, Yixi Chen, Venkata Vasiraju, and Sreeram Vaddiraju. Nanowire-based thermoelectrics. *Nanotechnology*, 28:282001, 2017.

[64] Rama Venkatasubramanian, Edward Siivola, Thomas Colpitts, K The, G Kanatzidis, These Zt, and B Vining. Thin-film thermoelectric devices with high room-temperature figures of merit. *Nature*, 413:597–602, 2001.

[65] T. C. Harman, P. J. Taylor, M. P. Walsh, and B. E. LaForge. Quantum dot superlattice thermoelectric materials and devices. *Science*, 297(5590):2229–2232, 2002.

[66] Christopher J. Vineis, Ali Shakouri, Arun Majumdar, and Mercouri G. Kanatzidis. Nanostructured thermoelectrics: Big efficiency gains from small features. *Advanced Materials*, 22(36):3970–3980, 2010.

[67] S.-M. Lee, David G Cahill, and Rama Venkatasubramanian. Thermal conductivity of Si – Ge superlattices. *Applied Physics Letters*, 70:2957–2959, 1997.

[68] M. N. Touzelbaev, P. Zhou, R. Venkatasubramanian, and K. E. Goodson. Thermal characterization of Bi_2Te_3/Sb_2Te_3 superlattices. *Journal of Applied Physics*, 90(2):763–767, 2001.

[69] Sebastian G. Volz and Gang Chen. Molecular dynamics simulation of thermal conductivity of silicon nanowires. *Applied Physics Letters*, 75(14):2056, 1999.

[70] Allon I. Hochbaum, Renkun Chen, Raul Diaz Delgado, Wenjie Liang, Erik C. Garnett, Mark Najarian, Arun Majumdar, and Peidong Yang. Enhanced thermoelectric performance of rough silicon nanowires. *Nature*, 451(7175):163–167, 2008.

[71] Mordechay Schlesinger and Milan Paunovic. *Modern Electroplating*. 2000.

[72] Noémie Elgrishi, Kelley J. Rountree, Brian D. McCarthy, Eric S. Rountree, Thomas T. Eisenhart, and Jillian L. Dempsey. A Practical Beginner's Guide to Cyclic Voltammetry. *Journal of Chemical Education*, 95(2):197–206, 2018.

[73] Milan Paunovic and Mordechay Schlesinger. *Fundamentals of Electrochemical Deposition*. 2006.

[74] B. Y. Yoo, C. K. Huang, J. R. Lim, J. Herman, M. A. Ryan, J. P. Fleurial, and N. V. Myung. Electrochemically deposited thermoelectric n-type Bi_2Te_3 thin films. *Electrochimica Acta*, 50(22):4371–4377, 2005.

[75] Masayuki Takashiri, Takumi Makioka, and Hiroki Yamamuro. Promotion of crystal growth in as-grown Bi_2Te_3 electrodeposited films without micro-pores using sputtered Bi_2Te_3 seed layers deposited on a glass substrate. *Journal of Alloys and Compounds*, 764:802–808, 2018.

[76] Biswapriya Deb, Yukihiro Isoda, Olga Caballero-Calero, Pablo Diaz-Chao, Marisol S. Martin-Gonzalez, and Yoshikazu Shinohara. Heat Treatment Effects

on Electrochemically Grown Bi_2Te_3 Thin Films for Thermoelectric Applications. *Materials Transactions*, 53(8):1481–1485, 2012.

[77] Andrew J. Naylor, Elena Koukharenko, Iris S. Nandhakumar, and Neil M. White. Surfactant-mediated electrodeposition of bismuth telluride films and its effect on microstructural properties. *Langmuir*, 28(22):8296–8299, 2012.

[78] O. Caballero-Calero, P. Díaz-Chao, B. Abad, C. V. Manzano, M. D. Ynsa, J. J. Romero, M. Muñoz Rojo, and M. S. Martín-González. Improvement of Bismuth Telluride electrodeposited films by the addition of Sodium Lignosulfonate. *Electrochimica Acta*, 123:117–126, 2014.

[79] Youngsup Song, In Joon Yoo, Na Ri Heo, Dong Chan Lim, Dongyun Lee, Joo Yul Lee, Kyu Hwan Lee, Kwang Ho Kim, and Jae Hong Lim. Electrodeposition of thermoelectric Bi_2Te_3 thin films with added surfactant. *Current Applied Physics*, 15(3):261–264, 2015.

[80] Chiranjit Kulsi, Mousumi Mitra, Kajari Kargupta, Saibal Ganguly, Dipali Banerjee, and Shyamaprosad Goswami. Effect of different surfactants and thicknesses on electrodeposited films of bismuth telluride and its thermoelectric performance. *Materials Research Express*, 2(10):0–11, 2015.

[81] Yanling Liu, Xiaoxia Yan, Zhigang Zeng, and Zhiyu Hu. Electrochemically Deposited Thermoelectric Bismuth-Telluride Films. *Advanced Materials Research*, 557-559:1811–1814, 2012.

[82] Minxian Wu, Salvador Alvarado Ramírez, Ehsan Shafahian, Lingyi Guo, Christ Glorieux, Koen Binnemans, and Jan Fransaer. Electrodeposition of bismuth telluride thin films containing silica nanoparticles for thermoelectric applications. *Electrochimica Acta*, 253:554–562, 2017.

[83] Gisbert Leimkühler, Ingo Kerkamm, and Rolf Reineke-Koch. Electrodeposition of antimony telluride. *Journal of the Electrochemical Society*, 149(10):474–478, 2002.

[84] Kerstin Tittes and Waldfried Plieth. Electrochemical deposition of ternary and binary systems from an alkaline electrolyte-a demanding way for manufacturing p-doped bismuth and antimony tellurides for the use in thermoelectric elements. *Journal of Solid State Electrochemistry*, 11(2):155–164, 2007.

[85] Hyunsung Jung and Nosang V. Myung. Electrodeposition of antimony telluride thin films from acidic nitrate-tartrate baths. *Electrochimica Acta*, 56(16):5611–5615, 2011.

[86] J. L. Lensch-Falk, D. Banga, P. E. Hopkins, D. B. Robinson, V. Stavila, P. A. Sharma, and D. L. Medlin. Electrodeposition and characterization of nanocrystalline antimony telluride thin films. *Thin Solid Films*, 520(19):6109–6117, 2012.

[87] Xingzhao Yan. Buhler Helios Pro XL Sputterer, Work Instruction, Southampton Nanofabrication Centre, School of Electronics and Computer Science, 2019.

[88] Philip N. Bartlett, David Cook, C. H. De Groot, Andrew L. Hector, Ruomeng Huang, Andrew Jolleys, Gabriela P. Kissling, William Levason, Stuart J. Pearce, and Gillian Reid. Non-aqueous electrodeposition of p-block metals and metalloids from halometallate salts. *RSC Advances*, 3(36):15645–15654, 2013.

[89] Philip N. Bartlett, Sophie L. Benjamin, C. H. Kees De Groot, Andrew L. Hector, Ruomeng Huang, Andrew Jolleys, Gabriela P. Kissling, William Levason, Stuart J. Pearce, Gillian Reid, and Yudong Wang. Non-aqueous electrodeposition of functional semiconducting metal chalcogenides: $Ge_2Sb_2Te_5$ phase change memory. *Materials Horizons*, 2(4):420–426, 2015.

[90] JEOL. Scanning Electron Microscope: Basic knowledge for using the SEM. *Jeol*, pages 1–32, 2006.

[91] S.T.Misture & R.L.Snyder. X-ray Polycrystalline Diffraction. *Encyclopedia of Materials: Science and Technology*, (2), 2001.

[92] Hidetaka Konno. *Chapter 8 - X-ray Photoelectron Spectroscopy.* Tsinghua University Press Limited, 2016.

[93] Keithley. van der Pauw and Hall Voltage Measurements with the 4200A-SCS Parameter Analyzer. *Keithley App Note*, 2016.

[94] Colin M. Hurd. *The Hall Effect in Metals and Alloys.* Plenum Press, New York, 1st edition, 1972.

[95] R. Mansfield. The Hall effect in semiconductors. *Proceedings of the Physical Society. Section B*, 69(8):862–865, 1956.

[96] https://www.linseis.com/en/products/thermoelectrics/lsr-3/.

[97] Namrata Bansal, Myung Rae Cho, Matthew Brahlek, Nikesh Koirala, Yoichi Horibe, Jing Chen, Weida Wu, Yun Daniel Park, and Seongshik Oh. Transferring MBE-Grown Topological Insulator Films to Arbitrary Substrates and Metal Insulator Transition via Dirac Gap. *Nano Letters*, 14:1343–1348, 2014.

[98] Huynh Van Ngoc, Yongteng Qian, Suk Kil Han, and Dae Joon Kang. PMMA-etching-free transfer of wafer-scale chemical vapor deposition two-dimensional atomic crystal by a water soluble polyvinyl alcohol polymer method. *Scientific Reports*, 6:1–9, 2016.

[99] Yang Yu, Patrick W.K. Fong, Shifeng Wang, and Charles Surya. Fabrication of WS_2/GaN p-n Junction by Wafer-Scale WS_2 Thin Film Transfer. *Scientific Reports*, 6:1–11, 2016.

[100] Bum Jun Kim, Nilesh K. Shrivastava, Tuqeer Nasir, Kyoung Soon Choi, Jouhahn Lee, Hak Chul Kim, Kwan Woo Kim, Mudusu Devika, Sang Hoon Lee, Byung Joo Jeong, Hak Ki Yu, and Jae Young Choi. Poly-Trimethoxyphenylsilane as Carrier Film for Residual-Free CVD Graphene Transfer. *Physica Status Solidi - Rapid Research Letters*, 11(11):1–4, 2017.

[101] Joshua D. Wood, Gregory P. Doidge, Enrique A. Carrion, Justin C. Koepke, Joshua A. Kaitz, Isha Datye, Ashkan Behnam, Jayan Hewaparakrama, Basil Aruin, Yaofeng Chen, Hefei Dong, Richard T. Haasch, Joseph W. Lyding, and Eric Pop. Annealing free, clean graphene transfer using alternative polymer scaffolds. *Nanotechnology*, 26(5):55302, 2015.

[102] Eric Auchter, Justin Marquez, Stephen L. Yarbro, and Enkeleda Dervishi. A facile alternative technique for large-area graphene transfer via sacrificial polymer. *AIP Advances*, 7(12):125306, 2017.

[103] Sukang Bae, Hyeongkeun Kim, Youngbin Lee, Xiangfan Xu, Jae Sung Park, Yi Zheng, Jayakumar Balakrishnan, Tian Lei, Hye Ri Kim, Young Il Song, Young Jin Kim, Kwang S. Kim, Barbaros Özyilmaz, Jong Hyun Ahn, Byung Hee Hong, and Sumio Iijima. Roll-to-roll production of 30-inch graphene films for transparent electrodes. *Nature Nanotechnology*, 5(8):574–578, 2010.

[104] Hiroki Yamamuro, Naoki Hatsuta, Makoto Wachi, Yoshihiro Takei, and Masayuki Takashiri. Combination of Electrodeposition and Transfer Processes for Flexible Thin-Film Thermoelectric Generators. *Coatings*, 8(1):22, 2018.

[105] M A Thomas and J B Cui. Highly Uniform 2D Growth, Substrate Transfer, and Electrical Characterization of Electrodeposited ZnO Thin Films. *Journal of The Electrochemical Society*, 160(6):218–225, 2013.

[106] C. Lei, K. S. Ryder, E. Koukharenko, M. Burton, and Iris S. Nandhakumar. Electrochemical deposition of bismuth telluride thick layers onto nickel. *Electrochemistry Communications*, 66:1–4, 2016.

[107] Matthew R. Burton, Andrew J. Naylor, and Iris S. Nandhakumar. Electrochemically copper-doped bismuth tellurium selenide thin films. *Electrochemistry Communications*, 97:56–59, 2018.

[108] Qingshuo Wei, Keisuke Tajima, and Kazuhito Hashimoto. Bilayer ambipolar organic thin-film transistors and inverters prepared by the contact-film-transfer method. *ACS Applied Materials and Interfaces*, 1(9):1865–1868, 2009.

[109] W.S. Rasband. ImageJ, U. S. National Institutes of Health, Bethesda, Maryland, USA, https://imagej.nih.gov/ij/, 1997-2018.

[110] Ki Beom Cheon, Sun Kyung Hwang, Se Won Seo, Jae Hyun Park, Min Ah Park, and Jin Young Kim. Roughness-Controlled $Cu_2ZnSn(S,Se)_4$ Thin-Film Solar Cells with Reduced Charge Recombination. *ACS Applied Materials and Interfaces*, 11:24088–24095, 2019.

[111] Yixin Zhao and Clemens Burda. Chemical synthesis of $Bi_{0.5}Sb_{1.5}Te_3$ nanocrystals and their surface oxidation properties. *ACS Applied Materials and Interfaces*, 1(6):1259–1263, 2009.

[112] S. M. Patil, S. R. Mane, R. M. Mane, S. S. Mali, P. S. Patil, and P. N. Bhosale. Synthesis and X-ray photoelectron spectroscopy (XPS) and thermoelectric studies of ternary $Bi_2(Te_{0.5}Se_{0.5})_3$ mixed-metal chalcogenide thin films by the arrested precipitation technique. *Canadian Journal of Chemistry*, 89(11):1375–1381, 2011.

[113] D. Ingersoll, A. L. Lima-Sharma, D. P. Adams, P. A. Sharma, P. Lu, J. F. Ihlefeld, J. R. Michael, S. Chou, J. D. Sugar, and M. Brumbach. Electrical contact uniformity and surface oxidation of ternary chalcogenide alloys. *AIP Advances*, 9(1):015125, 2019.

[114] Denis Music, Keke Chang, Paul Schmidt, Felix N. Braun, Martin Heller, Steffen Hermsen, Peter J. Pöllmann, Till Schulzendorff, and Cedric Wagner. On atomic mechanisms governing the oxidation of Bi_2Te_3. *Journal of Physics Condensed Matter*, 29(48):485705, 2017.

[115] Son D.N. Luu and Paz Vaqueiro. Synthesis, characterisation and thermoelectric properties of the oxytelluride Bi_2O_2Te. *Journal of Solid State Chemistry*, 226:219–223, 2015.

[116] Lada V. Yashina, Jaime Sánchez-Barriga, Markus R. Scholz, Andrey A. Volykhov, Anna P. Sirotina, Vera S. Neudachina, Marina E. Tamm, Andrei Varykhalov, Dmitry Marchenko, Gunther Springholz, Günther Bauer, Axel Knop-Gericke, and Oliver Rader. Negligible surface reactivity of topological insulators Bi_2Se_3 and Bi_2Te_3 towards oxygen and water. *ACS Nano*, 7(6):5181–5191, 2013.

[117] Andrey A. Volykhov, Jaime Sánchez-Barriga, Anna P. Sirotina, Vera S. Neudachina, Alexander S. Frolov, Evgeny A. Gerber, Elmar Yu Kataev, Boris Senkovsky, Nickolay O. Khmelevsky, Anatoliy Yu Aksenenko, Natalia V. Korobova, Axel Knop-Gericke, Oliver Rader, and Lada V. Yashina. Rapid Surface Oxidation of Sb_2Te_3 as Indication for a Universal Trend in the Chemical Reactivity of Tetradymite Topological Insulators. *Chemistry of Materials*, 28(24):8916–8923, 2016.